

THREE YEAR WILKINSON MICROWAVE ANISOTROPY PROBE (WMAP) OBSERVATIONS: POLARIZATION ANALYSIS

L. PAGE¹, G. HINSHAW², E. KOMATSU¹², M. R. NOLTA⁹, D. N. SPERGEL⁵, C. L. BENNETT¹⁰, C. BARNES¹, R. BEAN^{5,8}, O. DORÉ^{5,9},
M. HALPERN³, R. S. HILL², N. JAROSIK¹, A. KOGUT², M. LIMON², S. S. MEYER⁴, N. ODEGARD², H. V. PEIRIS^{4,14}, G. S.
TUCKER⁶, L. VERDE¹³, J. L. WEILAND², E. WOLLACK², E. L. WRIGHT⁷

Draft version January 25, 2020

ABSTRACT

The Wilkinson Microwave Anisotropy Probe (WMAP) has mapped the entire sky in five frequency bands between 23 and 94 GHz with polarization sensitive radiometers. We present three-year full-sky maps of the polarization and analyze them for foreground emission and cosmological implications. These observations open up a new window for understanding how the universe began and help set a foundation for future observations.

WMAP observes significant levels of polarized foreground emission due to both Galactic synchrotron radiation and thermal dust emission. Synchrotron radiation is the dominant signal at $\ell < 50$ and $\nu \lesssim 40$ GHz, while thermal dust emission is evident at 94 GHz. The least contaminated channel is at 61 GHz. We present a model of polarized foreground emission that captures the large angular scale characteristics of the microwave sky.

After applying a Galactic mask that cuts 25.7% of the sky, we show that the high Galactic latitude rms polarized foreground emission, averaged over $\ell = 4-6$, ranges from $\approx 5 \mu\text{K}$ at 22 GHz to $\lesssim 0.6 \mu\text{K}$ at 61 GHz. By comparison, the levels of intrinsic CMB polarization for a ΛCDM model with an optical depth of $\tau = 0.09$ and assumed tensor to scalar ratio $r = 0.3$ are $\approx 0.3 \mu\text{K}$ for E-mode polarization and $\approx 0.03 \mu\text{K}$ for B-mode polarization. To analyze the maps for CMB polarization at $\ell < 16$, we subtract a model of the foreground emission.

In the foreground corrected maps, we detect $\ell(\ell+1)C_{\ell<2-6}^{EE}/2\pi = 0.086 \pm 0.029 (\mu\text{K})^2$. This is interpreted as the result of rescattering of the CMB by free electrons released during reionization at $z_r = 10.9^{+2.7}_{-2.3}$ for a model with instantaneous reionization. By computing the likelihood of just the EE data as a function of τ we find $\tau = 0.10 \pm 0.03$. When the same EE data are used in the full six parameter fit to all WMAP data (TT, TE, EE), we find $\tau = 0.09 \pm 0.03$.

We see no evidence for B-modes, limiting them to $\ell(\ell+1)C_{\ell<2-6}^{BB}/2\pi = -0.04 \pm 0.03 (\mu\text{K})^2$. We perform a template fit to the E-mode and B-mode data with an approximate model for the tensor scalar ratio. We find that the limit from the polarization signals alone is $r < 2.2$ (95% CL) where r is evaluated at $k = 0.002 \text{ Mpc}^{-1}$. This corresponds to a limit on the cosmic density of gravitational waves of $\Omega_{GW}h^2 < 5 \times 10^{-12}$. From the full WMAP analysis, we find $r < 0.55$ (95% CL) corresponding to a limit of $\Omega_{GW}h^2 < 1 \times 10^{-12}$ (95% CL). The limit on r is approaching the upper bound of predictions for some of the simplest models of inflation, $r \sim 0.3$.

Subject headings: cosmic microwave background, polarization, cosmology: observations

1. INTRODUCTION

The temperature anisotropy in the cosmic microwave background is well established as a powerful constraint on theories

of the early universe. A related observable, the polarization anisotropy of the CMB, gives us a new window into the physical conditions of that era. At large angular scales the polarization has the potential to be a direct probe of the universe at an age of 10^{-35} s as well as to inform us about the ionization history of the universe. This paper reports on the direct detection of CMB polarization at large angular scales and helps set a foundation for future observations. It is one of four related papers on the three-year WMAP analysis: Jarosik et al. (2006) report on systematic errors and mapmaking, Hinshaw et al. (2006) on the temperature anisotropy and basic results, and Spergel et al. (2006) on the parameter estimation and cosmological significance.

The polarization of the CMB was predicted soon after the discovery of the CMB (Rees 1968). Since then, considerable advances have been made on both theoretical and observational fronts. The theoretical development (Basko & Polnarev 1980; Kaiser 1983; Bond & Efstathiou 1984; Polnarev 1985; Bond & Efstathiou 1987; Crittenden et al. 1993; Harari & Zaldarriaga 1993; Freun et al. 1994; Coulson et al. 1994; Crittenden et al. 1995; Zaldarriaga & Harari 1995; Kosowsky 1996; Seljak 1997; Zaldarriaga & Seljak 1997; Kamionkowski et al. 1997) has evolved to where there are precise predictions and a common language to describe the

¹ Dept. of Physics, Jadwin Hall, Princeton University, Princeton, NJ 08544-0708

² Code 665, NASA/Goddard Space Flight Center, Greenbelt, MD 20771

³ Dept. of Physics and Astronomy, University of British Columbia, Vancouver, BC Canada V6T 1Z1

⁴ Depts. of Astrophysics and Physics, KICP and EFI, University of Chicago, Chicago, IL 60637

⁵ Dept. of Astrophysical Sciences, Peyton Hall, Princeton University, Princeton, NJ 08544-1001

⁶ Dept. of Physics, Brown University, 182 Hope St., Providence, RI 02912-1843

⁷ UCLA Astronomy, PO Box 951562, Los Angeles, CA 90095-1562

⁸ 612 Space Sciences Building, Cornell University, Ithaca, NY 14853

⁹ Canadian Institute for Theoretical Astrophysics, 60 St. George St, University of Toronto, Toronto, ON Canada M5S 3H8

¹⁰ Dept. of Physics & Astronomy, The Johns Hopkins University, 3400 N. Charles St., Baltimore, MD 21218-2686

¹² Univ. of Texas, Austin, Dept. of Astronomy, 2511 Speedway, RLM 15.306, Austin, TX 78712

¹³ Univ. of Pennsylvania, Dept. of Physics and Astronomy, Philadelphia, PA 19104

¹⁴ Hubble Fellow

Electronic address: page@princeton.edu

polarization signal. Hu & White (1997) give a pedagogical overview.

The first limits on the polarization were placed by Penzias & Wilson (1965), followed by Caderni et al. (1978); Nanos (1979); Lubin & Smoot (1979, 1981); Lubin et al. (1983); Wollack et al. (1993); Netterfield et al. (1997); Sironi et al. (1997); Torbet et al. (1999); Keating et al. (2001) and Hedman et al. (2002). In 2002, the DASI team announced a detection of CMB polarization at sub-degree angular scales based on 9 months of data from a 13 element 30 GHz interferometer (Kovac et al. 2002; Leitch et al. 2002). The signal level was consistent with that expected from measurements of the temperature spectrum. The DASI results were confirmed and extended (Leitch et al. 2005) almost contemporaneously with the release of the CBI (Readhead et al. 2004) and CAPMAP (Barkats et al. 2005) results. More recently, the Boomerang team has released its measurement of CMB polarization (Montroy et al. 2005). All of these measurements were made at small angular scales ($\ell > 100$). Of the experiments that measure the polarization, the DASI, CBI, and Boomerang (Piacentini et al. 2005) teams also report detections of the temperature-polarization cross correlation.

The CMB polarization probes the evolution of the decoupling and reionization epochs. The polarization signal is generated by Thompson scattering of a local quadrupolar radiation pattern by free electrons. The scattering of the same quadrupolar pattern in a direction perpendicular to the line of sight to the observer has the effect of isotropizing the quadrupolar radiation field. The net polarization results from a competition between these two effects. We estimate the magnitude of the signal following Basko and Polnarev (1980). By integrating the Boltzmann equation for the photon distribution they show that the ratio of the polarization anisotropy (E_{rms}) to the temperature (T_{rms}) signal in a flat cosmology is given by

$$\frac{E_{rms}}{T_{rms}} = \frac{\int_0^\infty [e^{-0.3\tau(z')} - e^{-\tau(z')}] \sqrt{1+z'} dz'}{\int_0^\infty [6e^{-\tau(z')} + e^{-0.3\tau(z')}] \sqrt{1+z'} dz'}, \quad (1)$$

where $\tau(z) = c\sigma_T \int_0^z n_e(z') dz' (dt/dz')$ is the optical depth. Here, σ_T is the Thompson cross section, c is the speed of light, and n_e is the free electron density. The difference in brackets in the numerator sets the range in z over which polarization is generated. For example, if the decoupling epoch entailed an instantaneous transition from an extremely high optical depth ($\tau \gg 1$) to transparency ($\tau = 0$), there would be no polarization signal.

To estimate the polarization fraction we compute the optical depth using ordinary atomic physics and the thermal history of the universe (Peebles 1968; Zeldovich et al. 1969). The result is shown in Figure 1. From inserting $\tau(z)$ in Equation 1, we find that the expected level of polarization anisotropy is $\approx 5\%$ (in E_{rms}/T_{rms}) of the anisotropy.

The polarization producing quadrupole is generated by different mechanisms at different epochs. Near decoupling at $z_d = 1088$ (Page et al. 2003b; Spergel et al. 2003), velocity gradients in the flow of the primordial plasma give rise to the quadrupole. More specifically, in the rest frame of an electron in such a flow, the radiation background has a quadrupolar pattern proportional to the velocity gradient, $\nabla \vec{v}$, and the mean free path between scatterings, λ . Just before decoupling, $z > z_d$, the photons are tightly coupled to the electrons and λ is small. Thus, the polarization is small. As decoupling

proceeds λ increases and the quadrupole magnitude increases. The process is cut off at lower redshift because the optical depth drops so rapidly. In the context of inflationary cosmology, Harari & Zaldarriaga (1993) show that in Fourier space the polarization signal is $\propto k\nu\Delta$ where k is the wavevector and $\Delta \approx \lambda$ is the width of the last scattering surface.

After decoupling there are no free electrons to scatter the CMB until the first generation of stars ignite and reionize the universe at z_r . The free electrons then scatter the intrinsic CMB quadrupole, $C_2(z_r)$, and produce a polarized signal $\propto C_2(z_r)^{1/2} \tau(z_r)$. As this process occurs well after decoupling, the effects of the scattering are manifest at comparatively lower values of ℓ . We expect the maximum value of the signal to be at $\ell_{max} \approx \pi/\theta_H(z_r)$ where $\theta_H(z_r)$ is the current angular size of the horizon at reionization. For $6 < z < 30$ a simple fit gives $\theta_H(z) = 4.8/z^{0.7}$, so that for $z_r = 12$, $\ell_{max} \approx 4$. Thus, the signature of reionization in polarization is cleanly separable from the signature of decoupling.

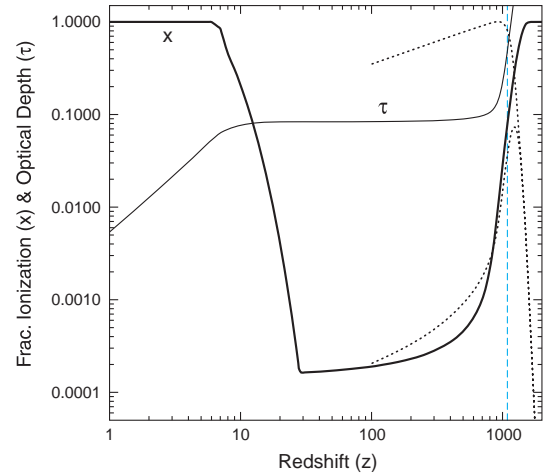


FIG. 1.— A model of the ionization history of the universe. The line marked “x” is the ionization fraction, $x = n_e/n$ where n_e is the number of electrons and $n = 11.2\omega_b(1+z)^3 \text{ m}^{-3}$ is the number of protons with ω_b the baryon density. From quasar absorption systems we know the universe has been fully ionized since at least $z \approx 6$. Between $6 \lesssim z \lesssim 30$ the first generation of stars ionized the universe. We show a possible model inspired by Holder et al. (2003). The history for this period is uncertain though the reionization produces a characteristic signature in the CMB polarization. For $30 < z < 2000$, we show decoupling as described in Peebles (1993). The line marked τ is the net optical depth, $\tau(z)$. The dashed curves are the integrands in the numerator (bottom) and denominator (top) of equation 1 (divided by 200) for the $100 < z < 2000$ region. By eye, one can see that the ratio of the integrals at the maximum, and thus the fractional polarization, is $\approx 5\%$. The vertical line marks the redshift of decoupling, $z_{dec} = 1088$, at the maximum of the visibility function (not shown).

In the first data release the WMAP team published a measurement of the temperature-polarization (TE) cross spectrum for $2 < \ell < 450$ (Bennett et al. 2003b; Kogut et al. 2003) with distinctive anti-peak and peak structure (Page et al. 2003b). The $\ell > 16$ part of the spectrum was consistent with the prediction from the temperature power spectrum, while the $\ell < 16$ part showed an excess that was interpreted as reionization at $11 < z_r < 30$ (95% CL).

This paper builds on and extends these results. Not only are there three times as much data, but the analysis has improved

significantly: 1) The polarization mapmaking pipeline now self-consistently includes almost all known effects and correlations due to instrumental systematics, gain and offset drifts, unequal weighting, and masking (Jarosik et al. 2006). For example, the noise matrix is no longer taken to be diagonal in pixel space, leading to new estimates of the uncertainties. 2) The polarization power spectrum estimate now consistently includes the temperature, E and B modes (defined below), and the coupling between them (see also Hinshaw et al. 2006). 3) The polarized foreground emission is now modeled and subtracted in pixel space (§4.3). Potential residual contamination is examined ℓ by ℓ as a function of frequency. In addition to enabling the production of full sky maps of the polarization and their power spectra, the combination of these three improvements has led to a new measure of the $\ell < 16$ TE and EE spectra, and therefore a new evaluation of the optical depth based primarily on EE. The rest of the paper is organized as follows: we discuss the measurement in §2 and consider systematic errors and maps in §3. In §4 we discuss foreground emission. We then consider, in §5 and §6, the polarization power spectra and their cosmological implications. We conclude in §7.

2. THE MEASUREMENT

WMAP measures the difference in intensity between two beams separated by $\approx 140^\circ$ in five frequency bands centered on 23, 33, 41, 61, and 94 GHz (Bennett et al. 2003b; Page et al. 2003b; Jarosik et al. 2003a). These are called K, Ka, Q, V, and W bands respectively. Corrugated feeds (Barnes et al. 2002) couple radiation from back-to-back telescopes to the differential radiometers. Each feed supports two orthogonal polarizations aligned so that the unit vectors along the direction of maximum electric field for an A-side feed follow $(x_s, y_s, z_s) \approx (\pm 1, -\sin 20^\circ, -\cos 20^\circ)/\sqrt{2}$ in spacecraft coordinates (Page et al. 2003b). For a B-side feed, the directions are $(x_s, y_s, z_s) \approx (\pm 1, \sin 20^\circ, -\cos 20^\circ)/\sqrt{2}$. The z_s axis points toward the Sun along the spacecraft spin axis; the y_s - z_s plane bisects the telescopes and is perpendicular to the radiator panels (Bennett et al. 2003b, Figure 2) (Page et al. 2003b, Figure 1). The angle between the spacecraft spin axis and the optical axis is $\approx 70^\circ$. Thus the two polarization axes on one side are oriented roughly $\pm 45^\circ$ with respect to the spin axis.

The polarization maps are derived from the difference of two differential measurements (Jarosik et al. 2006; Kogut et al. 2003; Hinshaw et al. 2003b). One half of one differencing assembly (DA) (Jarosik et al. 2003a) measures the difference between two similarly oriented polarizations, ΔT_1 , from one feed on the A side and one feed on the B side (e.g., W41: polarization 1 of the 4th W-band DA corresponding to $x_s = +1$ in both expressions above). The other half of the DA measures the difference between the other polarizations in the same pair of feeds, ΔT_2 (e.g., W42: polarization 2 of the 4th W-band DA corresponding to $x_s = -1$ in both the expression above). The polarization signal is proportional to $\Delta T_1 - \Delta T_2$. In other words, WMAP measures a double difference in polarized intensity, not the intensity of the difference of electric fields as with interferometers and correlation receivers (e.g., Leitch et al. 2002; Keating et al. 2001; Hedman et al. 2002).

With these conventions, the total intensity and polarization signals as measured at the output of the detectors are (Kogut et al. 2003, Eq. 3&4):

$$\Delta T_i \equiv \frac{1}{2}(\Delta T_1 + \Delta T_2) = I(\hat{n}_A) - I(\hat{n}_B) \quad (2)$$

$$\Delta T_P \equiv \frac{1}{2}(\Delta T_1 - \Delta T_2) \quad (3)$$

$$= Q(\hat{n}_A) \cos 2\gamma_A + U(\hat{n}_A) \sin 2\gamma_A \\ - Q(\hat{n}_B) \cos 2\gamma_B - U(\hat{n}_B) \sin 2\gamma_B. \quad (4)$$

where n_A and n_B are the unit vectors for the A and B sides; I , Q , and U are the Stokes parameters¹⁴, and γ is the angle between the polarization direction of the electric field and the Galactic meridian (Kogut et al. 2003). In the mapmaking algorithm (Wright et al. 1996; Hinshaw et al. 2003b; Jarosik et al. 2006), I , Q , and U maps of the sky are produced from the time-ordered differential measurements, ΔT_i and ΔT_P . From these, we form maps of polarization intensity, $P = \sqrt{Q^2 + U^2}$, and direction, $\gamma = \frac{1}{2} \tan^{-1}(U/Q)$. This convention has γ positive for North through West and follows the convention in Zaldarriaga & Seljak (1997) and HEALPix (Górski et al. 1998). However, it differs from the standard astronomical position angle (PA) which has $\gamma_{PA} = \frac{1}{2} \tan^{-1}(-U/Q)$ with γ_{PA} positive for North through East. The choice of convention does not affect the plots.

For linear polarization in a given pixel, the Q and U quantities are related to the x and y components of the electric field, E_x, E_y , through the coherency matrix (Born & Wolf 1980):

$$\begin{pmatrix} \langle E_x E_x^* \rangle & \langle E_x E_y^* \rangle \\ \langle E_y E_x^* \rangle & \langle E_y E_y^* \rangle \end{pmatrix} = \frac{1}{2} \begin{pmatrix} I & 0 \\ 0 & I \end{pmatrix} + \frac{1}{2} \begin{pmatrix} Q & U \\ U & -Q \end{pmatrix} \\ = \frac{I}{2} \begin{pmatrix} 1 & 0 \\ 0 & 1 \end{pmatrix} + \frac{P}{2} \begin{pmatrix} \cos 2\gamma & \sin 2\gamma \\ \sin 2\gamma & -\cos 2\gamma \end{pmatrix} \quad (5)$$

where we have set Stokes $V = 0$. The polarized component of the coherency matrix is a spin-two field on a sphere; the total power is the trace of the coherency matrix.

The Crab Nebula [Tau A, 3C144, RA = 05^h34^m31^s, Dec = 22°01' (J2000)] is the brightest polarized point source in the sky and provides a useful end-to-end check of the sign conventions and mapmaking pipeline. Figure 2 shows our measurement of the Crab in Q band (41 GHz) in I , Q , U , P , and γ . Note that its polarization direction ($U \approx 0$, Q negative), is perpendicular to the polarization of the Galaxy ($U \approx 0$, Q positive). The WMAP polarization direction and intensity are in general agreement with previous measurements. Table 1 summarizes the results in all five frequency bands and previous measurements in our frequency range. A second check is needed to fully resolve the sign convention. In Figure 2 we show that the polarization direction of the Centaurus A galaxy [Cen A, NGC5128, RA = 13^h25^m27^s, Dec = -43°01'09" (J2000)] is consistent with that measured by Junkes et al. (1993).

Figures 3 and 4 show the P and γ maps of the full sky for all five frequency bands in Galactic coordinates. Figure 5 shows a Lambert equal area projection of the Galactic polar region in K band. A number of features are immediately apparent to the eye. K band is strongly polarized over a large fraction of the sky, including the polar region. The North Polar Spur and its southern extension are clearly evident. The polarization has a coherent structure over large swaths of sky which translates into significant emission at low ℓ . The polarization intensity decreases with increasing frequency but follows the same pattern. K band is a good monitor of polarized foreground emission as discussed below. Though not immediately apparent to the eye, there is somewhat more polarized emission at W band than V band. The uneven weighting due to the

¹⁴ Italics are used to distinguish between the similarly notated Q band and Q Stokes parameter.

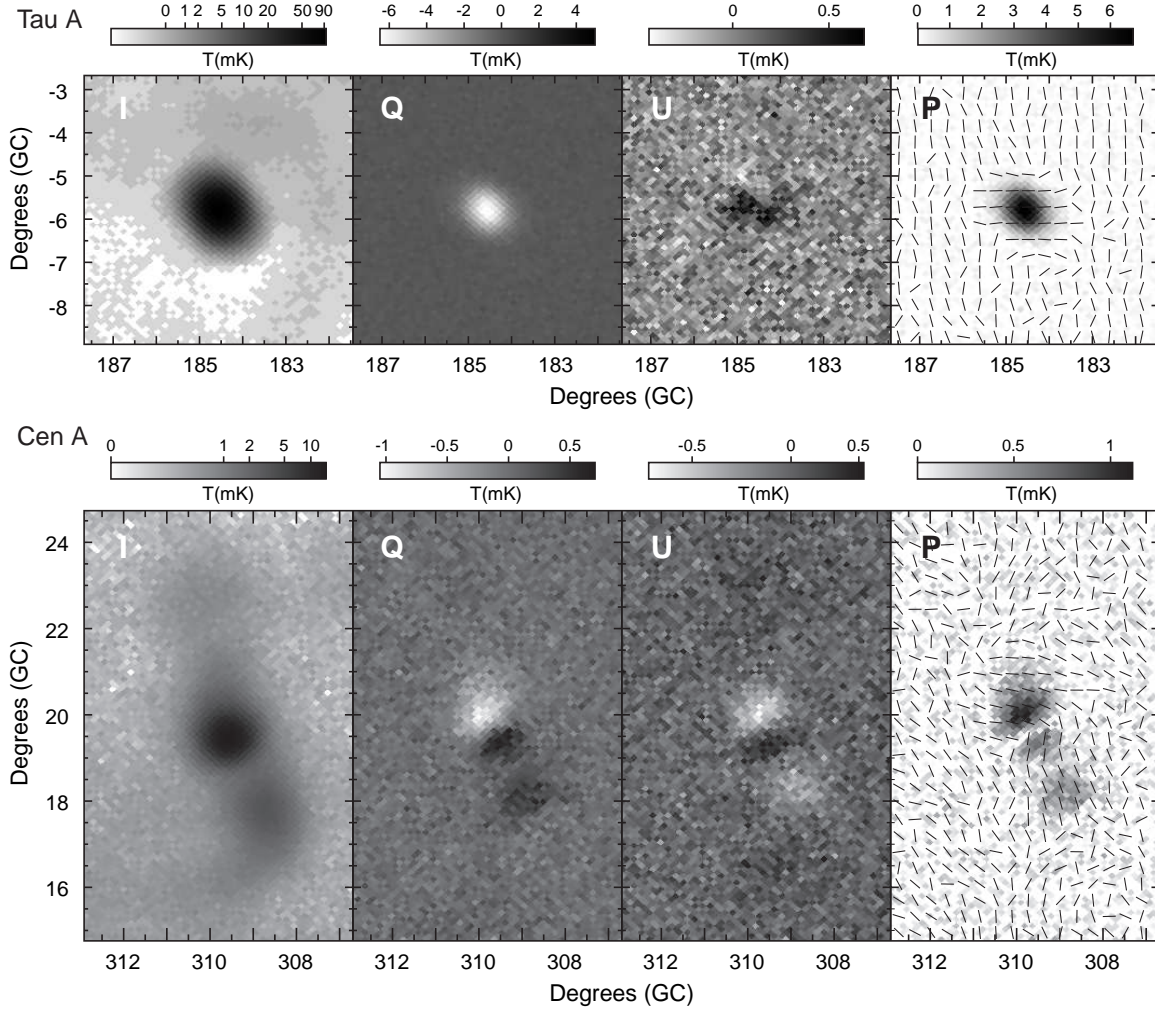


FIG. 2.— *Top*: Map of Tau A in Galactic coordinates at 41 GHz in Stokes I , Q , U , P , smoothed to 1° . Since Tau A is polarized parallel to the Galactic plane it is negative in Q and small in U . *Bottom*: Map of Centaurus A in Stokes I , Q , U , and P . For both sets of plots, Stokes I is scaled logarithmically and all the others are scaled linearly. The scaling in mK is indicated above the grayscale wedge for each panel. A map of the noise bias has been subtracted from the P images.

scan strategy is also evident as increased noise in the ecliptic plane (Bennett et al. 2003b, Figure 4). Figure 6 shows the K and Ka bands in Stokes Q and U .

While foreground emission is visible with a high signal to noise ratio, the CMB polarization anisotropy is not, a situation unlike that for the temperature anisotropy.

3. SYSTEMATIC ERRORS

Detection of the CMB polarization requires tight control of systematic errors, as small couplings to the temperature field or instrument will dominate the polarization signal. *WMAP*'s differential nature and interlocked scan strategy suppress potential polarization systematics in ways similar to the suppression for temperature systematics. The details are different however, and more complex because of the tensorial nature of the polarization field and the double difference required to measure the polarization. Throughout our analyses, the overall level of systematic contamination is assessed with null tests as described here and in Jarosik et al. (2006) & Hinshaw et al. (2006).

The mapmaking procedure is described in Jarosik et al. (2006). End-to-end simulations of the instrument and scan strategy, incorporating realistic models of the frequency re-

sponse, foreground emission, and detector noise characteristics, are used to assess the possible levels of contamination. Interactions between the slow $< 1\%$ drifts in the gain, non-uniform weighting across the sky, the 0.2% correlation due to the oppositely directed beams, the time series masking of the planets, and the $1/f$ noise are accounted for in the map solution. In the following we discuss how the instrumental offset, gain/calibration uncertainty, passband mismatch, main beam mismatch, polarization isolation and cross polarization, loss imbalance, and sidelobes affect the polarization maps.

Offset and baseline drift— The instrumental offset is the output of the detector in the absence of celestial signal. The average polarization offset in the Q , V , and W bands is 250 mK. Changes in this offset on time scales of minutes to hours arise from spacecraft temperature changes and from $1/f$ drifts in the amplifier gain acting on the 250 mK. To measure polarization at the level of $0.1 \mu\text{K}$, we require that changes in the baseline be suppressed by roughly a factor of 10^6 . The first step in achieving this is maintaining a stable instrument and environment. The physical temperature of the DAs averaged over a spin period changes by less than 5 parts in 10^6 (Jarosik et al. 2006), suppressing changes in the baseline by a similar factor. The second step in achieving this

TABLE 1
POLARIZATION OF TAU A

Measurement	Band	Frequency (GHz)	I [Jy]	Q [Jy]	U [Jy]	P/I [%]	γ_{PA} [deg]
WMAP	K	22.5	352 ± 11	-24.7 ± 0.8	1.3 ± 0.9	7.0 ± 0.3	-88° (150°)
WMAP	Ka	32.8	322 ± 6	-22.2 ± 2.0	1.9 ± 1.1	6.9 ± 0.3	-87° (151°)
WMAP	Q	40.4	299 ± 6	-19.6 ± 2.6	0.5 ± 2.4	6.6 ± 0.9	-89° (149°)
WMAP	V	60.2	265 ± 7	-18.5 ± 2.7	-1.9 ± 6.2	7.0 ± 1.1	-93° (145°)
WMAP	W	92.9	229 ± 11	-17.5 ± 4.4	-1.3 ± 7.2	7.6 ± 2.0	-92° (146°)
Mayer & Hollinger (1968)		19				6.6 [15.5]	($140^\circ \pm 10$)
Wright & Forster (1980)		23				9	(152°)
Johnston & Hobbs (1969)		31				8.1 [17]	(158°)
Flett & Henderson (1979)		33				[16]	($154^\circ 8 \pm 2$)
Matveenko & Conklin (1973)		86				(23 ± 3)	
Montgomery et al. (1971)		88				13	(152°)
Hobbs et al. (1978)		99				[11.9 \pm 0.9]	(123°)
Flett & Murray (1991)		273				[27 \pm 1]	($146^\circ \pm 2$)
Greaves et al. (2003)		363				25 \pm 5	($150^\circ \pm 6$)

The fluxes are integrated over pixels within a radius that includes 99% of the beam solid angle, $r_{99} = [2.^\circ 525, 1.^\circ 645, 1.^\circ 517, 1.^\circ 141, 0.^\circ 946]$ degrees in K through W bands. The errors are 1σ estimates calculated as a quadrature sum of statistical error, error due to background uncertainty, confusion error, 0.5% calibration error, and an additional 1% error since the aperture radius doesn't include all of the beam solid angle. Confusion error was calculated as the maximum difference in derived flux when the aperture radius and annulus radius are both decreased by 20% or increased by 20%. Confusion error is usually the largest contribution to the total error. The frequencies are band center frequencies for Tau A's antenna temp spectral index, $\beta = -2.3$. The two numbers for γ_{PA} correspond to Galactic and equatorial (in parentheses) coordinates. Non-WMAP measurements are generally done with arcminute resolution and therefore have different average and peak (in square brackets) fractional polarization. Their polarization directions are all in equatorial coordinates.

is through the baseline removal in the mapmaking algorithm (Hinshaw et al. 2003b; Jarosik et al. 2006).

If the precession of the satellite were stopped, the temperature data for $\ell > 1$ would repeat in the time stream at the spin period (2.16 m). The offset, though, would change sign relative to the celestial signal at half the spin period enabling the differentiation of celestial and instrumental signals. By contrast, with our choice of polarization orientations, the polarization data ΔT_P , would repeat at half the spin period for some orientations of the satellite. Consequently, an instrumental offset would not change sign relative to a celestial signal upon a 180° spacecraft rotation. Thus the polarization data are more sensitive to instrumental offsets than are the temperature data. In general, the polarization data enters the time stream in a more complex manner than does the temperature data.

Calibration— An incorrect calibration between channels leads to a leakage of the temperature signal into ΔT_P , contaminating the polarization map. Calibration drifts cause a leakage that varies across the sky. Jarosik et al. (2003a) show that calibration drifts on ≈ 1 day time scales are the result of sub-Kelvin changes in the amplifier's physical temperature. The calibration can be faithfully modeled by fitting to the physical temperature of each DA with a three parameter model. Here again WMAP's stability plays a key role. The residual calibration errors are at the $\approx 0.2\%$ level. These errors do not limit the polarization maps because the bright Galactic plane is masked in the time ordered data when producing the high Galactic latitude maps (Jarosik et al. 2006). The overall absolute calibration uncertainty is still the first-year value, 0.5% (Jarosik et al. 2006).

Passband mismatch— The effective central frequencies (Jarosik et al. 2003b; Page et al. 2003b) for ΔT_1 and ΔT_2 are not the same. This affects both the beam patterns, treated below, and the detected flux from a celestial source, treated in

the following. The passbands for the A and B sides of one polarization channel in a DA may be treated as the same because the dominant contributions to the passband definition, the amplifiers and band defining filters, are common to both sides.

Since WMAP is calibrated on the CMB dipole, the presence of a passband mismatch means that the response to radiation with a non-thermal spectrum is different from the response to radiation with a CMB spectrum (Kogut et al. 2003; Hinshaw et al. 2003b). This would be true even if the sky were unpolarized, the polarization offset zero, and the beams identical. The effect produces a response in the polarization data of the form:

$$\begin{aligned} \Delta T_P = \Delta I_1 - \Delta I_2 + \\ Q(\hat{n}_A) \cos 2\gamma_A + U(\hat{n}_A) \sin 2\gamma_A \\ - Q(\hat{n}_B) \cos 2\gamma_B - U(\hat{n}_B) \sin 2\gamma_B. \end{aligned} \quad (6)$$

where ΔI_1 is the unpolarized temperature difference observed in radiometer one, and similarly for ΔI_2 . If these differ due to passband differences, the polarization data will have an output component that is independent of azimuth angle. Given sufficient azimuthal coverage, such a term can be separated from Stokes Q and U in the mapmaking process. We model the polarized signal as $Q \cos 2\gamma + U \sin 2\gamma + S$ where the constant, S , absorbs the signal due to passband mismatch. We solve for the mismatch term simultaneously with Q and U as outlined in Jarosik et al. (2006). Note that we do not need to know the magnitude of the passband mismatch, it is fit for in the mapmaking process. The S map resembles a temperature map of the Galaxy but at a reduced amplitude of 3.5% in K band, 2.5% in the V1 band, and on average $\approx 1\%$ for the other bands. The maps of S agree with the expectations based on the measured passband mismatch.

Beamwidth mismatch— The beamwidths of each polarization on each of the A and B sides are different. The difference

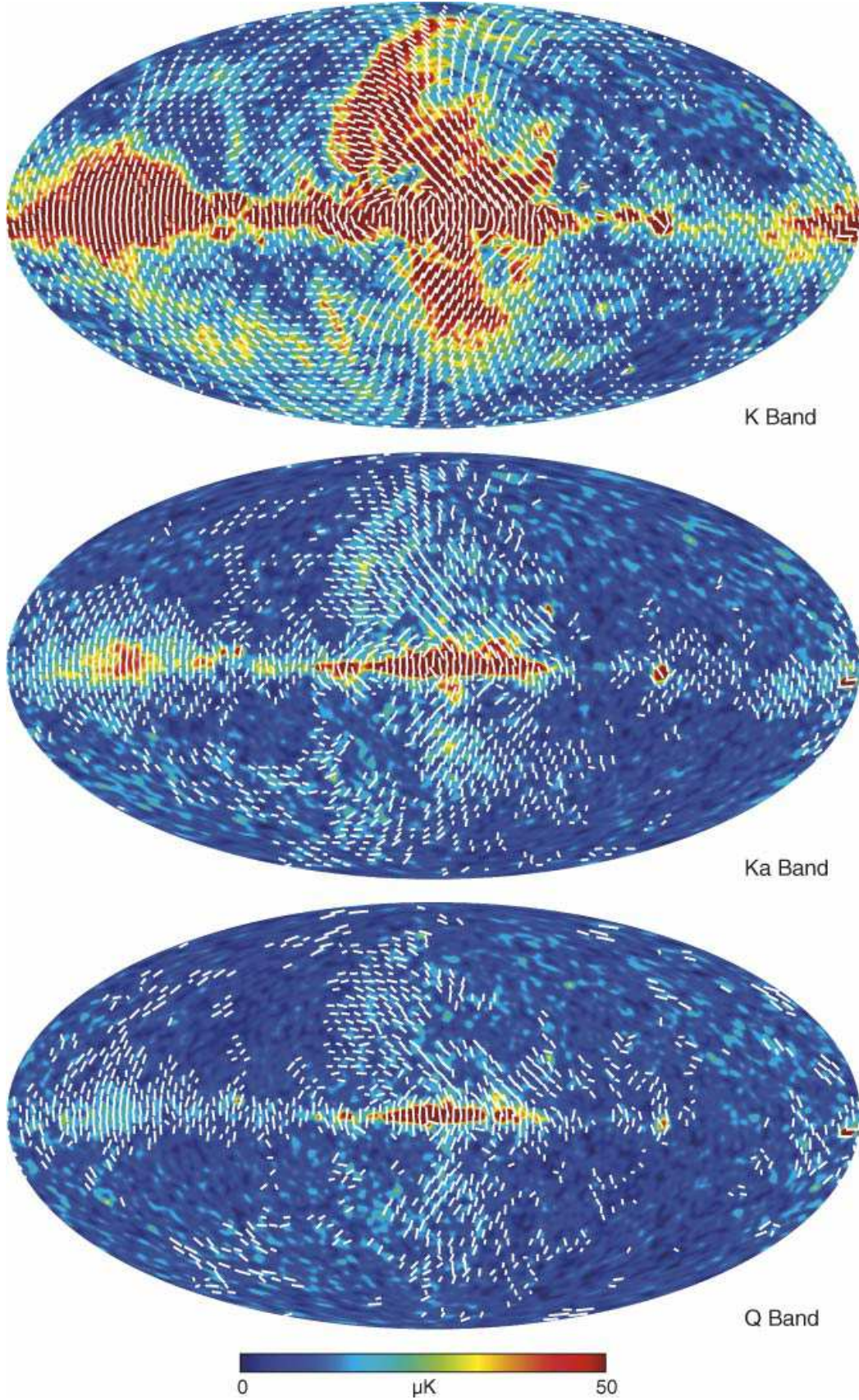


FIG. 3.— P and γ maps for K, Ka, and Q bands in Galactic coordinates. See Bennett et al. (2003b, Figure 4) for features and coordinates. There is only one polarization map for K and Ka bands. For Q band, there are two maps which have been coadded. The maps are smoothed to 2° . The polarization vectors are plotted whenever a r4 HEALPix pixel (see §4.2, roughly $4^\circ \times 4^\circ$) and three of its neighbors has a signal to noise (P/N) greater than unity. The length of the arrow is logarithmically dependent on the magnitude of P . Note that P is positive. Maps of the noise bias have been subtracted in these images.

between the A and B side beam shapes is due to the difference in shapes of the primary mirrors and is self consistently

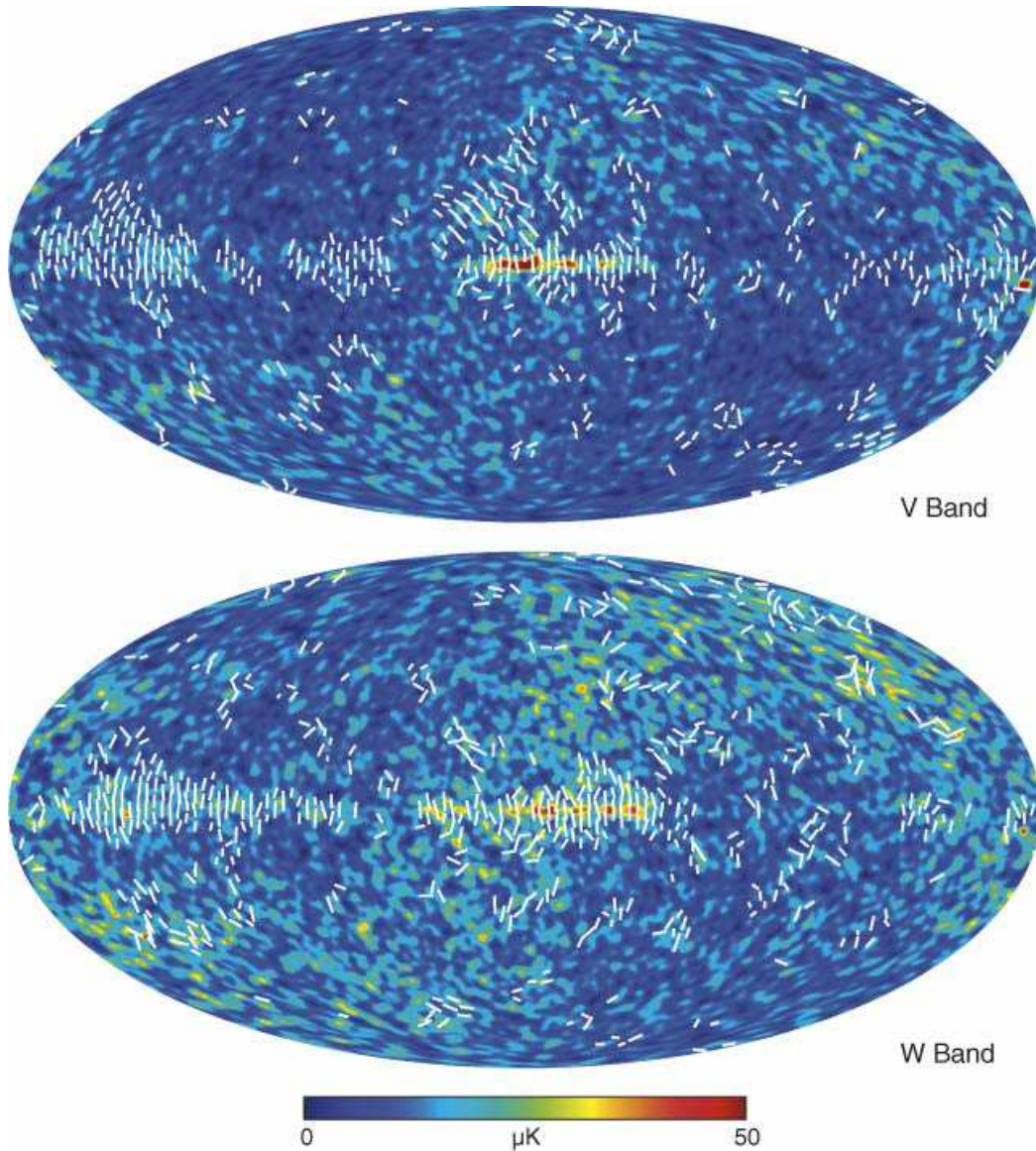


FIG. 4.— Similar to Figure 3 but for V and W bands. The two V-band maps have been coadded as have the four W-band maps. The relatively higher noise in the ecliptic plane is evident. Maps of the noise bias have been subtracted in these images.

treated in the window function (Page et al. 2003b). The difference in beam shapes between ΔT_1 and ΔT_2 is due to the mismatch in central frequencies.¹⁵

This effect is most easily seen in the K-band observations of Jupiter. We denote the brightness temperature and solid angle of Jupiter with T_J and Ω_J , and the measured quantities as \hat{T}_J and $\hat{\Omega}_J$. Although the product $T_J\Omega_J = \hat{T}_J\hat{\Omega}_J$ is the same for the two polarizations (because Jupiter is almost a thermal source in K band), the beam solid angles differ by 8.1% on the A-side and 6.5% on the B-side (Page et al. 2003a). The primary effect of the beamwidth mismatch is to complicate the determination of the intrinsic polarization of point sources.

The difference in beams also leads to a small difference in window functions between ΔT_1 and ΔT_2 . The signature would be leakage of power from the temperature anisotropy into the polarization signal at high ℓ . We have analyzed the

¹⁵ If the passbands were the same, the beam solid angles for ΔT_1 and ΔT_2 would be the same to $< 0.5\%$ accuracy.

data for evidence of this effect and found it to be negligible. Additionally, as most of the CMB and foreground polarization signal comes from angular scales much larger than the beam, the difference in window functions can safely be ignored in this data set.

Polarization isolation and cross polarization—Polarization isolation, X_{cp} , and cross polarization are measures of the leakage of electric field from one polarization into the measurement of the orthogonal polarization. For example, if a source were fully polarized in the vertical direction with intensity I_v and was measured to have intensity $I_h = 0.01I_v$ with a horizontally polarized detector, one would say that the cross polar response (or isolation) is $|X_{cp}|^2 = 1\%$ or -20 dB. The term “polarization isolation” is usually applied to devices whereas “cross polarization” is applied to the optical response of the telescope. We treat these together as a cross-polar response. For WMAP, the off-axis design and imperfections in the orthomode transducers (OMT) lead to a small cross-polar response. The ratio of the maximum of the modeled crosspolar

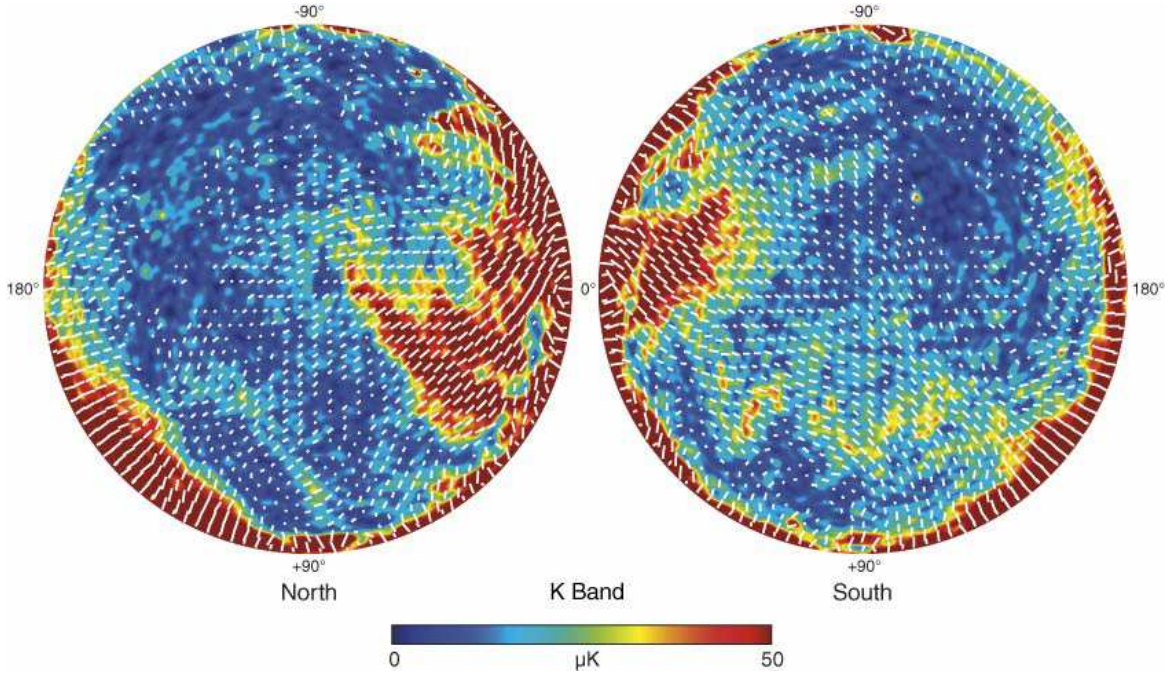


FIG. 5.— A Lambert azimuthal equal area projection of the Galactic poles (*left*: north) showing the K-band polarization. The circumference of each map is at zero Galactic latitude. The convention in this plot is to use bars to indicate the polarization direction. It is clear that the polarization extends to high Galactic latitudes. A map of the noise bias is subtracted from this image.

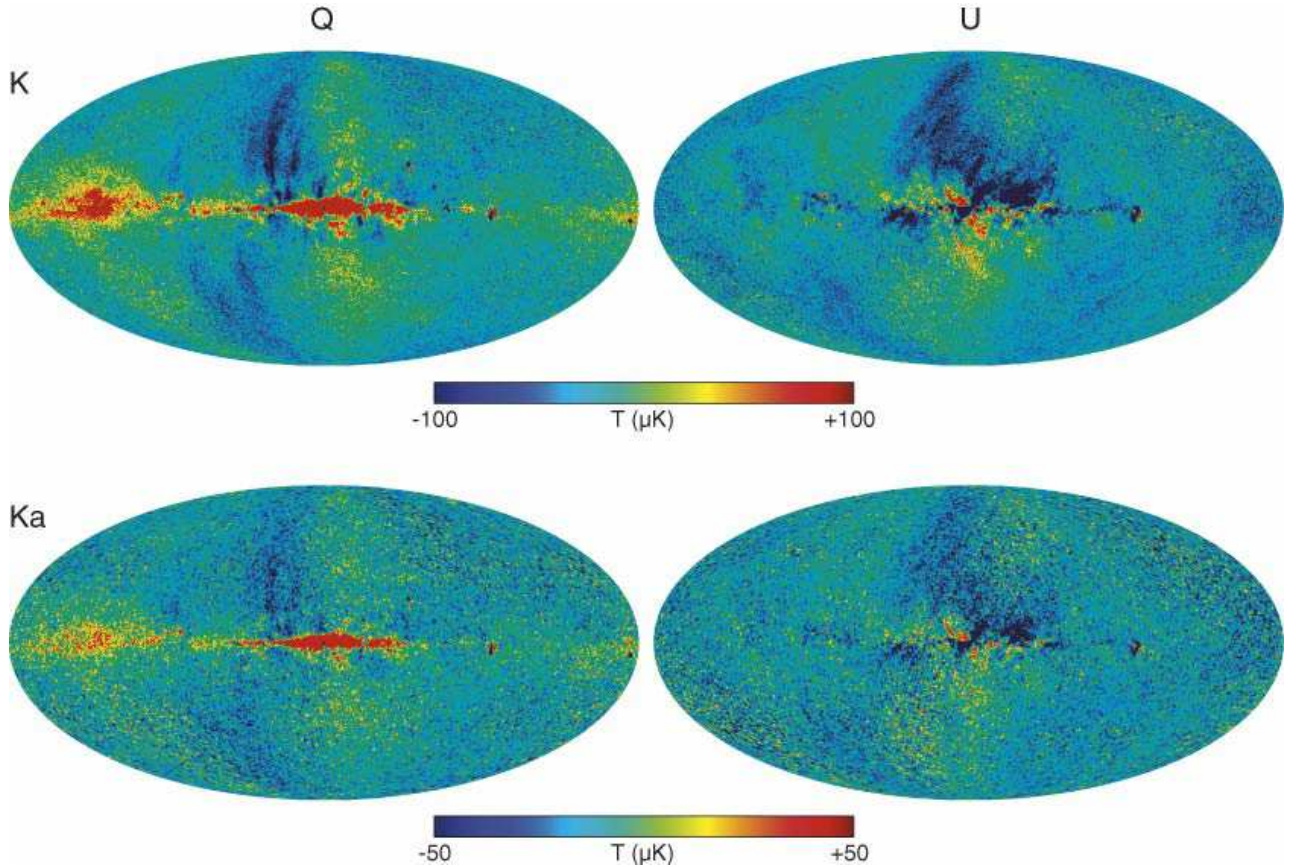


FIG. 6.— Stokes Q and U maps in K and Ka bands. The Galactic plane is dominated by positive Stokes Q because the foreground polarization direction is perpendicular to the plane. As discussed in §4, this is expected because the Galactic magnetic field is predominantly parallel to the plane. For comparison, the Stokes Q and U maps of a noiseless CMB simulation have peak-to-peak values of less than $6 \mu\text{K}$. These maps have been smoothed to 1° .

beam to the maximum of the modeled copolar beam is -25 , -27 , -30 , -30 , & -35 dB in K through W bands respectively.

The determination of the feed and OMT polarization isolation is limited by component measurement. The maximum values we find are: $|X_{cp}|^2 = -40, -30, -30, -27, \& -25$ dB for K through W bands respectively (Page et al. 2003b).

Because WMAP measures only the difference in power from two polarizations, it measures only Stokes Q in a reference frame fixed to the radiometers, Q_{Rad} . The sensitivity to celestial Stokes Q and U comes through multiple observations of a single pixel with different orientations of the satellite. The formalism that describes how cross polarization interacts with the observations is given in Appendix A. To leading order, the effect of a simple cross polarization of the form $X_{cp} = X e^{iY}$ is to rotate some of the radiometer U into a Q component. The measured quantity becomes:

$$\Delta T_P = Q_{Rad}^A + Q_{Rad}^B + 2X \cos(Y)(U_{Rad}^A + U_{Rad}^B) \quad (7)$$

where Q_{Rad}^A and Q_{Rad}^B are the Stokes Q components for the A and B sides in the radiometer frame, similarly with U_{Rad}^A and U_{Rad}^B . Note that in the frame of the radiometers Q_{Rad}^B (Stokes Q in the B-side coordinate system) is $-Q_{Rad}^A$. This leads to the difference in sign conventions between the above and Equation 5. System measurements limit the magnitude of $|X_{cp}|^2$ but do not directly give the phase, Y . Laboratory measurements of selected OMTs show $Y = 90^\circ \pm 5^\circ$, indicating the effective cross polar contamination is negligible.

We limit the net effect of the reflectors and OMT with measurements in the GEMAC antenna range (Page et al. 2003b). We find that for a linearly polarized input, the ratios of the maximum to minimum responses of the OMTs are 1) $-25, -27, -25, -22$ dB for K through W band respectively; 2) $90^\circ \pm 2^\circ$ apart; and 3) within $\pm 1.5^\circ$ of the design orientation. Thus, we can limit any rotation of one component into another to $< 2^\circ$. The comparison of γ derived from Tau A to the measurement by Flett & Henderson (1979) in Table 1 gives further evidence that any possible rotation of the Stokes components is minimal. Based on these multiple checks, we treat the effects of optical cross polarization and incomplete polarization isolation as negligible.

Loss imbalance—A certain amount of celestial radiation is lost to absorption by the optics and waveguide components. If the losses were equal for each of the four radiometer inputs their effect would be indistinguishable from a change in the gain calibration. However, small differences exist that produce a residual common-mode signal that is separable from the gain drifts (Jarosik et al. 2003a). The mean loss difference (\bar{x}_{im}) between the A- and B-sides is accounted for in the mapmaking algorithm (Hinshaw et al. 2003a; Jarosik et al. 2003a). In addition, the imbalance between the two polarizations on a single side, the “loss imbalance imbalance,” is also included (Jarosik et al. 2006). It contributes a term $2(L^A T^A + L^B T^B)$ to ΔT_P . Here $T^{A,B}$ is the sky temperature observed by the A,B side, and $L^{A,B}$ is the loss imbalance between the two polarizations on the A,B side (see Appendix A). The magnitude of $L^{A,B}$ is $\lesssim 1\%$ (Jarosik et al. 2003b).

A change in the loss across the bandpass due to, for example, the feed horns is a potential systematic error that we do not quantify with the radiometer passband measurements (Jarosik et al. 2003b). The magnitude of the effect is second order to the loss imbalance which is 1%. We do not have a measurement of the effect. Nevertheless, as the effect mimics a passband mismatch, it is accounted for in the map solution.

Sidelobes—When the sidelobes corresponding to ΔT_P are measured, there are two terms (Barnes et al. 2003). The

largest term is due to the passband mismatch and is consistently treated in the mapmaking process. The second smaller term is due to the intrinsic polarization. We assess the contribution of both terms by simulating the effects of scan pattern of the sidelobes on the Q and U polarization maps. The results are reported in Barnes et al. (2003) for the first-year polarization maps. In K band, the net rms contamination is $1 \mu\text{K}$ outside of the Kp0 mask region (Bennett et al. 2003b). The intrinsic polarized sidelobe pickup is $< 1 \mu\text{K}$ and is not accounted for in this three-year data release. The contamination is more than an order of magnitude smaller in the other bands.

4. THE FOREGROUND EMISSION MODEL

The microwave sky is polarized at all frequencies measured by WMAP. In K band the polarized flux exceeds the level of CMB polarization everywhere over the full sky. By contrast, unpolarized foreground emission dominates over the CMB only over $\approx 20\%$ of the sky. Near 60 GHz and $\ell \approx 5$, the foreground emission temperature is roughly a factor of two larger than the CMB polarization signal. Thus, a model of the foreground must be subtracted before a cosmological analysis is done. While it is possible to make significant progress working with angular power spectra, we find that due to the correlations between foreground components, a pixel space model is required. Table 2 gives the foreground emission levels in a region around the Galactic center.

TABLE 2
TEMPERATURES IN THE GALACTIC CENTER REGION

Band	I [mK]	Q [mK]	U [mK]
K	33	0.69	-0.25
Ka	14	0.21	-0.086
Q	8.7	0.10	-0.041
V	4.0	0.037	$-0.01 < U < 0.01$
W	3.6	0.043	$-0.01 < U < 0.01$

The table gives the average values for the temperature and Q and U Stokes parameters in a $\delta b = 2^\circ$ by $\delta l = 10^\circ$ region centered on $(l, b) = (0, 0)$. The values are in thermodynamic units relative to the CMB. To convert to antenna temperature, divide by 1.014, 1.029, 1.044, 1.100, 1.251 in K through W bands respectively.

The two dominant components of diffuse polarized foreground emission in the 23–94 GHz range are synchrotron emission and thermal dust emission (Weiss 1984; Bennett et al. 2003b). Free-free emission is unpolarized¹⁶ and spinning dust grains are expected to have polarization fractions of 1–2% (Lazarian & Draine 2000). The signal from polarized radio sources is negligible (Table 9, Hinshaw et al. 2006). The detected polarized sources are all well known, and among the brightest objects in the temperature source catalog. They include 3C273, 3C274 (M87, Vir A), 3C279, Fornax A, Pictor A, [HB93]2255-282, and [HB93] 0637-752 and are masked as discussed below. The potential impact of polarized foreground emission on the detection of the CMB polarization has been discussed by many authors including Verde et al. (2006); Ponthieu et al. (2005); de Oliveira-Costa et al. (2003); Giardino et al. (2002); Tucci et al. (2002); Baccigalupi et al. (2001); Tegmark et al. (2000).

¹⁶ There may be polarized emission at the edges of HII clouds as noted in Keating et al. (1998).

Synchrotron emission is produced by cosmic-ray electrons orbiting in the $\approx 3 \mu\text{G}$ Galactic magnetic field. The unpolarized synchrotron component has been well measured by *WMAP* in the 23 to 94 GHz range (Bennett et al. 2003a). The brightness temperature of the radiation is characterized by $T(\nu) \propto \nu^{\beta_s}$ where the index $-3.1 < \beta_s < -2.5$ varies considerably across the sky (Reich & Reich 1988; Lawson et al. 1987). In the microwave range, the spectrum reddens (β_s tends to more negative values) as the frequency increases (Banday & Wolfendale 1991).

Synchrotron radiation can be strongly polarized in the direction perpendicular to the Galactic magnetic field (Rybicki & Lightman 1979). The polarization has been measured at a number of frequencies [from Leiden between 408 MHz to 1.4 GHz (Brouw & Spoelstra 1976; Wolleben et al. 2005), from Parkes at 2.4 GHz (Duncan et al. 1995, 1999), and by the Medium Galactic Latitude Survey at 1.4 GHz (Uyaniker et al. 1999)]. At these low frequencies, Faraday rotation alters the polarization. Electrons in the Galactic magnetic field rotate the plane of polarization because the constituent left and right circular polarizations propagate with different velocities in the medium. In the interstellar medium, the rotation is a function of electron density, n_e , and the component of the Galactic magnetic field along the line of sight, $B_{||}$,

$$\Delta\theta = 420^\circ \left(\frac{1 \text{ GHz}}{\nu} \right)^2 \int_0^{L/1 \text{ kpc}} dr \left(\frac{n_e}{0.1 \text{ cm}^{-3}} \right) \left(\frac{B_{||}}{1 \mu\text{G}} \right) \quad (8)$$

where the integral is over the line of sight. With $n_e \sim 0.1 \text{ cm}^{-3}$, $L \sim 1 \text{ kpc}$, and $B_{||} \sim 1 \mu\text{G}$, the net rotation is $\Delta\theta \sim 420^\circ/\nu^2$, with ν in GHz. At *WMAP* frequencies the rotation is negligible, though the extrapolation of low frequency polarization measurements to *WMAP* frequencies can be problematic. In addition there may be both observational and astrophysical depolarization effects that are different at lower frequencies (Burn 1966; Cioffi & Jones 1980; Cortigioni & Spoelstra 1995). Thus, our model for subtracting the foreground emission is based, to the extent possible, on the polarization directions measured by *WMAP*.

The other dominant component of polarized foreground emission comes from thermal dust. Nonspherical dust grains align their long axes perpendicularly to the Galactic magnetic field through the Davis-Greenstein mechanism (Davis & Greenstein 1951). The aligned grains preferentially absorb the component of starlight polarized along their longest axis. Thus, when we observe starlight we see it polarized in the same direction as the magnetic field. These same grains emit thermal radiation preferentially polarized along their longest axis, perpendicular to the Galactic magnetic field. Thus we expect to observe thermal dust emission and synchrotron emission polarized in the same direction, while starlight is polarized perpendicularly to both.

In Section §4.1, we describe a model of the polarized microwave emission from our Galaxy that explains the general features of the *WMAP* polarization maps. However this model is not directly used to define the polarization mask or to clean the polarization maps. We go on to define the polarization masks in §4.2 and in §4.3 we describe how we subtract the polarized foreground emission.

4.1. The Galaxy Magnetic Field and a Model of Foreground Emission.

In the following, we present a general model of polarized foreground emission based on *WMAP* observations. We view this as a starting point aimed at understanding the gross features of the *WMAP* data. A more detailed model that includes the wide variety of external data sets that relate to polarization is beyond the scope of this paper.

For both synchrotron and dust emission, the Galactic magnetic field breaks the spatial isotropy thereby leading to polarization. Thus, to model the polarized foreground emission we need a model of the Galactic magnetic field. As a first step, we note that the K-band polarization maps suggest a large coherence scale for the Galactic magnetic field, as shown in Figure 3.

We can fit the large-scale field structure seen in the K-band maps with a gas of cosmic ray electrons interacting with a magnetic field that follows a bisymmetric spiral (BSS) arm pattern. Many external galaxies show similar arm patterns (e.g., Sofue et al. 1986) and the BSS pattern is a good fit to pulsar measurements (Han & Wielebinski 2002). The BSS magnetic field is modeled as:

$$\mathbf{B}(r, \phi, z) = B_0 [\cos \psi(r) \cos \chi(z) \hat{r} + \sin \psi(r) \cos \chi(z) \hat{\phi} + \sin \chi(z) \hat{z}] \quad (9)$$

where $\psi(r) = \psi_0 + \psi_1 \ln(r/8 \text{ kpc})$, $\chi(z) = \chi_0 \tanh(z/1 \text{ kpc})$, r and z are measured in kpc, r ranges from 3 kpc to 20 kpc, and the angles are in degrees. For a fixed radius, $|\mathbf{B}|$ has the same value at all azimuths. We take 8 kpc as the distance to the center of the Galaxy (Eisenhauer et al. 2003; Reid & Brunthaler 2005). The values are determined by fitting to the K-band field directions. While the tilt, $\chi(z)$ with $\chi_0 = 25^\circ$, and the radial dependence, $\psi(r)$ with $\psi_1 = 0.9$, optimize the fit, the key parameter is ψ_0 , the opening angle of the spiral arms. We find that the magnetic field is a loosely wound spiral with $\psi_0 \simeq 35^\circ$.

To model the cosmic ray electrons, we assume they have a power-law distribution with slope ¹⁷ $p = -(2\beta_s + 3) = 3$ (Rybicki & Lightman 1979) and are distributed in a exponential disk with a scale height of $h_d = 1 \text{ kpc}$ and a radial scale length of $h_r = 5 \text{ kpc}$ (e.g., Drimmel & Spergel 2001) as

$$n_e = n_0 \exp(-r/h_r) \text{sech}^2(z/h_d). \quad (10)$$

While the amplitude of the signal is sensitive to the details of the cosmic ray distribution and the magnetic field structure, we may estimate its overall structure with the smooth field model (Eq. 9) and cosmic ray distribution. We compute the polarization direction in this simple model as:

$$\begin{aligned} \tan 2\gamma(\hat{n}) &= \frac{U(\hat{n})}{Q(\hat{n})} \\ &= \frac{\int n_e(x, \hat{n}) 2B_s(x, \hat{n}) B_t(x, \hat{n}) dx}{\int n_e(x, \hat{n}) [B_s^2(x, \hat{n}) - B_t^2(x, \hat{n})] dx} \end{aligned} \quad (11)$$

where \hat{n} is the line-of-sight direction, x is the distance along that direction, n_e is the electron distribution described above, and B_t and B_s are orthogonal components of the field perpendicular to the line of sight, with B_t the component perpendicular to the z axis of the Galactic plane. The parameters of the BSS model are determined by fitting the predicted directions, Equation 11, to the measured the K-band field directions.

¹⁷ Bennett et al. (2003a) uses γ in place of p .

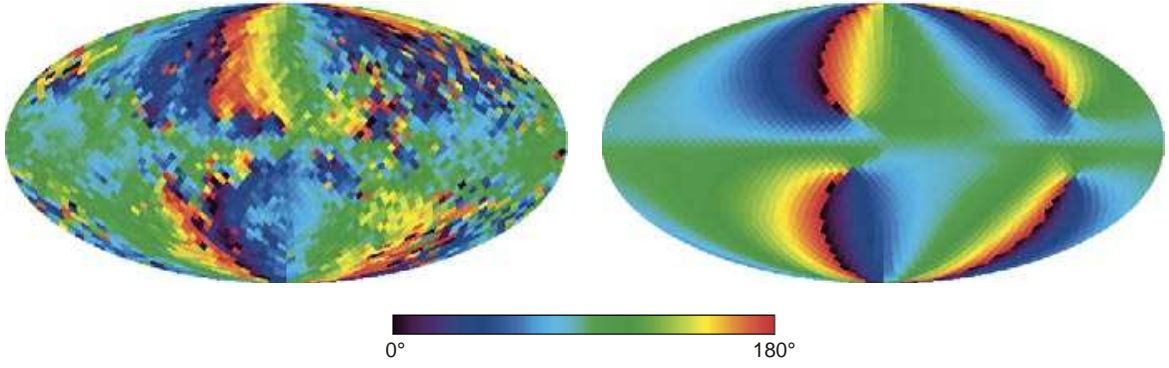


FIG. 7. — *Left*: The angle of the magnetic field, $\gamma_M = \gamma_{PA} + 90^\circ$, derived from the synchrotron radiation in the K-band map (smoothed with a 4° beam) shown in Figure 3. (We do not distinguish between $\pm 180^\circ$ in the field direction.) The predominant low Galactic latitude magnetic field direction is parallel to the Galactic plane ($\gamma_M = 90^\circ$) and thus the synchrotron (and dust) polarization directions have $\gamma \approx 0^\circ$. In the North Polar Spur region, the magnetic field is perpendicular to the Galactic plane corresponding to $\gamma_M \approx 0^\circ$ or 180° . Note the large scale coherency of the field. *Right*: The predicted magnetic field direction given by a simple model of the electron distribution and the bisymmetric spiral arm model (Equation 9) for the magnetic field.

Figure 7 shows the predicted magnetic field directions for the BSS model. In the plane, the field lines are parallel to the Galactic plane and the polarization projects into positive Stokes Q . Near the Galactic pole, the field lines all point along the spiral arm direction. When projected into Q and U , this leads to γ rotating around the pole. We assess the agreement between the model field directions and the directions inferred from the K-band polarization with the correlation coefficient $r = \cos(2(\gamma_{\text{model}} - \gamma_{\text{data}}))$, and take the rms average over 74.3% of the sky (outside the P06 mask described below). For our simple model the agreement is clear: $r = 0.76$ for K band.

For a power law distribution of electrons moving in a homogeneous magnetic field, the polarization fraction is $\Pi_s = (p+1)/(p+7/3) \approx 0.75$ (Rybicki & Lightman 1979). Because the field direction changes as one integrates along the line of sight, there is a geometric suppression of the amplitude of the polarization signal. We estimate this geometric suppression as

$$g_{\text{sync}}(\hat{n}) = \frac{P(\hat{n})}{\Pi_s I(\hat{n})}, \quad (12)$$

where all quantities are determined from the model: $P(\hat{n}) = \sqrt{Q^2 + U^2}$ and I is found by integrating the magnetic field and cosmic ray distribution along the line of sight. The result is shown in Figure 8. This geometric reduction factor ranges from unity to zero and is especially small in the Galactic plane at longitudes near $\ell = -100^\circ$. When compared to the K-band data, the model over suppresses the predicted polarization near $\ell = -100^\circ$ so we enforce $g_{\text{sync}} \geq 0.2$. That is, we globally set $g_{\text{sync}} = 0.2$ where it is initially less than 0.2.

4.1.1. Comparison to Low Frequency Observations

The polarization of edge-on spirals NGC 891 and 4565, which are similar to the Milky Way, has been measured by Sukumar & Allen (1991). The observations are at 5 GHz and thus probe primarily synchrotron emission. They find: (1) at distances ≈ 2 kpc off the galactic plane the polarization fraction can be $\geq 20\%$; and (2) in the plane, heights < 0.5 kpc, the polarization fraction drops to $< 5\%$. Hummel et al. (1991) show that (3) between 0.66 GHz and 1.5 GHz the spectral index ranges from $\beta_s = -2.5$ in the plane to $\beta_s = -3.5$ well off the plane. WMAP observes qualitatively similar behavior in K band.

At 408 MHz, Haslam et al. (1982) have surveyed the Galactic plane in intensity. At this frequency, synchrotron emission

dominates maps. We test the magnetic field model by extrapolating the 408 MHz measurements to 22 GHz (an extrapolation of 40 in frequency and over 10,000 in amplitude):

$$Q_{\text{model}}(\hat{n}) = q I_{\text{Has}}(\hat{n}) \left(\frac{22}{0.408} \right)^{\beta_s} \Pi_s g_{\text{sync}}(\hat{n}) \cos(2\gamma_{\text{model}})$$

$$U_{\text{model}}(\hat{n}) = q I_{\text{Has}}(\hat{n}) \left(\frac{22}{0.408} \right)^{\beta_s} \Pi_s g_{\text{sync}}(\hat{n}) \sin(2\gamma_{\text{model}}) \quad (13)$$

where q is the ratio of the homogeneous field strength to the total field strength. Note that the model effectively has only one free parameter: an overall amplitude, which is described by a degenerate combination of the spectral index, β_s and q . For $\beta_s = -2.7$, the best fit value for q is 0.7. This implies that the energy in the large scale field is roughly the same as the energy in small scale fields, consistent with measurements of external galaxies (Han & Wielebinski 2002) and studies of dust polarization in the Milky Way (Jones et al. 1992).

Figure 9 compares the K band polarization signal to the extrapolated 408 MHz maps. Given the simplicity of the model (uniform cosmic ray spectral index, p , and a uniform BSS field), the agreement is remarkably good. The largest deviations are seen near spiral arms. Recent observations (Enomoto et al. 2002) suggest that cosmic rays are accelerated in star-forming regions. If most cosmic rays are accelerated in spiral arms and then diffuse away from the arms, we would expect a flatter spectral index in the arms, consistent with the observations. In Figure 10 we show that the radio loops (Berkhuijsen et al. 1971) seen at 408 MHz, probably from supernovae or “blowouts,” are also seen in the WMAP data.

4.1.2. Starlight Polarization and Polarized Dust Emission

Measurements of starlight polarization serve as a template for the analysis of polarized microwave dust emission (Fosalba et al. 2002; Bernardi et al. 2003). We have combined several catalogs of optical dust polarization measurements (Heiles 2000; Berdyugin et al. 2001; Berdyugin & Teerikorpi 2002; Berdyugin et al. 2004) to construct a template for the magnetic field direction in dusty environments. Since there are significant variations in the dust column density, we only use the measured direction to construct the dust template. The dust layer has a scale height of 100 pc (Berdyugin & Teerikorpi 2001; Drimmel & Spergel 2001).

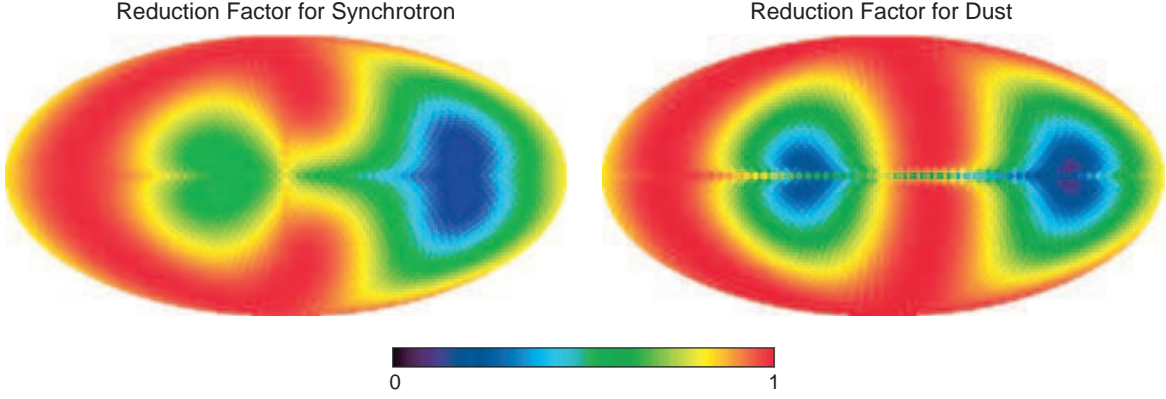


FIG. 8.— The left panel shows the geometric suppression factor, $g_{sync}(\hat{n})$, in the polarization due to the magnetic field geometry. In the region of low polarization, $g_{sync}(\hat{n})$ is bounded to be greater than 0.2. The right panel shows a similar geometric suppression factor for polarized dust emission, $g_{dust}(\hat{n})$, see §4.1.3.

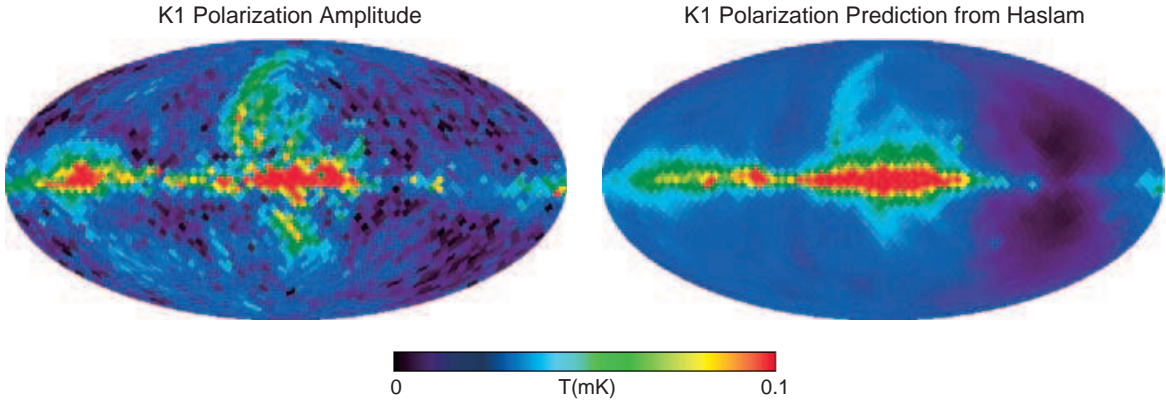


FIG. 9.— *Left*: The observed K-band polarization, P . The color scale ranges from 0 to 0.1 mK. *Right*: The model prediction of the K-band polarization based on the Haslam *intensity* map. The model has one effective free parameter, the ratio of the homogeneous field strength to the total field strength as shown in Equation 13. This plot shows the results for $\beta_s = -2.7$ & $q = 0.7$.

Observations toward the Galactic poles suggest that most of the dust absorption occurs within 200 pc. To select stars outside the dust column for $|b| > 10^\circ$, we limit the sample to the 1578 stars with heliocentric distances greater than 500 pc. For $|b| < 10^\circ$, the model is problematic because there is ample dust emission from distances further away than the stars sample.

We represent the starlight polarization data, (Q_\star, U_\star) , in terms of a polarization amplitude, P_\star and direction, γ_\star :

$$\begin{aligned} Q_\star &= P_\star \cos(2\gamma_\star) \\ U_\star &= P_\star \sin(2\gamma_\star) \end{aligned} \quad (14)$$

We then smooth the starlight data by convolving (Q_\star/P_\star) and (U_\star/P_\star) with a Gaussian window with a FWHM of 9.2° . The smoothing is required because the measurements are coarsely distributed. As a result, this dust model is applicable only for $\ell \lesssim 15$ and $|b| > 10^\circ$. Above, γ_\star describes the direction of this smoothed starlight polarization field. We can quantify the agreement between the starlight and *WMAP* K-band polarization measurements by computing their correlation in each pixel, $z = \cos(2(\gamma_\star - \gamma_K) + \pi)$ where γ_K is the direction in K band. Figure 11 shows a plot of the correlation as a function of position. The median correlation coefficient is 0.72 implying that the dust and K-band directions typically agree to 20° . Because of noise in both the K-band and starlight maps, this is an underestimate of the correlation. Nevertheless, the

correlation tells us that the basic model relating the starlight, the dust, synchrotron emission, and the magnetic field agrees with observations.

4.1.3. Thermal Dust Emission

Based on the detection of starlight polarization, thermal dust emission is expected to be polarized at millimeter and sub-millimeter wavelengths. Archaeops has detected polarized thermal emission at 353 GHz (Benoît et al. 2004). An extrapolation from this high frequency suggests that *WMAP* should see polarized thermal dust emission at 94 GHz. Here, we report on the *WMAP* detection of dust polarization at 94 GHz.

We generate a template for the dust polarization by using the Maximum Entropy Method (MEM) dust intensity map (Bennett et al. 2003a), the smoothed polarization direction from the starlight, and the model geometric factor for the dust layer:

$$\begin{aligned} Q_{dust}(\nu) &= I_{dust}(\hat{n}) \Pi_d g_{dust}(\hat{n}) \cos(2\gamma_{dust}) \\ U_{dust}(\nu) &= I_{dust}(\hat{n}) \Pi_d g_{dust}(\hat{n}) \sin(2\gamma_{dust}) \end{aligned} \quad (15)$$

where $\gamma_{dust} = \gamma_\star + \pi/2$ is the smoothed starlight polarization direction. The geometric suppression factor for the dust, g_{dust} , is computed along the same lines as g_{sync} in Equation 12 and is shown in Figure 8. To compute $I(\hat{n})$ we assume the dust has a scale height of 100 pc and a radial scale length of 3 kpc. To

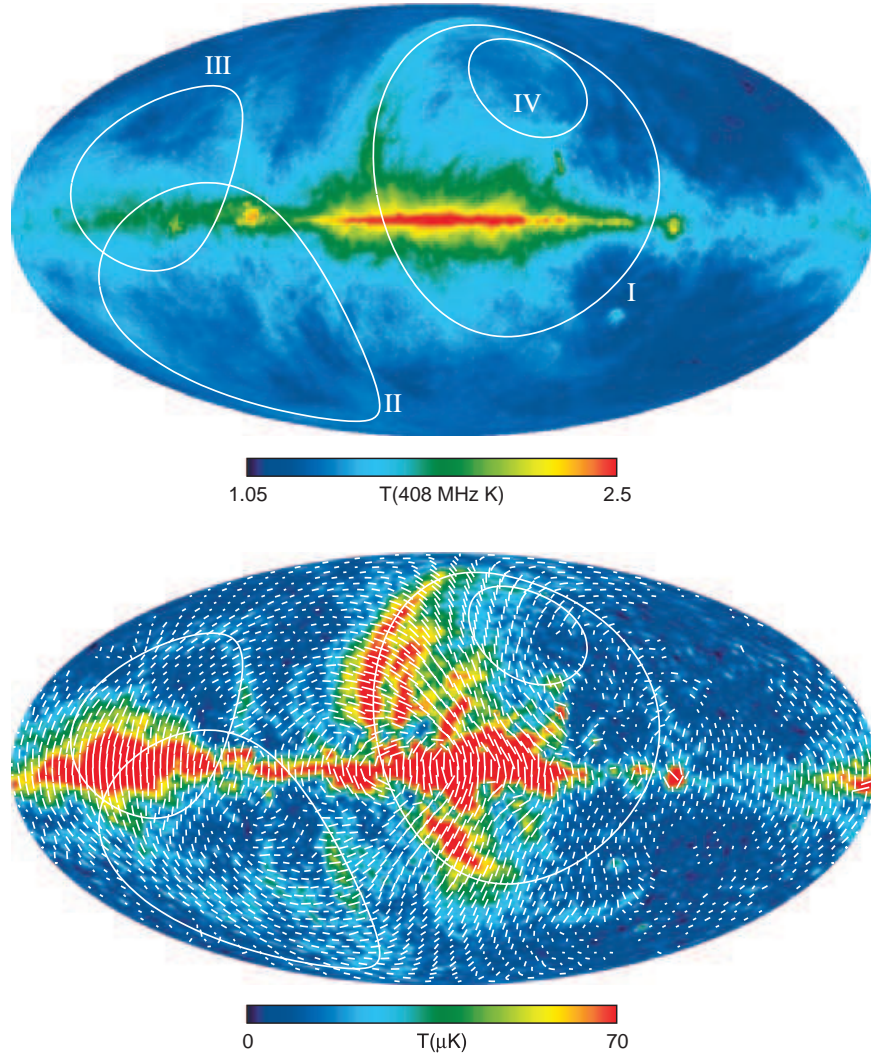


FIG. 10.— *Top*: The Haslam 408 MHz map is shown with circles indicating loops from Berkhuijsen et al. (1971). These ridges of enhanced Galactic radio emission are seen across the sky at low radio frequencies. The North Polar Spur (“Loop I”) and the Cetus arc (“Loop II”) are examples of these features, which have been described as the remnants of individual supernovae, or of correlated supernovae outbursts that produce blowouts, or as helical patterns that follow the local magnetic fields projecting out of the plane. Four such loops can be seen in the Haslam 408 MHz radio map and the WMAP map. *Bottom*: The WMAP K-band polarization map with the same loops superimposed. Note that the highly polarized southern feature is close to the North Polar Spur circle and may be related to the same physical structure. Note also that the polarization direction is perpendicular to the main ridge arc of the North Polar Spur, indicating a tangential magnetic field. This is also seen in the southern feature. Whether or not they are physically related remains unclear.

Optical Dust- K-band correlation

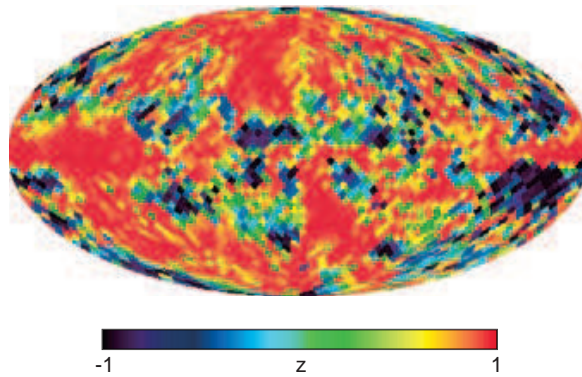


FIG. 11.— A map of the correlation, z , between the polarization angle derived from the polarization of starlight, and the polarization angle in K-band. In the regions of high K-band polarization, the correlation is strong. The polarization directions are anti-correlated in the Orion-Eridanus region near $l = -165^\circ$, suggesting spatially distinguished regions of dust and synchrotron emission.

find $P(\hat{n})$ we use the BSS magnetic field model. The fractional polarization, $\Pi_d = 0.05$, is found with a best fit of the model

to the data. The uncertainty is estimated to be 50%.

Figure 12 compares this predicted pattern of polarization to the cleaned W-band observations. We use the K-band synchrotron template to clean Q, V and W bands and then use the Q and V band maps to remove the CMB polarization signal from the W-band maps; though removing the CMB component is not necessary. The W-band map is then smoothed with a 10° beam for plotting. The appearance of the dust polarization signal pattern is similar to that found by Archeops (Ponthieu et al. 2005, Figures 2 & 3). However, the signal to noise ratio is low due to the low level of polarized dust emission at 94 GHz. The predominant feature is that the plane is dominated by positive Stokes Q emission. A visual comparison to the model is less robust. One must keep in mind that since stars are heavily obscured in the plane, the model is not expected to be accurate in the plane. Nevertheless, since Stokes Q emission corresponds to the dominant horizontal magnetic field, one does not have to sample too deeply to pick it up. Similarly, we interpret the poor correlation between the model U and the observed U as due to the insufficient sampling of other magnetic field directions by rather limited depth of the stars. Some common features between the model and W-band data are seen for $|b| > 10^\circ$. Fits of the data to the model are given in Section §4.3. Clearly, more integration time and more stellar polarization measurements are needed to fill out the model.

4.1.4. Spinning Dust Emission?

Electric dipole emission from rapidly spinning dust grains is potentially a significant source of emission at WMAP frequencies (Erickson 1957; Draine & Lazarian 1998). Thermal fluctuations in the magnetization of magnetized grains may also be a potentially significant source of emission at microwave wavelengths (Prunet & Lazarian 1999). Both have been proposed as an explanation for the correlations seen between thermal dust emission at $140 \mu\text{m}$ and microwave emission in many cosmic background experiments: COBE (Kogut et al. 1996), OVRO (Leitch et al. 1997), Saskatoon (de Oliveira-Costa et al. 1997), the 19 GHz Survey (de Oliveira-Costa et al. 1998), Tenerife (de Oliveira-Costa et al. 1999, 2004), Python V (Mukherjee et al. 2003), and COSMOSOMAS (Fernandez-Cerezo et al. 2006).

The spectral shape of spinning dust emission can be similar to synchrotron emission in the 20-40 GHz range. Thus models with either variable synchrotron spectral index (Bennett et al. 2003b) or with a spinning dust spectrum with a suitably fit cutoff frequency (Lagache 2003; Finkbeiner 2004) can give reasonable fits to the data. However, at $\nu < 20$ GHz there is a considerable body of evidence, reviewed in Bennett et al. (2003b) and Hinshaw et al. (2006), that shows (1) that the synchrotron index varies across the sky steepening with increasing galactic latitude (as is also seen in WMAP) and (2) that in other galaxies and our galaxy there is a strong correlation between 5 GHz synchrotron emission and $100 \mu\text{m}$ (3000 GHz) dust emission. The combination of these two observations imply that the $\nu < 40$ GHz WMAP foreground emission is dominated by synchrotron emission as discussed in Hinshaw et al. (2006). Nevertheless, we must consider spinning dust as a possible emission source. While on a Galactic scale it appears to be sub-dominant, it may be dominant or a significant fraction of the emission in some regions or clouds.

Spinning dust models predict an unambiguous signature in

intensity maps: at 5-15 GHz, the dust emission should be significantly less than the synchrotron emission. Finkbeiner (2004) and de Oliveira-Costa et al. (2004) argue that the Tenerife and Green Bank data show evidence for a rising spectrum between 10 and 15 GHz, suggesting the presence of spinning dust. Observations of individual compact clouds also show evidence for spinning dust emission (Finkbeiner et al. 2002, 2004; Watson et al. 2005) though the signature is not ubiquitous. The status of the observations is discussed further in Hinshaw et al. (2006).

The WMAP polarization measurements potentially give us a new way to distinguish between synchrotron and dust emission at microwave frequencies. While synchrotron emission is expected to be highly polarized, emission from spinning dust grains is thought to be weakly polarized. While promising, the signature is not unique as a tangle of magnetic field lines can also lead to a low polarization component (Sukumar & Allen 1991) as seen at 5 GHz where spinning dust emission is expected to be negligible. Using a model for the polarization fraction of the synchrotron emission based on the BSS structure, we separate the microwave intensity emission into a high and low polarization component:

$$I_{\text{high}}^\nu(\hat{n}) = P^\nu(\hat{n}) / q \Pi_{\text{sgsync}}(\hat{n})$$

$$I_{\text{low}}^\nu(\hat{n}) = I^\nu(\hat{n}) - I_{\text{high}}^\nu(\hat{n}) - I_{\text{CMB}}^{\text{LL}} - I_{\text{FF}}^{\text{MEM},\nu} \quad (16)$$

where I^ν and P^ν are the intensity and polarization maps at frequency ν . For notational convenience, we use $\nu = \text{K, Ka, Q, V, W}$. $I_{\text{CMB}}^{\text{MEM}}$ is the MEM CMB map and $I_{\text{FF}}^{\text{MEM},\nu}$ is the MEM free-free map for band ν (Bennett et al. 2003b). In effect, we use the WMAP polarization maps to extract the intensity map of the low-polarization component in the data.

Figure 13 compares the morphology of the low polarization K-band map to the W-band MEM dust map (Bennett et al. 2003a). Even in this simple model based on a number of assumptions, the agreement in morphology is striking. We quantify this by computing the rms deviation between the two scaled maps,

$$d^2 = \frac{\sum (I_{\text{W}}(\hat{n}) - \alpha I_{\text{low}}^{\text{K}}(\hat{n}))^2}{\sum I_{\text{W}}(\hat{n})^2} \quad (17)$$

where W is the W-band map, the scale factor is $\alpha = 0.105$, and the sum is taken over pixels. We find $d = 0.05$. In other words, we can “predict” the distribution of dust in W band from just the K band intensity and polarization maps. The low polarization fraction component has a spectral index of $\beta = -2.6$ between K and Q bands. This correlation between the low polarization emission regions at 22-45 GHz and the thermal emission at 90 GHz and higher may be interpreted as either a very tight correlation between tangled field files in star forming (dusty) regions or as evidence for spinning dust emission. More polarization data, $\nu < 22$ GHz observations, and extensive modeling are needed to conclusively delineate the magnitude and morphology of the various components.

4.2. Masking Polarized Foreground Emission

To compute the CMB power spectrum, we must mask the regions with the brightest foreground emission. For polarization we create a set of masks with a process that is somewhat analogous to the creation of the temperature masks (Bennett et al. 2003b). First, the K-band Q and U polarization maps are used to compute a positive-definite HEALpix $r4^{18}$ P

¹⁸ The number of pixels is $12N_{\text{side}}^2$ where $N_{\text{side}} = 2^4$ for $r4$, or resolution 4 (Górski et al. 1998). See notation in Bennett et al. (2003b).

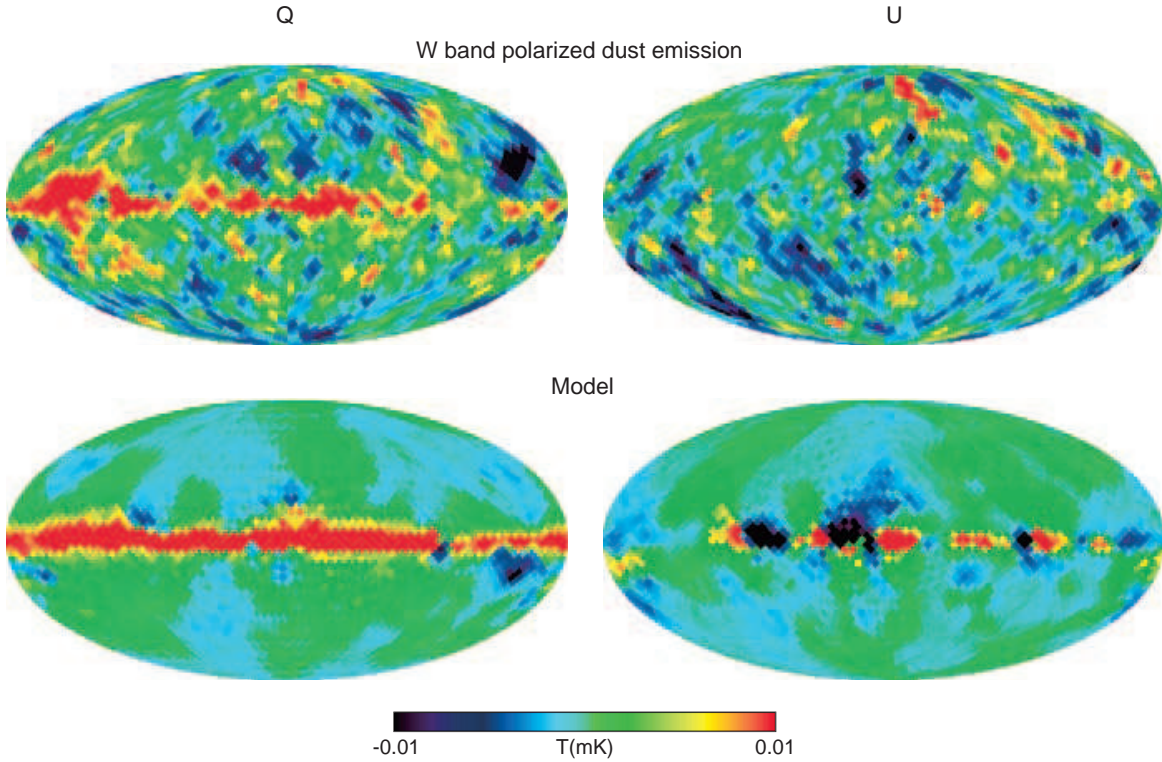


FIG. 12.— The upper panels show the polarization signal at W band with the CMB and synchrotron signal removed (smoothed with a 10° Gaussian beam). The left and right panels show Stokes Q and U polarization components respectively. There is a clear preponderance of Stokes Q emission in the plane. The lower panels show the predicted dust polarization based on Equation 15. For $|b| < 10^\circ$, the stars do not sample the dust column well and the model is not accurate, especially for Stokes U . For $|b| > 10^\circ$, there are regions where the data and model agree to the eye. However, a fit (§4.3) is used to assess the level of polarized dust emission in the maps.

map. From this a noise-bias variance map (Jarosik et al. 2006) is subtracted. The rectified noise-bias correction is small because of the coarse resolution at r4. A histogram of pixel polarization amplitudes in this noise-bias-corrected map approximates a power law. The peak is near the zero pixel value, there are just a few negative pixels (due to the noise bias correction), and there is a long positive tail.

Unlike the process in which the temperature masks were created, there is no natural cut level based on the histogram peak. Instead, the cuts are given in terms of the mean of the noise bias corrected map of P at K band. The cut level at the mean is denoted “P10”. The cut level at 0.2 times the mean is “P02”, etc. For each cut level, a preliminary mask is made by setting r4 pixels greater than the cut level to 1, and all others to 0. This mask is expanded to r9 and smoothed by a 7.5 FWHM Gaussian. This mask map is set back to all 0s and 1s using the 0.5 level as a cut-off and the sense of the mask is reversed, so that the masked-out parts of the sky have zeros (the WMAP convention). The above process results in a synchrotron polarization mask.

In the case of temperature masks, we found that additional masking based on the higher frequency bands was redundant. This is not the case with polarization. Thus we make a dust polarization mask in a similar manner. We begin with the first-year MEM dust model box-averaged to r7. Half the maximum value found in a subset of pixels in the polar caps ($|b| > 60^\circ$) is adopted as the cut-off level. A preliminary mask is made by setting r7 pixels greater than the cut-off level to unity, and all others to zero. This mask is then resolution expanded to a r9

map, smoothed by a 4.0 Gaussian, and set back to digital levels with a 0.5 cut-off. The sense of the mask is then reversed to fit the WMAP convention. Each synchrotron polarization mask is ANDed with the (constant) dust polarization mask and a constant polarized source mask.

We find, in general, that the extragalactic point sources are minimally polarized in the WMAP bands, as discussed in Hinshaw et al. (2006). We construct a source mask based on the exceptions. The most significant exception (not already covered by the synchrotron or dust polarization masks) is Centaurus A, an extended and polarized source. We found excellent agreement between WMAP and previously published maps of Cen A (Figure 2). Based on this information, we custom-masked the full extent of Cen A. Six other bright polarized sources that we masked are Fornax A, Pictor A, 3C273, 3C274, 3C279, PKS 1209-52. (Some bright polarized sources already covered by the synchrotron and dust mask regions include: 3C58, Orion A, Taurus A, IC443, 1209-52, W51, W63, HB21, CTB104A). We have determined that, for most applications, the mask that we call “P06” is the best compromise between maximizing usable sky area while minimizing foreground contamination. With the above considerations, the P06 mask masks 25.7% of the sky, mostly near the Galactic plane. We use the terminology “outside the P06 mask” to refer to data in the 74.3% of the sky left for cosmological analysis. Various masks are shown in Figure 14.

4.3. Removing the Polarized Foreground Emission from the Maps

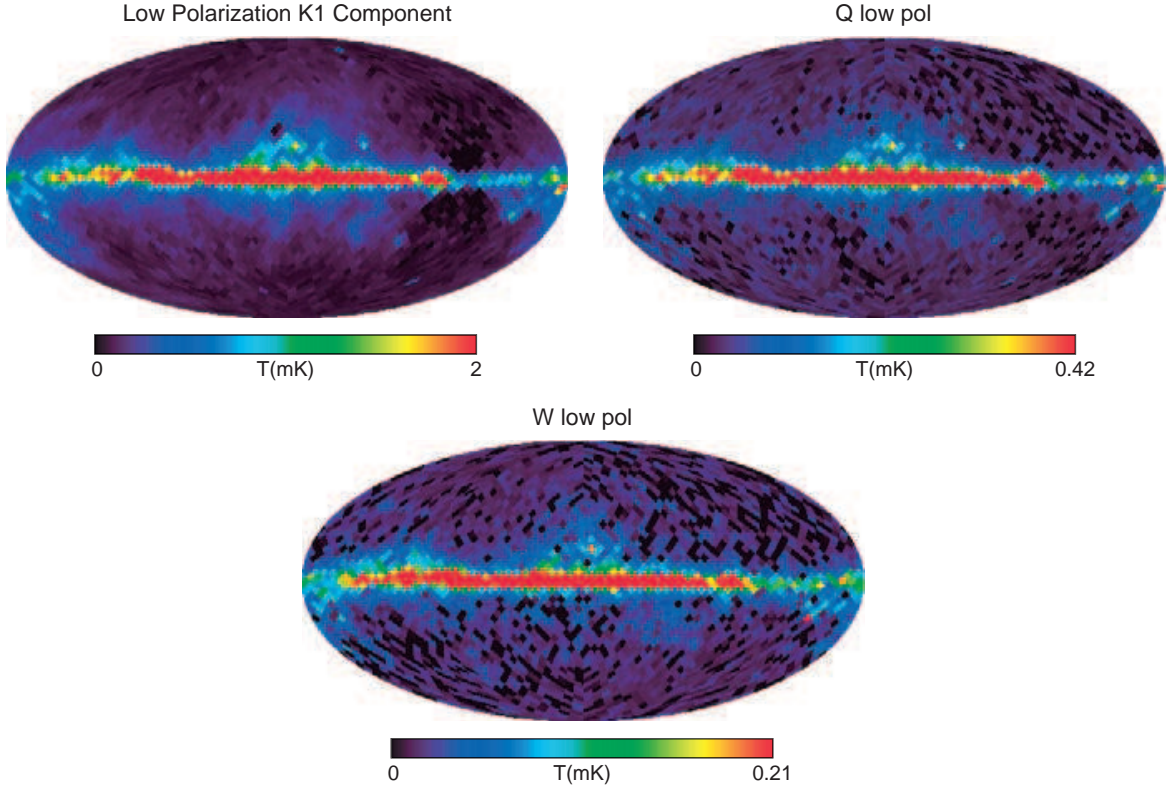


FIG. 13.— Temperature maps of the low polarization components for K, Q, and W bands. The maps are computed using equation (16). The color scale is in mK. Near the Galactic center, the low polarization component is approximately 6%, 3%, and 6% of the unpolarized emission in K, Q, and W bands respectively.

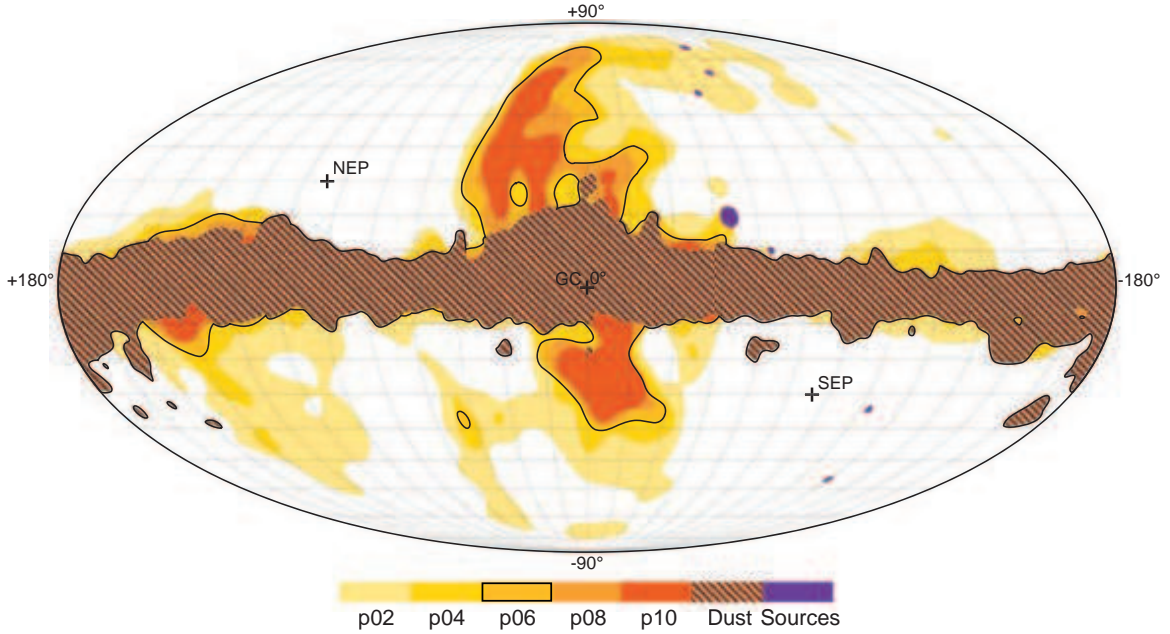


FIG. 14.— The polarization masks, in Galactic coordinates, are shown for the P02, P04, P06, and P10 cut levels. The cross hatched region along the Galactic plane, common to all polarization masks, shows the dust intensity cut. The P06 cut is outlined by the black curve. The masked sources are in violet. The North Ecliptic Pole (NEP), and South Ecliptic Pole (SEP), and Galactic Center (GC) are indicated.

Based on our analysis of the Galactic foreground emission, we have generated synchrotron and dust template maps for the purposes of foreground removal. The template maps are fit and subtracted from the Ka through W band data to generate cleaned maps that are used for CMB analysis. We assess

the efficacy of the subtraction with χ^2 and by examining the residuals as a function of frequency and multipole ℓ , as described in §5.2.

We use the K-band data to trace the synchrotron emission, taking care to account for the (relatively weak) CMB signal

in the K-band map when fitting and subtracting the template. For dust emission, we construct a model using Equation (15), where we use the FDS dust model eight (Finkbeiner et al. 1999) evaluated at 94 GHz to trace the dust intensity, I_{dust} . We call this template-based foreground model “KD3Pol”. We have tried a number of variants on the model, such as using the K-band polarization direction to trace the dust direction, $\gamma_{\text{dust}} = \gamma_K$, and we find that our cosmological conclusions are insensitive to the details of the dust template.

The synchrotron and dust templates are fit simultaneously in Stokes Q and U to three-years maps in Ka through W bands. The three-year maps are constructed by optimally combining the single-year maps for each DA in a frequency band. Specifically

$$[Q_\nu, U_\nu] = \left(\sum_i \mathbf{N}_i^{-1} \right)^{-1} \sum_i \mathbf{N}_i^{-1} [Q_i, U_i] \quad (18)$$

where i is a combined year and DA index, $[Q_i, U_i]$ is a polarization map degraded to r4 (Jarosik et al. 2006), and \mathbf{N}_i^{-1} is the inverse noise matrix for polarization map i . The fit coefficients, α_s and α_d are obtained by minimizing χ^2 , defined as

$$\chi^2 = \sum_p \frac{([Q_\nu, U_\nu] - \alpha_{s,\nu}[Q_s, U_s] - \alpha_{d,\nu}[Q_d, U_d])^2}{[\sigma_Q^2, \sigma_U^2]}, \quad (19)$$

where $[Q_s, U_s]$ is the K-band polarization map (the synchrotron template), $[Q_d, U_d]$ is the dust template, and $[\sigma_Q^2, \sigma_U^2]$ is the noise per pixel per Stokes parameter in the three-year combined maps. We have tried using optimal (\mathbf{N}^{-1}) weighting for the fits as well, and found similar results for the coefficients. The results reported here are based on the simpler diagonal weighting. The fit is evaluated for all pixels outside the processing mask (Jarosik et al. 2006).

The fit coefficients are given in the top half of Table 3. For each emission component we also report the effective spectral index derived from the fit: $\beta_s(\nu_K, \nu)$ for synchrotron emission, and $\beta_d(\nu, \nu_W)$ for dust. These results indicate that the spectrum of the component traced by K-band is systematically flattening with increasing frequency, which is unexpected for synchrotron emission. This behavior is statistically significant, and is robust to variations in the dust model and the data weighting. We do not have a definitive explanation for this behavior though note that it is expected for correlated synchrotron and dust emission.

To guard against the possibility of subtracting CMB signal, we modified the template model as follows. We take the 4 synchrotron coefficients in Table 3 and fit them to a spectrum model of the form

$$\alpha_s(\nu) = \alpha_{s,0} \cdot g(\nu)(\nu/\nu_K)^{\beta_s} + \alpha_c, \quad (20)$$

where $\alpha_{s,0}$, β_s , and α_c are model parameters that are fit to the $\alpha_s(\nu)$, and $g(\nu)$ is the conversion from antenna temperature to thermodynamic temperature at frequency ν . This results in a modified set of synchrotron coefficients that are forced to follow a power-law that is largely determined by the Ka and Q-band results. Specifically, the modified coefficients are given in Table 3. The implied synchrotron spectrum is $\beta_s = -3.33$. This results in a 12% reduction in the synchrotron coefficients at Q-band, and a 33% reduction at V-band. However, because the K-band template is dominated by an $\ell = 2$ E-mode signal (see §5.1), this change has a negligible effect on our cosmological conclusions, which are dominated by E-mode signal at $\ell > 2$. A comparison of selected “before and after” cleaning maps is shown in Figure 15.

TABLE 3
FIT COEFFICIENTS TO FOREGROUND TEMPLATES

Band	$\alpha_{s,\nu}$	$\beta_s(\nu_K, \nu)$	$\alpha_{d,\nu}$	$\beta_d(\nu, \nu_W)$
Ka	0.310	−3.22	0.0015	1.54
Q	0.169	−3.12	0.0015	1.89
V	0.061	−2.94	0.0034	1.92
W	0.036	−2.51	0.0089	...
Ka	0.297	−3.33	0.0015	1.54
Q	0.149	−3.33	0.0015	1.89
V	0.041	−3.33	0.0034	1.92
W	0.011	−3.33	0.0089	...

The top of the Table gives the coefficients for a direct fit to the polarization maps. The α are dimensionless and produce model maps in thermodynamic units. The spectral indices β refer to antenna temperature. The bottom half of the Table gives the same numbers for when the synchrotron fit is constrained to follow a power law. The fits were evaluated outside the processing mask.

We also account for the cleaning in the map error bars. Since the K-band data are a combination of synchrotron and CMB emission, subtracting a scaled version of K band from a higher frequency channel also subtracts some CMB signal. If the fit coefficient to the higher frequency channel is a_0 , then the cleaned map is $M'(\nu) = (M(\nu) - a_0 M(\nu = K)) / (1 - a_0)$, where M is the map and ν denotes the frequency band. The factor of $1/(1 - a_0)$ dilates the noise in the new cleaned map. The maps we use for cosmological analysis were cleaned using the coefficients in the bottom half of Table 3, including the above correction to account for loss of CMB signal.

One measure of the efficacy of the foreground removal is the change in χ^2 , relative to a null signal, between pre-cleaned and cleaned maps. Table 4 gives the values for the full sky and the P06 cut. In both cases the full pixel covariance matrix was used to compute χ^2 for Stokes Q and U simultaneously. For the full sky the number of degrees of freedom, ν , is 6144 (twice the number of pixels in an r4 map) and outside the P06 mask $\nu = 4534$. Note the large $\Delta\chi^2$ achieved with just a two parameter fit. By comparing the full sky to the P06 χ^2 , we find that the starlight-based dust template is insufficient in the plane as discussed in §4.1.3. We also see that outside the P06 mask, that Q and V bands are the cleanest maps and that they are cleaned to similar levels. Since χ^2/ν for Q and V bands is so close to unity for the cleaned maps, it is no longer an effective measure of cleaning. Instead, we examine the power spectra ℓ by ℓ to assess the cleaning, and then test the sensitivity of the cosmological conclusions to cleaning by including Ka and W band data.

5. POWER SPECTRA

The Q & U maps are well suited to analyzing foreground emission, are useful for comparing to other polarization maps, and have straightforward noise properties. However, they are not well suited to quantifying the CMB polarization anisotropy because their definition is coordinate dependent. The Q and U maps may be transformed into scalar and pseudo-scalar quantities called E and B modes (Seljak 1997; Kamionkowski et al. 1997; Zaldarriaga & Seljak 1997). E and B are so named because they comprise a curl-free and divergence-free decomposition of the spin-2 polarization field, analogous to static electric and magnetic fields. The problem of separating E and B modes with an unevenly sam-

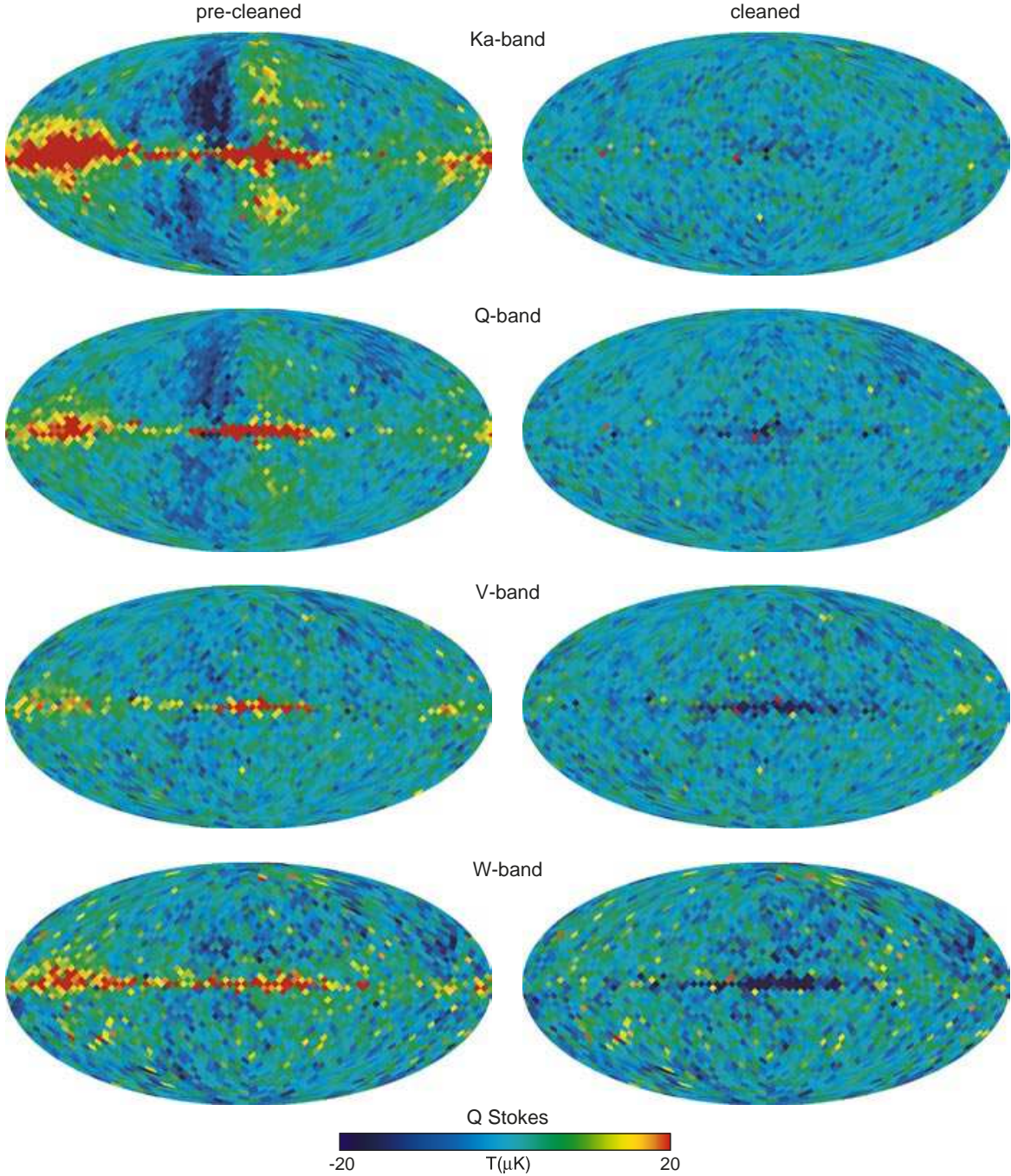


FIG. 15.— The Ka, Q, V, and W band Q Stokes Parameter maps before and after foreground subtraction using the method outlined in §4.3. There is a possible residual signal in W band though the noise is not yet sufficiently low to be certain. The U maps look similar. The cleaning for the cosmological analysis was done outside the processing cut (Jarosik et al. 2006) and was based on the K-band maps and the starlight-based dust template. The over-subtracted dark regions on the galactic plane are inside the processing cut.

pled and cut sky has been considered by a number of authors (e.g., Tegmark et al. 2000; Lewis et al. 2002; Bunn et al. 2003). In our analysis, we work directly with Q and U maps to produce the E and B angular power spectra. The conventions follow Appendix A of Kogut et al. (2003).¹⁹

Fundamental symmetries in the production and growth of the polarized signal select the possible configurations for the

¹⁹ In this paper we do not use the rotationally invariant Q' and U' of Kogut et al. (2003).

CMB polarization. Scalar (density) perturbations to the matter power spectrum give rise to T and E modes. Tensor perturbations (gravitational waves) give rise to T, E, and B modes primarily at $\ell \lesssim 200$ ²⁰. Both scalar and tensor perturbations can produce polarization patterns in both the decoupling and reionization epochs. Vector perturbations²¹ (both inside and outside the horizon) are redshifted away with the expansion of

²⁰ At $\ell \gtrsim 70$ primordial B modes are dominated by the gravitational lensing of E modes.

²¹ Vector modes are produced by purely rotational fluid flow. Based on

TABLE 4
COMPARISON OF χ^2 BETWEEN PRE-CLEANED AND CLEANED MAPS

Band	χ^2/ν Pre-cleaned	χ^2/ν Cleaned	ν	$\Delta\chi^2$
Ka	10.65	1.20	6144	58061
Q	3.91	1.09	6144	17326
V	1.36	1.19	6144	1045
W	1.38	1.58	6144	-1229
Ka	2.142	1.096	4534	4743
Q	1.289	1.018	4534	1229
V	1.048	1.016	4534	145
W	1.061	1.050	4534	50

The top half of the table compares χ^2/ν for the full-sky pre-cleaned map to χ^2/ν for full-sky cleaned map. The bottom half makes a similar comparison for the region outside the P06 mask.

the universe, unless there are active sources creating the vector modes, such as topological defects. We do not consider these modes here.

At the noise levels achievable with *WMAP*, the standard cosmological model predicts that only the E mode of the CMB polarization and its correlation with T will be detected. The B-mode polarization signal is expected to be too weak for *WMAP* to detect, while the correlations of T and E with B is zero by parity. Thus the TB and EB signals serve as a useful null check for systematic effects. The polarization of foreground emission is produced by different mechanisms. Foreground emission can have any mixture of E and B modes, it can be circularly polarized (unlike the CMB), and E and B can be correlated with T.

We quantify the CMB polarization anisotropy with the C_ℓ^{TE} , C_ℓ^{EE} , and C_ℓ^{BB} angular power spectra, where

$$C_\ell^{XY} = \langle a_{\ell m}^X a_{\ell m}^{Y*} \rangle. \quad (21)$$

Here the $\langle \rangle$ denote an ensemble average, $a_{\ell m}^T$ are the multipoles of the temperature map, and $a_{\ell m}^E, a_{\ell m}^B$ are related to the spin-2 decomposition of the polarization maps

$$[Q \pm iU](\hat{x}) = \sum_{\ell > 0} \sum_{m=-\ell}^{\ell} \mp 2 a_{\ell m} \mp 2 Y_{\ell m}(\hat{x}) \quad (22)$$

via

$$\pm 2 a_{\ell m} = a_{\ell m}^E \pm i a_{\ell m}^B \quad (23)$$

(Zaldarriaga & Seljak 1997). The remaining polarization spectrum combinations (TB, EB) have no expected cosmological signal because of the statistical isotropy of the universe.

We compute the angular power spectrum after applying the P06 polarization mask using two methods depending on the ℓ range. All power spectra are initially based on the single-year r9 Q and U maps (Jarosik et al. 2006). For $\ell > 23$ ²², we compute the power spectrum following the method outlined in Hivon et al. (2002), and Kogut et al. (2003, Appendix A) as updated in Hinshaw et al. (2006) and Appendix B.2. The statistical weight per pixel is N_{obs}/σ_0^2 where σ_0 is the noise per

the fit of the adiabatic Λ CDM model to *WMAP* TT data, the contribution of such modes is not large (Spergel et al. 2003). However, a formal search for them has not been done.

²² $\ell = 23 = 3N_{side} - 1$ is the Nyquist limit on ℓ . For some analysis methods (§D) we use HEALPix r3 for which $n_{side} = 2^3 = 8$

observation (Jarosik et al. 2006; Hinshaw et al. 2006). Here N_{obs} is a 2x2 weight matrix that multiplies the vector $[Q, U]$ in each pixel

$$N_{obs} = \begin{pmatrix} N_Q & N_{QU} \\ N_{QU} & N_U \end{pmatrix}, \quad (24)$$

where N_Q, N_U , and N_{QU} are the elements of the weight arrays provided with the sky map data. Note that the correlation between Q and U within each pixel is accounted for. We refer to this as “ N_{obs} weighting.” From these maps, only cross power spectra between DAs and years are used. The cross spectra have the advantage that only signals common to two independent maps contribute and there are no noise biases to subtract as there are for the auto power spectra. The covariance matrices for the various C_ℓ are given in Appendix C.3.

For $\ell < 23$ we mask and degrade the r9 maps to r4 (see the last paragraph of Appendix D and Jarosik et al. 2006) so that we may use the full r4 inverse pixel noise matrix, \mathbf{N}^{-1} , to optimally weight the maps prior to evaluating the pseudo- C_ℓ . This is necessary because the maps have correlated noise that is significant compared to the faint CMB signal. By “ \mathbf{N}^{-1} weighting” the maps, we efficiently suppress modes in the sky that are poorly measured given the *WMAP* beam separation and scan strategy (mostly modes with structure in the ecliptic plane). We propagate the full noise errors through to the Fisher matrix of the power spectrum. For the spectrum plots in this section, the errors are based on the diagonal elements of the covariance matrix which is evaluated in Appendix B.

Figure 16 shows the effect that correlated noise has on the low ℓ errors in the EE and BB spectra. The curves show the diagonal elements of the inverse Fisher matrix (the C_ℓ errors) computed in two ways: (1) assuming the noise is uncorrelated in pixel space and described by N_{obs} (red) and (2) assuming it is correlated and correctly described by \mathbf{N}^{-1} (black). The smooth rise in both curves toward low ℓ is due to the effects of $1/f$ noise and is most pronounced in the W4 DA, which has the highest $1/f$ noise. The structure in the black trace is primarily due to the scan strategy. Note in particular, that we expect relatively larger error bars on $\ell = 2, 5, 7$ in EE and on $\ell = 3$ in BB. *We caution those analyzing maps that to obtain accurate results, the \mathbf{N}^{-1} weighting must be used when working with the $\ell < 23$ power spectra.* For the Monte Carlo Markov Chains (MCMC) and cosmological parameter evaluation, we do not use the power spectrum but find the exact likelihood of the temperature and polarization maps given the cosmological parameters (Appendix D & Hinshaw et al. 2006).

For both r4 and r9 maps there are 15 MASTER cross power spectra (see Table 5). For the full three-year result, we form $\sum_{i,j=1}^3 y_i \times y_j / 6$ omitting the $y_1 \times y_1$, $y_2 \times y_2$, and $y_3 \times y_3$ auto power spectra. The noise per ℓ in the limit of no celestial signal, N_ℓ , is determined from analytical models that are informed by full simulations for r9 (including $1/f$ noise), and from the full map solution for r4.

5.1. Power Spectrum of Foreground Emission Outside the P06 Mask.

Figure 17 shows the EE and BB power spectra for the region outside the P06 mask, 74.3% of the sky, before any cleaning. The 15 cross spectra have been frequency averaged into four groups (Table 5) by weighting with the diagonal elements of the covariance matrix. Data are similarly binned over the indicated ranges of ℓ . It is clear that even on the cut sky the foreground emission is non negligible. In K band, we find $\ell(\ell+1)C_{\ell < 2-6}^{EE} / 2\pi = 66 (\mu K)^2$ and

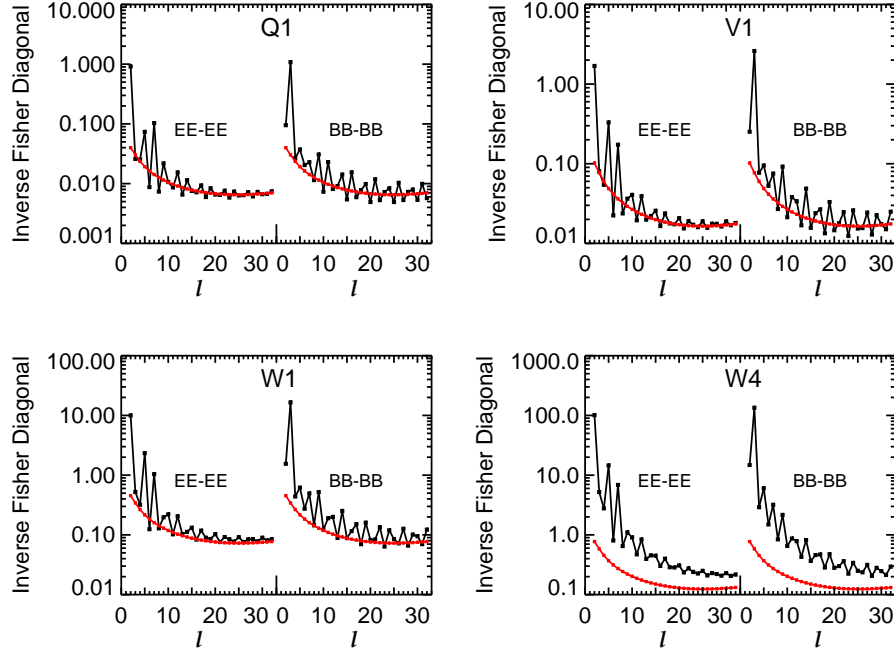


FIG. 16.— A comparison of the predicted C_ℓ errors with (black) and without (red) assuming correlated noise in the polarization sky maps. On the y-axis is plotted the diagonal element of the inverse of the Fisher matrix for one year of data. The units are $(\mu\text{K})^4$. Note that the y-axis scale for each plot is different. In each panel EE and BB are shown. The variations in the \mathbf{N}^{-1} weighting are due to the scan pattern combined with the sky cut. There is less variation for B-modes than there is for E-modes. W4 has the largest $1/f$ noise of all radiometers. One can see that the combination of $1/f$ noise coupled with WMAP’s scan strategy leads to a larger uncertainty than one would get from considering just the effects of $1/f$ noise alone.

$\ell(\ell+1)C_{\ell=2-6}^{BB}/2\pi = 48 (\mu\text{K})^2$, where $\ell = \langle 2-6 \rangle$ denotes the weighted average over multipoles two through six. The emission drops by roughly a factor of 200 in C_ℓ by 61 GHz resulting in $\lesssim 0.3 (\mu\text{K})^2$ for both EE and BB. There is a “window” between $\ell = 4$ and $\ell = 8$ in the EE where the emission is comparable to, though larger than, the detector noise. Unfortunately, BB foreground emission dominates a fiducial $r=0.3$, $\tau=0.09$ model by roughly an order of magnitude at $\ell < 30$. In general, the power spectrum of the foreground emission scales approximately as $\ell^{-1/2}$ in $\ell(\ell+1)C_\ell$.

Figure 18 shows the power spectra as a function of frequency for a few ℓ bands. The spectrum of the emission follows that of synchrotron with $T \propto \nu^{\beta_s}$ with $\beta_s = -2.9$ for both EE and BB. There is some evidence for another component at $\nu > 60$ as seen in the flattening of the EE $\ell = 2$ term. We interpret this as due to dust emission. In the foreground model, we explicitly fit to a dust template and detect polarized dust emission. However, there is not yet a sufficiently high signal to noise ratio to strongly constrain the dust index or amplitude outside the P06 mask.

A simple parameterization of the foreground emission outside the P06 mask region is given by

$$\ell(\ell+1)C_\ell^{fore}/2\pi = (\mathcal{B}_s(\nu/65)^{2\beta_s} + \mathcal{B}_d(\nu/65)^{2\beta_d})\ell^m. \quad (25)$$

We have introduced the notation $\mathcal{B}^{xx} \equiv \ell(\ell+1)C_\ell^{xx}/2\pi$ to simplify the expression. The “d” and “s” subscripts stand for “dust” and “synchrotron.” From an unweighted fit to all the raw $\ell < 100$ data with the dust index fixed at $\beta_d = 1.5$, we find for EE $\mathcal{B}_s = 0.36 (\mu\text{K})^2$, $\beta_s = -3.0$, $\mathcal{B}_d = 1.0 (\mu\text{K})^2$ and $m = -0.6$; and for BB $\mathcal{B}_s = 0.30 (\mu\text{K})^2$, $\beta_s = -2.8$, $\mathcal{B}_d = 0.50 (\mu\text{K})^2$ and $m = -0.6$. This model is given as an approximate guide. Its ℓ dependence is shown in Figure 17 for $\nu = 65$ GHz and

its frequency dependence is shown in Figure 18 for BB $\ell = 2$. One can see that this scaling model picks up the general trends but not the details of the foreground emission. For example, it ignores correlations between dust and synchrotron emission. It predicts an average foreground emission of $\approx 1 (\mu\text{K})^2$ at 30 GHz and $\ell = 300$. Leitch et al. (2005) give an upper bound of $\approx 1 (\mu\text{K})^2$ for synchrotron emission in this range. As DASI observes a relatively synchrotron-free region and at ℓ s beyond where this simple parametrization can be tested, there is not a conflict with their results. The same is true for the CBI experiment (Readhead et al. 2004) which also observed at 30 GHz but at a predominantly higher ℓ and in a predetermined clean region of sky.

For a more complete model of the power spectra of foreground emission, one must take into account the correlations or anticorrelations between various foreground components and between the foreground components and the CMB. For example, a reasonable fit to the $\ell = 2$ EE spectrum, which is dominated by foreground emission, is given by

$$\mathcal{B}^{EE}(\nu) = a_s(\nu_1\nu_2)^{\beta_s} + \rho_{sd}a_s a_d(\nu_1^{\beta_s}\nu_2^{\beta_d} + \nu_1^{\beta_d}\nu_2^{\beta_s}) + a_d(\nu_1\nu_2)^{\beta_d} \quad (26)$$

where ρ_{sd} is the dust synchrotron correlation coefficient, ν_1 and ν_2 are the frequencies of the two spectra that are correlated, the β_d and β_s are the dust and synchrotron spectral indices, and $\nu = \sqrt{\nu_1\nu_2}$. This fit is shown in Figure 18. After normalizing the frequency to 65 GHz, the following coefficients were found to reasonably represent the data: $a_s = 0.64$, $\beta_s = -2.9$, $a_d = 0.65$, $\beta_d = 1.5$, and $\rho_{sd} = 0.46$. In order to produce the KV, KW, and KaW features, there must be significant correlations between dust and synchrotron emission. For the $\ell = 4$ EE spectrum a similar expression fits the data if ρ_{sd} is negative.

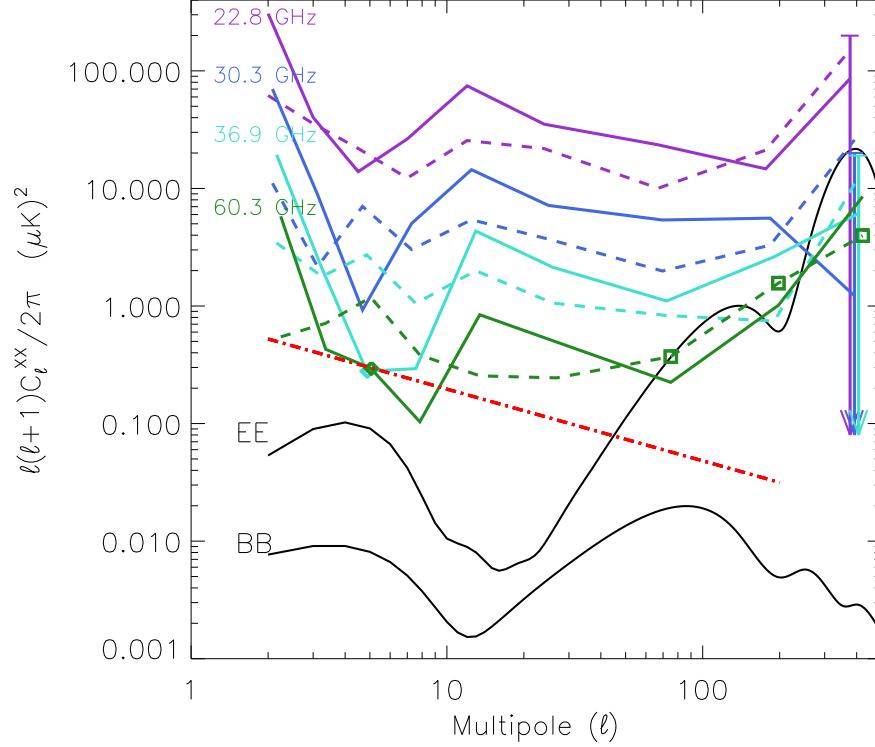


FIG. 17.— The absolute value of the EE (solid, violet through green) and BB (dashed, violet through green) polarization spectra for the region outside the P06 mask. The best fit Λ CDM model to TT, TE, and EE data with $\tau = 0.09$ and an additional tensor contribution with $r = 0.3$ is shown in black. The cross spectra have been combined into frequency bins according to Table 5 and into the following ℓ bins: [2, 3, 4-5, 6-8, 9-15, 16-32, 33-101, 102-251, 252-502]. In the presence of a dominant synchrotron spectrum, the averages over frequency are dominated by contributions from the lowest frequencies as can be seen by comparing the above at $\ell = 2$ to Figure 18. Diamonds (EE) and boxes (BB) denote the data points that are negative. The points are plotted at their absolute value to limit clutter. They should be interpreted as indicating the approximate noise level of the measurement. The 1σ upper bounds and downward arrows mark points that are positive but consistent with zero. The general rise in the data for $\ell > 100$ is due to the large noise term. The red line corresponds to Equation 25 evaluated for $\nu = 60$ GHz for the BB foreground emission.

Some care is needed in interpreting the statistical significance of power spectra that include foreground emission and a cut sky. The lack of statistical isotropy of the foreground emission means that it must be treated separately from the CMB when assessing the net noise. In the presence of foregrounds, the random uncertainty becomes

$$\Delta C_\ell^2 = \frac{2}{(2\ell+1)f_{\text{sky}}^2} [N_\ell^2 + 2N_\ell \mathcal{F}_\ell] \quad (27)$$

where \mathcal{F}_ℓ is the foreground emission at each ℓ . We plot only the first term in Figures 17 & 18 to indicate the size of the statistical error. Additionally, with the sky cut there is a noise-foreground coupling between $N_\ell^{E,B}$ and $\mathcal{F}_{\ell\pm 2}^{E,B}$, and between $N_\ell^{E,B}$ and $\mathcal{F}_{\ell\pm 1}^{B,E}$. This is analogous to the noise coupling shown in Appendix C.

5.2. Power Spectrum of Foreground-Cleaned Maps Outside the P06 Mask

We next discuss the power spectrum after removing the foreground emission from the *maps*. Cleaning foregrounds not only changes the mean of C_ℓ , but it reduces ΔC_ℓ because of the couplings. The choice of model makes little difference to the conclusions. For all the following we have subtracted the best fit KD3Pol Q and U templates from the Ka through W maps (both r4 and r9 versions) as described in Section 4. Table 5 shows the EE $\ell = 2$ and BB $\ell = 5$, the multipoles with the largest foreground contributions, for both before and after the subtraction. Where the foreground signal is dominant, the

subtraction can reduce its level by a factor of 6-10 in temperature.

When we fit and subtract the foreground templates, we use essentially all of the available data on polarized foreground emission. The error bar on the power spectrum of the cleaned maps is dilated in the cleaning process as discussed above. We do not include an addition error for systematic uncertainty in the model. Rather, by comparing spectra of pre-cleaned to cleaned maps, we estimate that the model removes at least 85% of the synchrotron. This is demonstrated, for example, in the KKa and KaKa combinations for $\ell = 2$ EE in Table 5, in the subtraction shown in Figure 15, and to a lesser degree by the null EB and BB power spectra. We also note that to a good approximation foreground emission adds only in quadrature to CMB emission.

Figure 19 shows the power spectra of the foreground cleaned maps as a function of frequency for $\ell = 2-9$. It also shows what we estimate to be the maximum levels of residual foreground contamination in the power spectrum. In the figure, we plot the synchrotron spectrum scaled to 0.15 of the pre-cleaned Ka band value (in temperature). This shows that there is negligible residual synchrotron from 40 to 60 GHz with the possible exception of $\ell = 2$ at 40 GHz. Given the size of the $\ell = 2$ error bar, this potential contribution to the determination of the optical depth is negligible as discussed in Section §6.1. Constraining the residual dust contamination is more difficult. In Figure 19, we also show the MEM temperature dust model scaled by 5%, a typical dust polarization value. A similarly scaled FDS model is almost identical. This

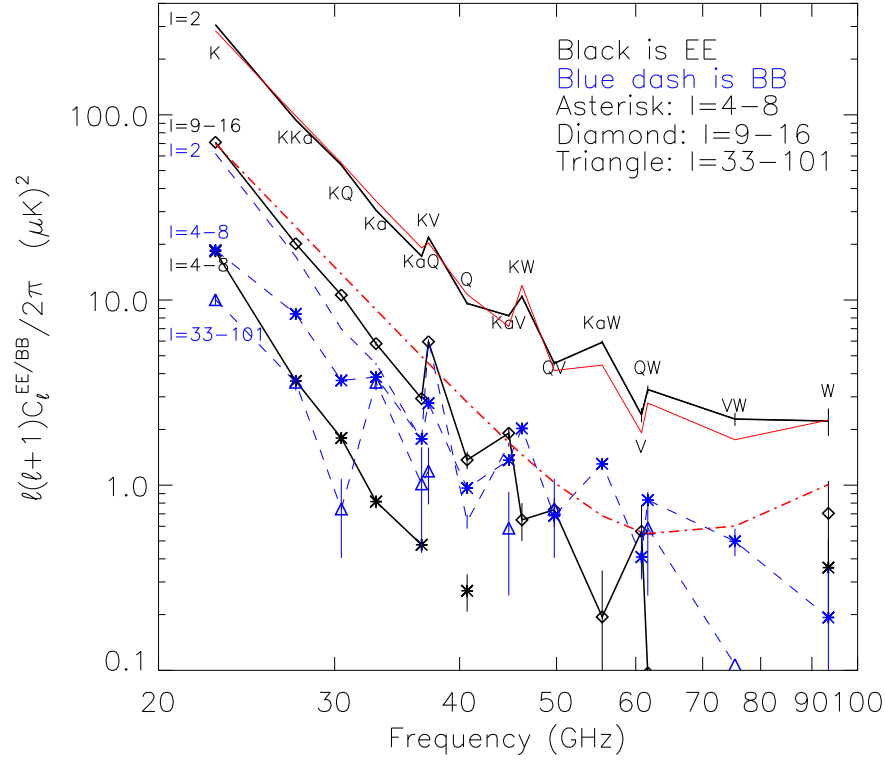


FIG. 18.— The frequency spectrum of the EE and BB power spectra for the region outside the P06 mask. To increase the signal to noise ratio, multiple values of ℓ are averaged as indicated. Only statistical errors are shown. Negative values are not plotted. The frequency band combinations are given in Table 5. The thin red line running close to the $\ell = 2$ EE spectrum is the model in Equation 26. The dot-dash red line corresponds to Equation 25 evaluated for BB at $\ell = 2$.

TABLE 5
WMAP EE $_{\ell=2}$ AND BB $_{\ell=5}$ VALUES FOR $\ell(\ell+1)C_\ell/2\pi$

Cross	Bin	f_{eff}	EE $_{\ell=2}$	y1-y2 EE $_{\ell=2}$	BB $_{\ell=5}$	y1-y2 BB $_{\ell=5}$	EE $_{\ell=2}^{Cleaned}$	BB $_{\ell=5}^{Cleaned}$
		GHz	(μK) 2	(μK) 2	(μK) 2	(μK) 2	(μK) 2	(μK) 2
KK	1	22.8	306.6 ± 0.12	...	38.1 ± 0.18
KKa	2	27.4	93.3 ± 0.07	0.0 ± 0.22	14.9 ± 0.10	0.6 ± 0.30	0.8 ± 0.10	0.6 ± 0.14
KQ	2	30.5	53.6 ± 0.09	-1.6 ± 0.27	8.5 ± 0.11	-1.3 ± 0.32	3.0 ± 0.10	0.2 ± 0.11
KV	3	37.2	21.8 ± 0.10	-0.7 ± 0.29	2.0 ± 0.13	-0.6 ± 0.38	1.6 ± 0.10	-0.7 ± 0.13
KW	4	46.2	10.4 ± 0.13	-3.8 ± 0.4	0.1 ± 0.17	-0.3 ± 0.52	-7.4 ± 0.14	-1.9 ± 0.18
KaKa	2	33.0	30.5 ± 0.13	...	4.8 ± 0.17	...	0.7 ± 0.26	-0.1 ± 0.35
KaQ	3	36.6	17.2 ± 0.09	-0.0 ± 0.27	2.7 ± 0.11	-0.7 ± 0.32	0.6 ± 0.15	-0.1 ± 0.18
KaV	4	44.8	8.2 ± 0.10	0.2 ± 0.30	0.7 ± 0.12	0.2 ± 0.37	0.1 ± 0.15	-0.2 ± 0.19
KaW	4	55.5	5.9 ± 0.14	0.6 ± 0.41	0.6 ± 0.17	0.0 ± 0.51	0.4 ± 0.20	-0.1 ± 0.25
QQ	4	40.7	9.6 ± 0.17	-0.1 ± 0.67	1.8 ± 0.17	0.3 ± 0.68	0.3 ± 0.23	0.0 ± 0.24
QV	4	49.7	4.5 ± 0.12	-0.1 ± 0.37	0.6 ± 0.13	0.9 ± 0.40	-0.1 ± 0.15	0.0 ± 0.16
QW	4	61.7	3.3 ± 0.17	0.2 ± 0.5	0.7 ± 0.18	-0.1 ± 0.55	0.1 ± 0.20	0.2 ± 0.21
VV	4	60.8	2.4 ± 0.21	-0.5 ± 0.81	0.2 ± 0.21	-0.2 ± 0.65	0.5 ± 0.19	0.2 ± 0.23
VW	4	75.4	2.3 ± 0.18	1.0 ± 0.55	0.2 ± 0.21	-0.2 ± 0.65	0.5 ± 0.19	0.2 ± 0.23
WW	4	93.5	2.2 ± 0.37	1.5 ± 1.27	-0.4 ± 0.44	-0.3 ± 1.48	0.3 ± 0.38	-0.7 ± 0.45

For $\nu > 40$ GHz, the largest foreground signals are at $\ell = 2$ of EE and $\ell = 5$ of BB. This table shows the “raw” and “cleaned” values. The column labeled “bin” indicates which cross spectra are coadded into frequency bins. Because K band is used as a foreground template, there are no foreground corrected values. Also, as there are only single K and Ka band polarization channels, it is not possible to form cross spectra of y1-y2. KW is not used in any of the averages over frequency.

shows that even if we did not model and subtract dust, the contamination from it would not be large in Q and V bands. A more detailed model might have to take into account the possibility that the electrons and dust grains are in regions at different line of sight distances with different magnetic fields or that variations in the magnetic field could alias power from

low multipoles to higher ones.

The cross power spectra of the cleaned maps are combined by frequency band for testing cosmological models. The 10 cross spectra (since K-band is used in the model, there is no K-band cleaned spectrum) are assessed ℓ by ℓ with a least squares fit to a flat line in Figure 19. The results are shown for

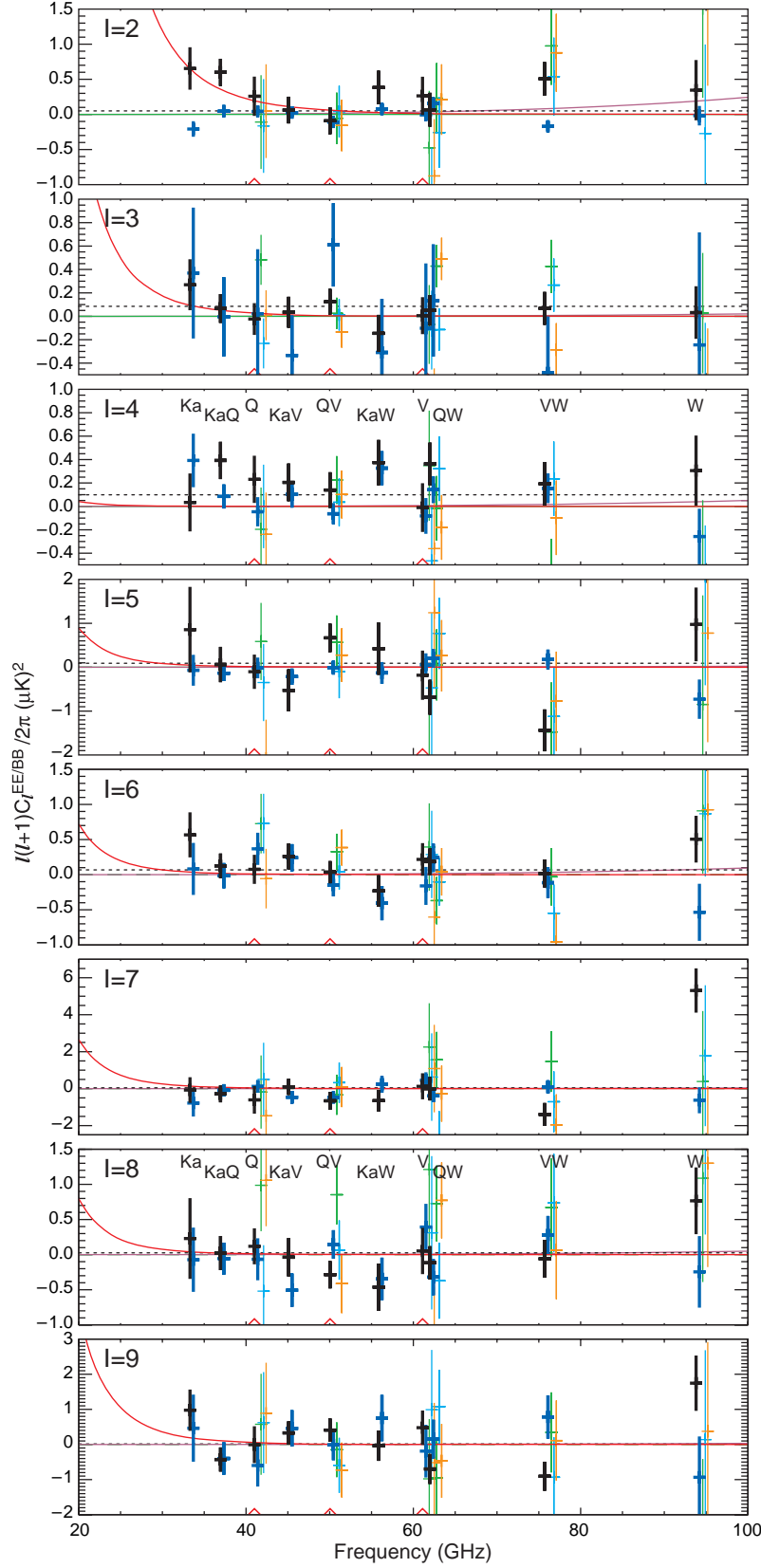


FIG. 19.— The frequency spectrum of the foreground cleaned EE and BB power spectra outside the P06 mask for $\ell = 2-9$. Black shows EE, blue shows BB, and green, cyan, and orange show the EE $y_i - y_j$ spectra (the BB ones are similar). For cosmological analysis, only the QQ, QV, and VV frequency channels are used (indicated by red triangles on the bottom of each panel). The dotted black line shows the EE signal for $\tau = 0.09$. The brown line shows the MEM dust temperature spectrum scaled by 0.0025 to indicate the level of 5% polarization. Averaged over the region outside the P06 mask, this is most likely an overestimate. The red curve shows the synchrotron spectrum scaled to 0.15 the pre-cleaned K-band temperature value. Based on the foreground model and discussion in text, it is unlikely that there is a significant residual foreground contamination in Q and V bands. Note that for all frequency combinations above 40 GHz (excluding KW), BB is clearly consistent with zero, also indicating the efficacy of the foreground cleaning.

the QQ+QV+VV (denoted “QV combination”) and QV+KaV combinations in EE, we find $0.1 < \text{PTE} < 1$ for all $\ell < 16$, where PTE is for “Probability to Exceed” and is the probability that a random variable drawn from the same distribution exceeds the measured value of χ^2 . When W band is added to the mix, we find $\text{PTE} < 0.03$ for $\ell = 5, 7, 9$, though all other values of ℓ give reasonable values. For BB, all frequency combinations yield reasonable PTEs for all ℓ . Thus, there is a residual signal in our power spectra that we do not yet understand. It is evident in W band in EE at $\ell = 7$ and to a lesser degree at $\ell = 5$ and $\ell = 9$. We see no clear evidence of it anywhere else.

5.3. Null Tests and Systematic Checks Outside the P06 Mask

Null tests are critical for assessing the quality of the data. We have examined the data in a wide variety of ways based on differencing assembly, frequency band, ℓ range, and year. We present selected, though typical, results in the following. A particularly important test is the null measurement of the BB, TB, and EB signals as shown in Table 6 and Figure 20. These data combinations are derived from the same processing as the EE, TE, and TT combinations, where a signal is detected. Thus, the null result highlights the stability of the WMAP data, the mapmaking, the foreground cleaning, and the power spectrum estimation.

The power spectrum of the difference of the individual yearly maps is another significant test. Table 7 shows the results for all the yearly differences for $\ell = 2 - 16$, the critical region of ℓ -space for the cosmological analysis. We have also used the $(y1 \times y1 + y2 \times y2 - y1 \times y2 - y2 \times y1)/4$ cross spectra to similar effect. This combination is equivalent to forming the power spectrum of the difference between $y1$ and $y2$ maps. In principle it does not contain any signal. The cross-spectrum method treats the noise in a slightly different way from the straight map method, where one must use the error bars from one of the maps. It has been checked with simulations. Similar combinations are used for the other years.

Using a variant of cross-spectrum method, we have also tested combinations of DAs for multiple ranges in ℓ within each frequency band. For all null tests, we find the expected null measurements, apart from the previously mentioned residuals at $\ell = 5$ & 7 in W band. Table 6 gives the reduced χ^2 for all combinations of T, E, and B data for a number of data combinations.

From Figure 19, it is clear that the large signal in W band is not residual dust contamination because the dust would not fit measurements in VW. Additionally, if one assumes that the polarized emission at a particular ℓ is a fraction times the intensity at the same ℓ , it would require $> 40\%$ dust polarization, which is unreasonable. Though this simple picture does not take into account the aliasing of intensity from a lower ℓ , we do not observe a similar effect with the synchrotron emission, which in the simplest case is polarized by the same magnetic fields. The W-band EE $\ell = 7$ value is essentially unchanged by cleaning, removing a 10° radius around the Galactic caps, or by additionally masking $\pm 10^\circ$ in the ecliptic plane.

A number of tests have been done to identify this artifact of the data. We are not yet certain if it is due to an ersatz signal or an incorrect noise term. The error bars on the individual year differences are too large to clearly see if the effect is the same from year to year. Simulations show that $1/f$ alone cannot explain the signal. The scan pattern in combination with the change in polarization is directly related to the large error

bars at $\ell = 5, 7, 9$ and is well understood. We have not identified a mechanism that leads to a further increase in these uncertainties. We know that different treatments of the noise, for example using N_{obs} weighting, decreases the magnitude of the discrepancy, though we are confident that the N^{-1} treatment of the pixel noise is the correct approach. The discrepancy can be made smaller by eliminating the W1 data simply because the error bars increase. The W1 radiometer has the lowest noise but also the largest number of “glitches” (13, 4, 1 in years 1, 2, & 3 respectively, Limon et al. 2003; Hinshaw et al. 2003b). However, since we could not identify any correlation between the glitch rate (assuming that unmasked glitches are responsible) and the magnitude of the signal, we do not have a basis for eliminating this channel.

We believe there is an as yet unknown coupling in the W-band data that is driving the signal but more simulations and more sensitivity are needed to understand it. We cannot rule out similar lower-level problems in other bands, but we see no evidence of systematic effects in BB, EB, or other values of ℓ and other frequencies in EE. To avoid biasing the result by this residual artifact which also possibly masks some unmodeled dust and synchrotron contamination, we limit the cosmological analysis to the QV combination. We also show that including W band EE does not alter our conclusions.

5.4. Analysis of Foreground-Cleaned Power Spectra Outside the P06 Mask.

A comparison of the raw spectra and foreground cleaned spectra is shown in Figure 21. We start with the weighted sum of the 8 cross spectra with $\nu > 40$ GHz (without KW). This is the upper-level line (green) in the figure. The individual maps are then cleaned and the power spectra remade and coadded. This is shown in violet. Similar comparisons are repeated for the QVW and QV combinations. A simple visual inspection shows that even at the ℓ s with the highest foreground contamination, the cleaning is effective.

From the bottom left panel in Figure 21 one sees that there is a clear signal above the noise in EE at $\ell < 7$. For the QV combination, $\mathcal{B}_{\ell < 2-6}^{EE} = 0.086 \pm 0.029 (\mu K)^2$. The signal has persisted through a number of different analyses. We cannot rule out that this signal might find explanation in an unmodeled foreground component; however, we find this explanation unlikely since the emission would have to be strikingly different from the measured spatial and frequency characteristics of the polarized foreground emission. Additionally, when different bands are coadded, the signal level is consistent: for QVW $\mathcal{B}_{\ell < 2-6}^{EE} = 0.098 \pm 0.022 (\mu K)^2$ and for all channels with $f > 40$ GHz except KW, $\mathcal{B}_{\ell < 2-6}^{EE} = 0.095 \pm 0.019 (\mu K)^2$. We have searched for systematic effects in the EE $\ell = 2 - 8$ range and have not been able to identify any, other than the one discussed above. We cannot find a more plausible explanation than that the signal is in the sky. We are thus led to interpret it cosmologically. This is done in the next section.

We show the EE signal for $\ell > 20$ in Table 8 and in Figure 22 along with a comparison to other recent measurements (Leitch et al. 2005; Sievers et al. 2005; Barkats et al. 2005; Montroy et al. 2005). Based on the best fit to the TT spectra, we produce a template for the predicted EE spectrum $C_{\ell}^{EE,T}$ and form:

$$\chi^2(A^{EE}) = \sum_{\ell=50}^{800} \delta C_{\ell} Q_{\ell}^{EE} \delta C_{\ell} \quad (28)$$

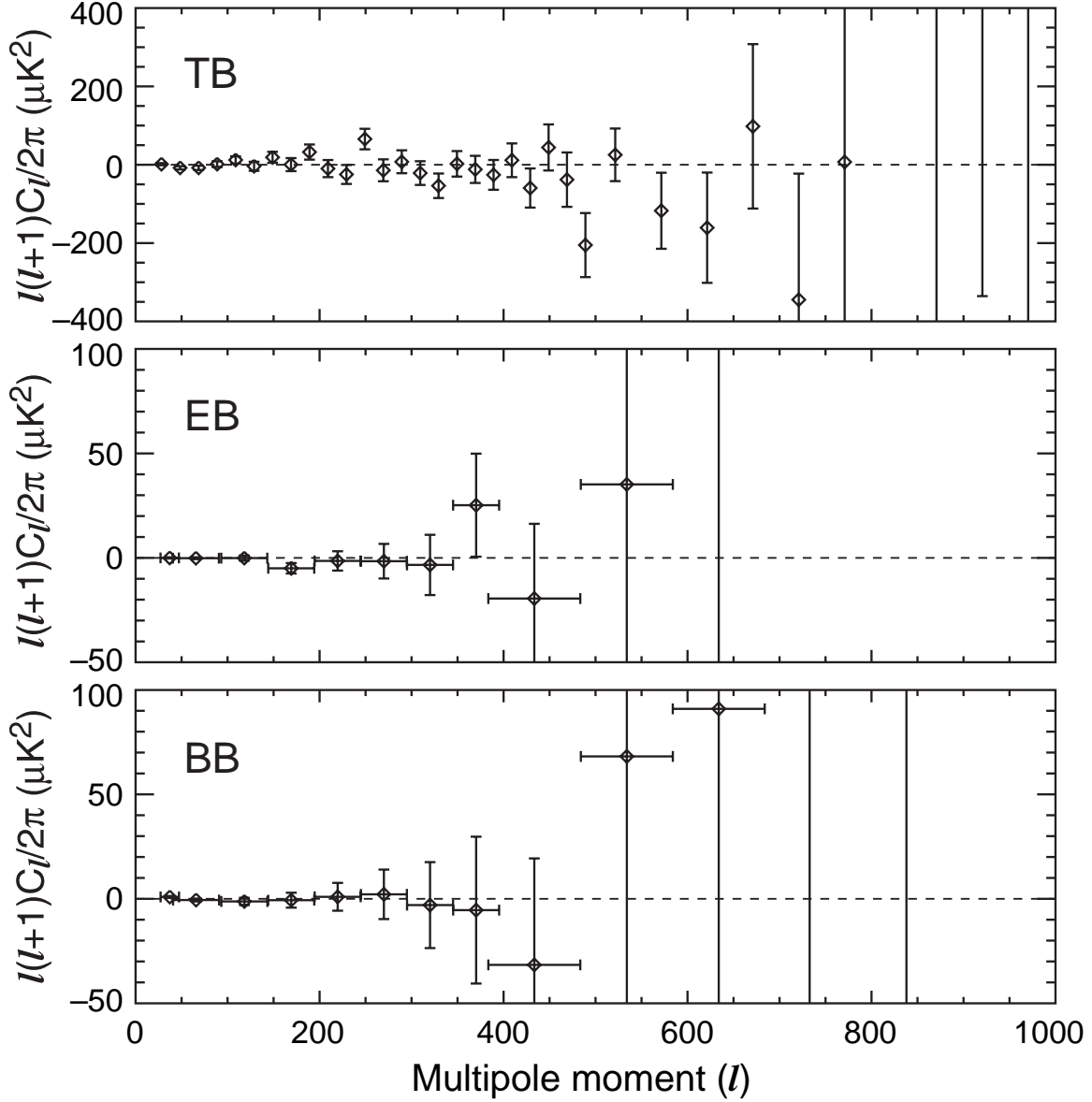


FIG. 20.— Plots of all the noise for the expected null combinations of TB, EB, BB for the region outside the P06 mask. For T the foreground-cleaned V and W bands have been combined bands. For E and B, the foreground-cleaned Q and V bands have been combined. Cosmic variance is included for all plots. For each plot there are 999 ℓ values that have been averaged into 33 bins for TB and 12 bins for EB and BB. For TB, $\chi^2/\nu = 41.6/33$ and $\chi^2/\nu = 931/999$ with corresponding $PTE = 0.15$ and 0.94 for the two binnings. For EB, $\chi^2/\nu = 7.5/12$ and $\chi^2/\nu = 956/999$ with corresponding $PTE = 0.82$ and 0.84 . For BB, $\chi^2/\nu = 6.2/12$ and $\chi^2/\nu = 1000/999$ with corresponding $PTE = 0.91$ and 0.49 . The polarization maps have been cleaned as described in Section §4.3. See also Table 6.

where $\delta C_\ell = C_\ell^{EE} - A^{EE} C_\ell^{EE,T}$, A^{EE} is the fit amplitude, and $Q_{\ell\ell}^{EE}$ is the diagonal Fisher matrix in Appendix C.3. Off diagonal elements in $Q_{\ell\ell'}^{EE}$ have a negligible effect on the results.

The results of the fit are plotted in Figure 23 for various frequency combinations. We plot $\Delta\chi^2$ from the minimum value and find that $A^{EE} = 0.95 \pm 0.35$ for the pre-cleaned QVW combination, where the uncertainty is determined from the bounds at $\Delta\chi^2 = 1$. The reduced χ^2 at the minima are 1.34, 1.34, 1.24, and 1.30 for QV, VW, QVW, and KaQVW combinations respectively, most likely indicating residual foreground contamination. At a relative amplitude of zero, $\Delta\chi^2 = 1.0, 3.3, 6.2, \& 16$ respectively for the same frequency combinations. It is clear that the noise is not yet low enough to use just QV as was done at low multipoles. In addition, cleaning

the maps with the KD3Pol is problematic because the K-band window function is reduced to 0.1 by $\ell = 250$. When the same code is used to analyze EB and BB data, the fitted amplitude is always consistent with zero. To summarize, the WMAP EE data are consistent with a model of adiabatic fluctuations based on the temperature maps at greater than the 2σ level for the QVW and KaQVW combinations.

Figure 24 (left panel) shows the TE spectrum for $\ell < 16$. We use V band for temperature and the QV combination for polarization. Several aspects of the new processing led to increased errors and a reduced low- ℓ signal estimate relative to the first-year result (Figure 8, Kogut et al. 2003). These include: improvements in mapmaking and power spectrum estimation (especially accounting for correlated noise and ap-

TABLE 6
 χ^2/ν FOR TE, TE (2003), TB, EE, BB, AND EB

	r4 ^a	r9 ^{b,f}	r9	r9
	$l = 2 - 16$ ($\nu = 15$ dof)	$l = 17 - 100$ ($\nu = 84$ dof)	$l = 17 - 500$ ($\nu = 484$ dof)	$l = 17 - 800$ ($\nu = 784$ dof)
TE ^{c,e,g}	0.31 (0.99) ^f	1.01 (0.46)	1.20(<0.01)	1.08(0.06)
TE (2003) ^d	1.88 (0.03)	1.18 (0.25)	2.06 (0)	...
TB ^{c,g}	0.57 (0.90)	0.72 (0.97)	0.97 (0.70)	0.97 (0.74)
EE ^c	1.34 (0.17)	1.06 (0.33)	0.98 (0.59)	0.96 (0.76)
BB ^c	0.72 (0.77)	1.28 (0.04)	0.96 (0.73)	0.95 (0.81)
EB ^c	0.41 (0.98)	1.21 (0.09)	1.03 (0.34)	0.96 (0.76)

Notes for all entries. χ^2/ν is computed for the null model ($C_l^{XX} = 0$). a) r4 HEALPix maps are used for $\ell < 32$. We limit this to $\ell < 17$ to avoid pixel window effects. b) r9 HEALPix maps are used for $16 < \ell < 800$. c) For all results a model of the foreground emission has been removed. d) TE (2003) corresponds to Kogut et al. (2003). e) The numbers in parentheses are the PTEs. f) For $\ell > 16$, we use the binned diagonal elements of the covariance matrices in Appendix C.3. g) For TE and TB, the E and B are comprised of a combination of Q and V bands and the T is from V and W bands.

TABLE 7
 χ^2/ν FOR R4 YEARLY DIFFERENCE NULL MAPS

	y _{r1} - y _{r2}	y _{r2} - y _{r3}	y _{r1} - y _{r3}
	$l = 2 - 16$ ($\nu = 15$ dof)	$l = 2 - 16$ ($\nu = 15$ dof)	$l = 2 - 16$ ($\nu = 15$ dof)
TE	1.70 (0.04)	1.05 (0.40)	1.87 (0.02)
TB	1.95 (0.02)	1.20 (0.26)	1.08 (0.37)
EE	1.55 (0.08)	0.89 (0.58)	0.55 (0.91)
BB	0.56 (0.90)	1.50 (0.09)	0.76 (0.72)
EB	0.62 (0.86)	1.04 (0.41)	0.84 (0.63)

Notes for all entries. χ^2/ν is computed for the null model, $C_l^{XX} = 0$.

plying N^{-1} weighting); limiting the bands to just Q and V instead of Ka-W; increasing the cut from KP0 to P06; and improvements in foreground modeling, including a new estimate of dust polarization. Recall also that the first-year result was based on the combinations of Ka, Q, V, and W bands and did not include a dust polarization template in contrast to the new prescription. Furthermore, if the year-two data are processed in the same way as the first-year data, we obtain a spectrum similar to that in Kogut et al. (2003) indicating that the major difference between first-year and three-year results rests on new knowledge of how to make and clean polarization maps. The new spectrum is fully consistent with the first-year results and prefers a model based just on TT and EE data to a null signal at the 2σ level. However, the new spectrum is also consistent with the absence of a TE signal. Thus, it will take greater signal-to-noise to clearly identify the TE signal with our new analysis methods.

Figure 24 (right panel) shows the TE signal over the full range in ℓ . Other detections of TE at $\ell > 100$ have been reported by DASI (2.9σ) (Leitch et al. 2005), Boomerang (3.5σ) (Piacentini et al. 2005), and CBI (3.3σ) (Sievers et al. 2005). The WMAP data have had foreground models subtracted from both the temperature and polarization maps prior to forming the cross correlation. The expected anticorrelation between the polarization and temperature is clearly evident. To quantify the consistency with the TT data we make a TE template based on the model fit to TT. Next, a fit is made to the TE data for $20 < \ell < 500$ with the following:

$$\chi^2(A^{TE}, \Delta\ell) = \sum_{\ell\ell'} \delta C_\ell Q_{\ell\ell'}^{TE} \delta C_{\ell'} \quad (29)$$

where $\delta C_\ell = C_\ell^{TE} - A^{TE} C_\ell^{TE,T}(\Delta\ell)$, $C_\ell^{TE,T}(\Delta\ell)$ is the predicted power spectrum shifted by $\Delta\ell$, A^{TE} is the fit amplitude, and $Q_{\ell\ell'}^{TE}$ is the diagonal Fisher matrix in Appendix C.3. Off diagonal elements in $Q_{\ell\ell'}^{TE}$ have a negligible effect on the results. Similar 2D fits were done in Readhead et al. (2004). We show the combination that uses V and W bands for T and Q and V bands for E. The result, shown in Figure 23, is $A^{TE} = 0.93 \pm 0.12$ and $\Delta\ell = 0 \pm 8$ with $\chi^2/\nu = 468/482$ (PTE=0.66). Similar results are obtained with other band combinations. Thus the TE data are consistent with the TT data to within the limits of measurement.

Figure 25 shows a summary of the various components of the CMB anisotropy.

6. COSMOLOGICAL ANALYSIS

The $\ell < 100$ region of the CMB polarization spectra is rich with new tests of cosmology. The EE spectrum gives us a new measure of the optical depth. The same free electrons from reionization that lead to the $\ell < 10$ EE signal act as test particles that scatter the quadrupolar temperature anisotropy produced by gravitational waves (tensor modes) originating at the birth of the universe. The scatter results in polarization B modes. Tensor modes also affect the TT spectrum in this region. A combination of these and related observations leads to direct tests of models of inflation.

The detection of the TE anticorrelation near $\ell \approx 30$ is a fundamental measurement of the physics of the formation of cosmological perturbations (Peiris et al. 2003). It requires some mechanism like inflation to produce and shows that super-horizon fluctuations must exist. Turok (1996) showed that with enough free parameters one could in principle make a

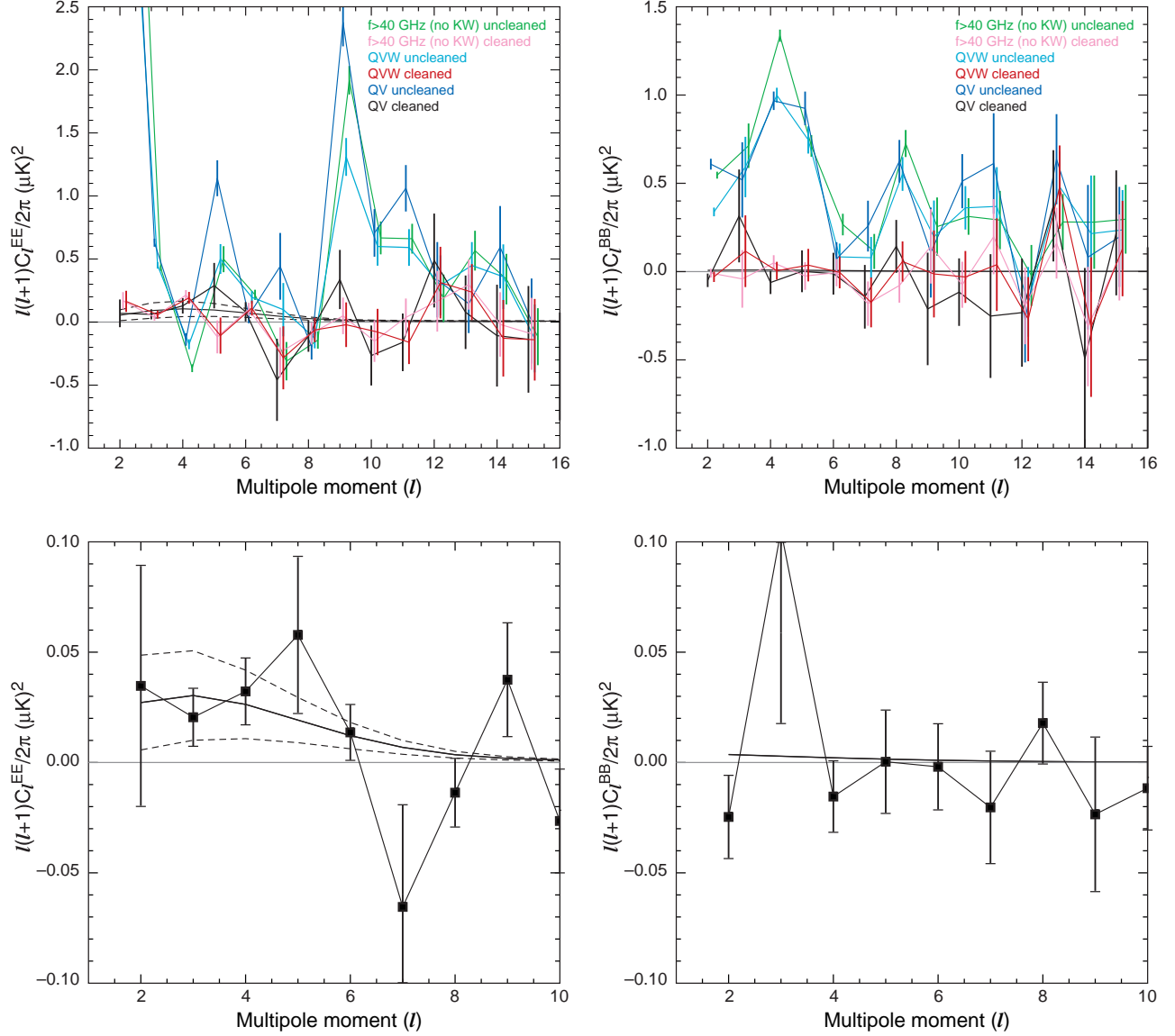


FIG. 21.— *Top*: The EE and BB power spectra outside the P06 mask before and after applying the KD3Pol foreground model. Different colors show different frequency combinations. Negative values are possible due to anticorrelations between foreground components, and to a lesser degree, from the coupling between different values of ℓ . Only statistical uncertainties are shown. For EE, the smooth black lines are the best fit model to the TT, TE, and EE data. The cosmic variance uncertainty is indicated by the dashed lines. The EE values at $\ell = 2$ are $5.8, 4.5, \& 5.5 \mu\text{K}^2$ for $f>40$ (no KW), QVW, and QV combinations respectively. To clean these to a level of $0.1 \mu\text{K}^2$ requires cleaning the Stokes Q and U maps to one part in eight. The BB foreground emission is generally less than half the EE emission. *Bottom*: Expanded plots of the QV data for the P06 cut. The models are for $\tau = 0.09$ and $r = 0.3$.

TABLE 8
BINNED DATA FOR \mathcal{B}^{EE}/ℓ FOR $\ell > 20$

	$30 \leq \ell \leq 50$	$51 \leq \ell \leq 150$	$151 \leq \ell \leq 250$	$251 \leq \ell \leq 350$	$351 \leq \ell \leq 450$	$451 \leq \ell \leq 650$	$651 \leq \ell \leq 1023$
QV	0.010 ± 0.007	0.011 ± 0.005	-0.001 ± 0.012	-0.003 ± 0.026	-0.014 ± 0.058	0.16 ± 0.12	-0.73 ± 0.66
VW	0.013 ± 0.011	0.004 ± 0.004	0.017 ± 0.009	0.027 ± 0.018	0.031 ± 0.037	0.095 ± 0.065	0.13 ± 0.22
QVW	0.013 ± 0.006	0.004 ± 0.004	0.017 ± 0.009	0.027 ± 0.018	0.031 ± 0.037	0.095 ± 0.065	0.13 ± 0.22
KaQVW	0.016 ± 0.004	0.011 ± 0.003	0.012 ± 0.007	0.020 ± 0.016	0.065 ± 0.035	0.097 ± 0.064	0.12 ± 0.22
QV ^a	0.005 ± 0.009	0.018 ± 0.007
VW ^a	0.013 ± 0.011	0.001 ± 0.008
QVW ^a	0.012 ± 0.007	0.006 ± 0.005
KaQVW ^a	0.005 ± 0.005	0.020 ± 0.004

All entries have units of $(\mu\text{K})^2$. The top set is for combinations of the pre-cleaned data. Sample variance is not included. The bottom set is for data cleaned with the KD3Pol model. Note that the cleaning has little affect on the $51 \leq \ell \leq 150$ bin other than to increase the uncertainty.

model based on post-inflation causal physics that reproduced

the TT spectrum. Spergel & Zaldarriaga (1997) show that the

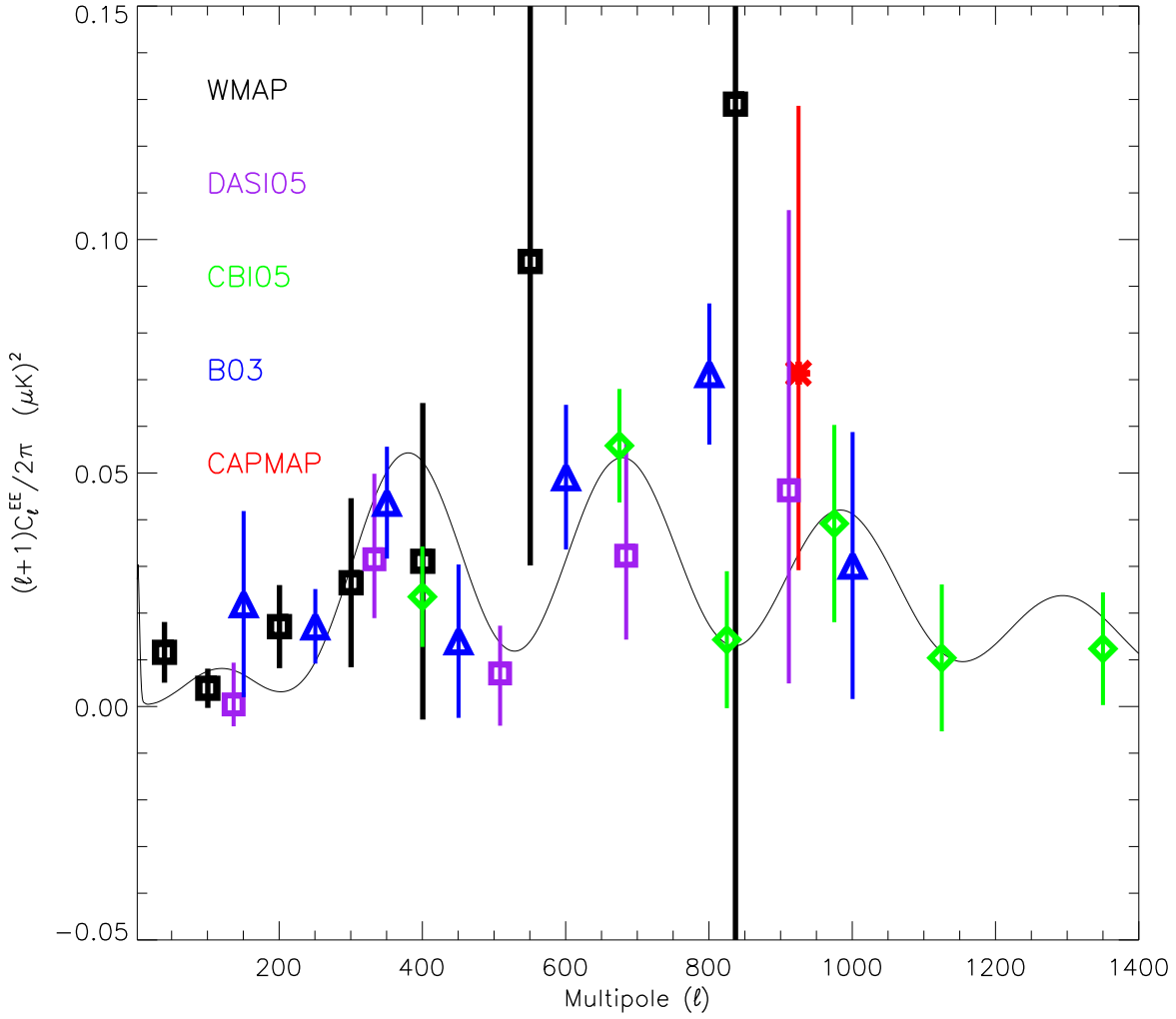


FIG. 22.— The EE spectrum at $\ell > 40$ for all measurements of the CMB polarization. The curve is the best fit EE spectrum. Note that the y axis has only one power of ℓ . The black boxes are the WMAP data; the triangles are the BOOMERanG data; the squares are the DASI data; the diamonds are the CBI data; and the asterisk is the CAPMAP data. The WMAP data are the QVW combination. For the first point, the cleaned value is used. For other values, the raw values are used. The data are given in Table 8

TE anticorrelation is characteristic of models with superhorizon fluctuations. The reason is that the anticorrelation is observed on angular scales larger than the acoustic horizon at decoupling. Thus, the observed velocity-density correlations implied by the TE data must have existed on scales larger than the horizon and were not produced by post-inflation causal processes.

Although multiple distinct physical mechanisms affect the $\ell < 100$ spectra, their effects can be disentangled through an analysis of the full data complement (Spergel et al. 2006). The separation, though, is not perfect and there remain degeneracies. In particular, to some degree, the values of the scalar spectral index, n_s , optical depth, and the tensor to scalar ratio, r , may be traded against each other, although far less than in the first-year WMAP results. As the data improve, or as more data sets are added, the degeneracy is broken further. In the following we take a step back from the full MCMC analysis (Spergel et al. 2006) and estimate τ and r from analyses of just the $\ell < 10$ polarization spectra. This approach aids our intuition in understanding what it is in the data that constrains the cosmological parameters.

6.1. The Optical Depth of Reionization

Our knowledge of the optical depth ripples through the assessment of all the cosmic parameters. Free electrons scatter the CMB photons thereby reducing the amplitude of the CMB spectrum. This in turn directly impacts the determination of other parameters.

The distinctive signature of reionization is at $\ell < 10$ in EE. The only known contamination is from foreground emission which has been modeled and subtracted. The amplitude of the reionization signal is proportional to τ in TE and is proportional to τ^2 in EE and BB. In the first year analysis, we imposed a prior that $\tau < 0.3$ (Spergel et al. 2003). Such a high value would produce a signal > 6 times the model in Figure 21 and is clearly inconsistent with the EE data. Thus this new analysis is a significant improvement over the previously assumed prior.

We assess τ using three methods: (1) with template fits to the EE power spectra; (2) with an exact likelihood technique based directly on the maps as described in Appendix D; and (3) with a multiparameter MCMC fit to all the data as reported in Spergel et al. (2006). The first method is based directly on the MASTER spectrum (Hivon et al. 2002, and Appendix B)

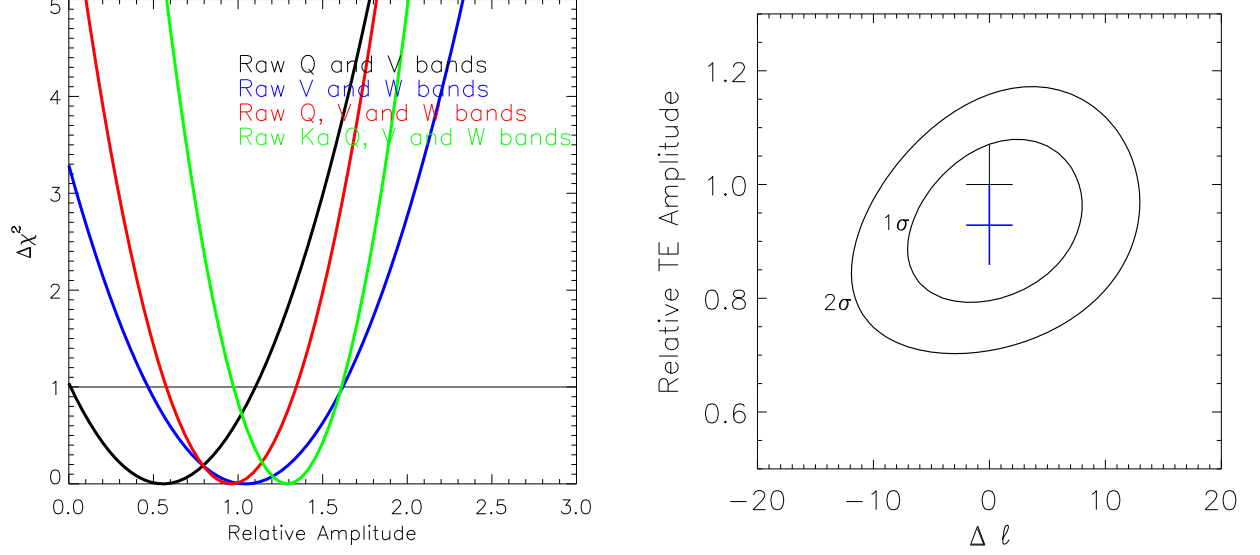


FIG. 23.— *Left*: Lines of $\Delta\chi^2$ for the fit given in Equation 28 vs. A^{EE} . The different colors correspond to different frequency combinations. If the EE prediction from the TT measurements describes the EE measurements, then the minimum would be at $A^{EE} = 1$. The line at $\Delta\chi^2 = 1$ corresponds to the 1σ error. One can see that the $\ell > 50$ EE data are consistent with the model. *Right*: The amplitude and phase of the TE measurement with respect to the model predicted by the TT data. If the TE were completely predicted by the model based on TT, the contours would be consistent with $A^{TE}, \Delta\ell^{TE} = (1, 0)$. It is clear that the TT model describes the TE data as well. The reduced χ^2 for the best fit model is 0.67. To convert $\Delta\ell$ to a phase angle in degrees, multiply by 1.18.

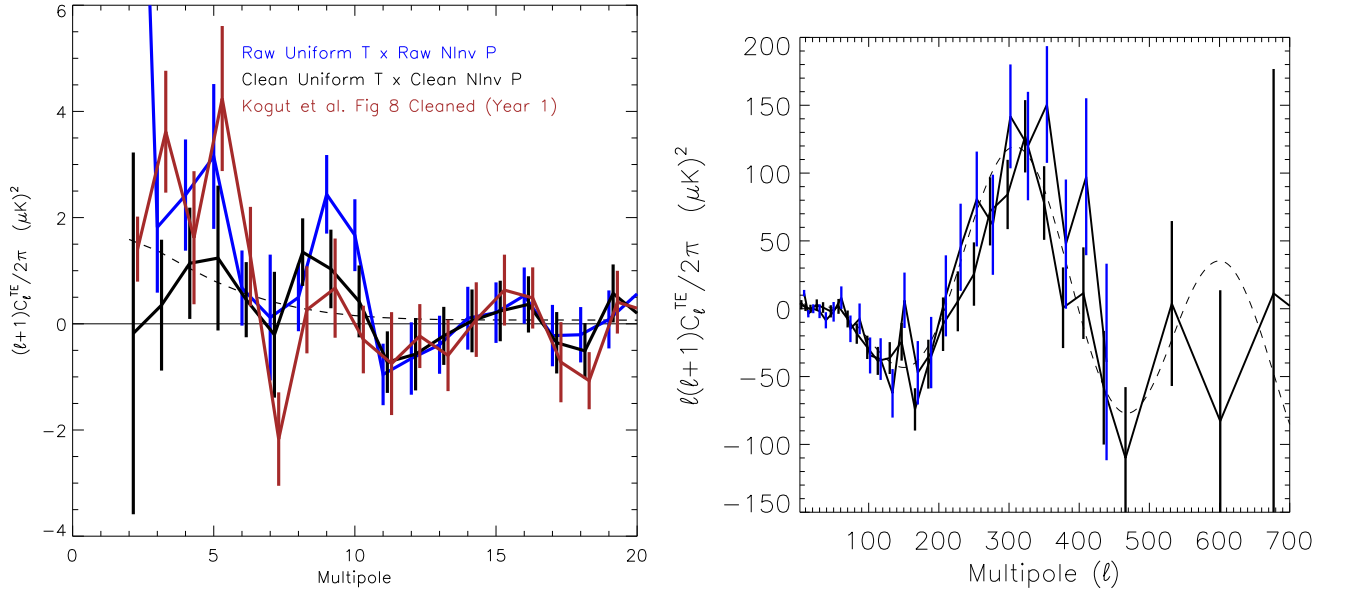


FIG. 24.— The TE power spectra for high and low ℓ ranges for the region outside the P06 mask in EE and outside the KP2 mask for TT. *Left*: At low ℓ we use the QV combination for polarization with full \mathbf{N}^{-1} weighting, and for temperature we use V band with uniform weighting. The black data points correspond to spectrum made with the KD3Pol cleaned polarization maps; the blue correspond to the same spectrum but without cleaning (the $\ell = 2$ point is at $17.8 \pm 3.4 \mu\text{K}$), and the brown are from Kogut et al. (2003). The black dashed line is the best fit model to all the WMAP data. For the first-year data, $\chi^2 = 35.3$ for $\ell = 2-10$ with a corresponding $PTE \approx 0$. For the three-year data, $\chi^2 = 9.4$ for $\ell = 2-10$ evaluated relative to a null signal. The corresponding PTE is 0.4. When the three-year data are evaluated with respect to the best-fit model, $\chi^2 = 5.4$ with a corresponding $PTE = 0.79$. We find that the data sets are consistent with each other and that the three-year data prefer the $\tau = 0.09$ model over the null signal at the 2σ ($\Delta\chi^2 = 4$) level. However, the three-year data are also consistent with a null signal. *Right*: The black data points show the three-year TE spectrum. The blue data points are from Kogut et al. (2003). The smooth dashed curve is the best fit model to the WMAP data. An additional zero crossing near $\ell = 400$ is now present.

of EE data and serves as a simple check of the other two. Additionally, the simplicity allows us to examine the robustness of the EE and TE detections to cuts of the data. The second method is robust and takes into account the phases of the EE and TE signals. It is run either as a stand alone method, as reported here, or as part of the full MCMC chain as reported in Spergel et al. (2006). The best estimate of the optical depth comes from the full chains.

For the template fits, ΛCDM power spectra were generated for $0 \leq \tau \leq 0.3$, with the remaining parameters fixed to $n_s = 0.96$, $\omega_b = 0.0226$, $\omega_m = 0.133$, and $h = 0.72$. For each spectrum, the scalar amplitude A is fixed by requiring that

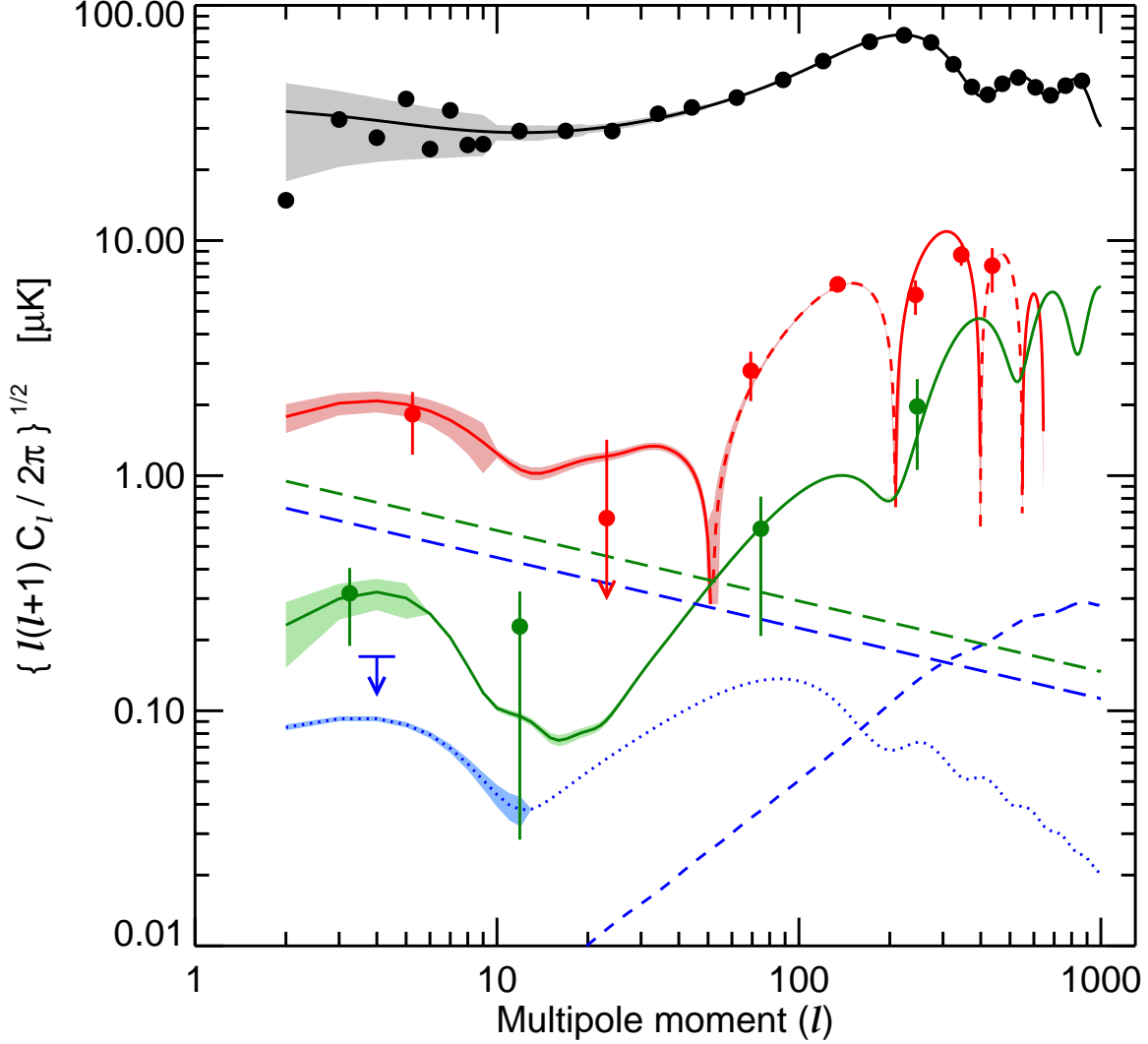


FIG. 25.— Plots of signal for TT (black), TE (red), EE (green) for the best fit model. The dashed line for TE indicates areas of anticorrelation. The cosmic variance is shown as a light swath around each model. It is binned in ℓ in the same way as the data. Thus, its variations reflect transitions between ℓ bin sizes. All error bars include the signal times noise term. The ℓ at which each point is plotted is found from the weighted mean of the data comprising the bin. This is most conspicuous for EE where the data are divided into bins of $2 \leq \ell \leq 5$, $6 \leq \ell \leq 49$, $50 \leq \ell \leq 199$, and $200 \leq \ell \leq 799$. The lowest ℓ point shows the cleaned QV data, the next shows the cleaned QVW data, and the last two show the pre-cleaned QVW data. There is possibly residual foreground contamination in the second point because our model is not so effective in this range as discussed in the text. For BB (blue dots), we show a model with $r = 0.3$. It is dotted to indicate that at this time WMAP only limits the signal. We show the 1σ limit of $0.17 \mu\text{K}$ for the weighted average of $\ell = 2 - 10$. The BB lensing signal is shown as a blue dashed line. The foreground model (Equation 25) for synchrotron plus dust emission is shown as straight dashed lines with green for EE and blue for BB. Both are evaluated at $\nu = 65$ GHz. Recall that this is an average level and does not emphasize the ℓ s where the emission is low.

$\mathcal{B}_{\ell=200}^{TT} = 5589 \mu\text{K}^2$. We then form:

$$\mathcal{L}(\tilde{\tau}) = \frac{1}{(2\pi)^n \sqrt{\det(D)}} \exp\left[-\sum_{\ell} (\vec{x}_{\ell} - \vec{x}_{\ell}^h) D^{-1} (\vec{x}_{\ell} - \vec{x}_{\ell}^h) / 2\right] \quad (30)$$

where \vec{x}_{ℓ} is the data as shown in Figure 21, $\vec{x}_{\ell}^h = \mathcal{B}_{\ell}^{EE}(\tilde{\tau})$ is the model ΛCDM spectrum,

$$D_{\ell} = \frac{2}{2\ell+1} \frac{1}{f_{\text{sky}}^{EE}(\ell)^2} (\mathcal{B}_{\ell}^{EE}(\tilde{\tau}) + N_{\ell}^{EE})^2 \quad (31)$$

as in C.14, and N_{ℓ}^{EE} is the uncertainty shown in Figure 21 and is derived from the MASTER spectrum determination. We use the symbol $\tilde{\tau}$ in this context because the likelihood function we obtain is not the full likelihood for τ . Uncertainties

in other parameters, especially n_s , have been ignored and the C_{ℓ} distribution is taken to be Gaussian. Thus $\mathcal{L}(\tilde{\tau})$ does not give a good estimate of the uncertainty. Its primary use is as a simple parametrization of the data. $\mathcal{L}(\tilde{\tau})$ is plotted in Figure 26 for the QV combination. We call this method “simple tau.” Table 9 shows that simple tau is stable with data selection. One can also see that if the QQ component is removed from the QV combination, τ increases slightly. This is another indication that foreground emission is not biasing the result. Additionally, one can see that removing $\ell = 5, 7$ for all band combinations does not greatly affect τ .

The optimal method for computing the optical depth is with the exact likelihood (as in Appendix D). The primary benefits are: it makes no assumptions about the distribution of C_{ℓ} at

each ℓ but does assume that the polarization signal and noise in the maps are normally distributed; it works directly in pixel space, taking advantage of the phase relations between the T and E modes both together and separately; and it is unbiased. The only disadvantages are that it is computationally intensive and that it is not easy to excise individual values of ℓ such as $\ell = 5, 7$. Table 9 shows that similar values of τ are obtained for a wide variety of band combinations. This is another indication that foreground emission is not significant. We conservatively select the QV combination. Figure 26 and Table 9 compare the exact likelihood for the EE QV combination to the simple tau method. One can see that simple tau is slightly biased high when compared to the exact likelihood and underestimates the likelihood at $\tau = 0$. One source of the bias is the assumption of a Gaussian likelihood. Nevertheless, it is reassuring that a variety of combinations of data give consistent values of τ . The values given here are just for the EE and TE data considered alone, with the first peak TT amplitude fixed. When the exact likelihood is used in the full MCMC analysis (Spergel et al. 2006) yielding the best estimate, we find $\tau = 0.088^{+0.028}_{-0.034}$, slightly lower than the values reported here but with the same uncertainty, indicating that the simple analysis has exhausted most of the information on the optical depth contained in the polarization data.

6.2. Gravitational Waves

The C_{ℓ}^{BB} spectrum directly probes the primordial gravitational wave background produced by tensor fluctuations in the early universe. The existence of these gravitational waves was proposed by Starobinsky (1979). Modern treatments may be found in, for example, Liddle & Lyth (2000); Dodelson (2003); Mukhanov (2005). While scalar and tensor fluctuations both contribute to the TT and EE spectra, only tensors produce B modes. Inflation models generally predict similar scalar spectra, but differ in their prediction of the tensor component. For example, ekpyrotic/cyclic models (Khoury et al. 2002; Steinhardt & Turok 2002) predict no observable tensor modes.

The tensor contribution is quantified with the tensor to scalar ratio r . We follow the convention in the CAMB code (Lewis et al. 2000, Version, June 2004), in CMBFAST v4.5.1 (Seljak & Zaldarriaga 1996) and in Peiris et al. (2003); Verde et al. (2003):

$$r \equiv \frac{\Delta_h^2(k_0)}{\Delta_{\mathcal{R}}^2(k_0)}. \quad (32)$$

Here, $\Delta_{\mathcal{R}}^2$ and Δ_h^2 are the variance due to scalar and tensor modes respectively. They are defined through

$$\langle \mathcal{R}^2 \rangle = \int \frac{dk}{k} \Delta_{\mathcal{R}}^2(k) \quad (33)$$

$$\text{and } \langle h_{ij}^{prim} h^{prim,ij} \rangle = \int \frac{dk}{k} \Delta_h^2(k), \quad (34)$$

where h_{ij}^{prim} is the primordial tensor metric perturbation in real space that was generated during inflation and stretched to outside the horizon²³. Peiris et al. (2003) shows the k -dependence of these expressions.

The expression for r is evaluated at $k_0 = 0.002 \text{ Mpc}^{-1}$ corresponding to $l \approx \eta_0 k = 30$ with the distance to the decoupling

surface $\eta_0 \approx 14,400 \text{ Mpc}$. Following Verde et al. (2003), we use $\Delta_{\mathcal{R}}^2(k_0) = 2 \times 10^4 \pi^2 A(k_0) / 9T_0^2 \approx 2.95 \times 10^{-9} A(k_0)$ with T_0 in microkelvins. Some of the simple models of inflation in a Λ CDM cosmology predict $r \simeq 0.3$ (e.g., Liddle & Lyth 2000; Boyle et al. 2005). For example, near this range inflationary models with a massive scalar field, $V(\phi) = m^2 \phi^2 / 2$, predict $r = 8/N_e = 4(1 - n_s) = 0.13 - 0.16$ (Linde 1983) and models with a self coupling, $V(\phi) = \lambda \phi^4 / 4$, predict $r = 16/N_e = 16(1 - n_s) / 3 = 0.27 - 0.32$ for $N_e = 60 - 50$. Here, N_e is the number of e-foldings before the end of inflation. However, some variants produce $r > 0.32$ (e.g. Mukhanov & Vikman 2005) while many other have $r \ll 0.1$.

For the best fit WMAPonly Λ CDM plus tensor model, the optical depth is $\tau = 0.091$. If we add to this model a tensor component with $r = 0.3$, then $\mathcal{B}_{\ell < 2-6}^{BB} = 0.001 \mu\text{K}^2$. A simple average of the C_{ℓ}^{BB} data gives $\mathcal{B}_{\ell < 2-6}^{BB} = -0.044 \pm 0.030 \mu\text{K}^2$, $\mathcal{B}_{\ell < 2-6}^{BB} = -0.018 \pm 0.023 \mu\text{K}^2$, $\mathcal{B}_{\ell < 2-6}^{BB} = 0.003 \pm 0.020 \mu\text{K}^2$, for QV, QVW, and $\nu > 40 \text{ GHz}$ (no KW) combinations respectively. To detect a signal at the upper range of the predictions would require maps with ≈ 5 times smaller error bars.

We constrain r by directly fitting a template of C_{ℓ}^{BB} to the BB data. With the above definition, r directly scales the C_{ℓ}^{BB} power spectrum. Additionally, the amplitude of C_{ℓ}^{BB} for $\ell < 16$ scales as τ^2 . We set the template to be the standard Λ CDM model (Spergel et al. 2006) and use the single field inflation consistency relation, $n_t = -r/8$, to fix the tensor spectral index. We assume the spectral index does not run and set $n_s = 0.96$. We distinguish the r in the template fit by the \tilde{r} notation. The sum is over $2 \leq \ell \leq 11$.

The results of the fit are plotted in Figure 27. When we consider just the limit on \tilde{r} from the polarization spectra, ignoring the tensor contribution to TT, we find $\tilde{r} < 2.2$ (95% CL) after marginalizing over $\tilde{\tau}$. It is clear that the BB spectrum is not driving the limit on r . After including the TT data, the limit drops to $\tilde{r} < 0.27$ (95% CL). This shows that the TT data in combination with the limits on τ from EE and TE are leading to the limit on r . The full MCMC analysis gives $r < 0.55$ (95% CL) with just the WMAP data. The increase in the error over the simple method given above is the result of the marginalization over the other parameters, particularly n_s . Additionally, when n_s is allowed to depend on k , the error in r increases dramatically, allowing $r < 1.3$ (95% CL).

We can relate r to the current energy density in primordial gravitational radiation (Krauss & White 1992; Peiris 2003),

$$\Omega_{GW} = \frac{1}{12H_0^2} \int \frac{dk}{k} \Delta_h^2(k) \dot{T}^2(k, \eta), \quad (35)$$

where η is conformal time and the transfer function, $T(k, \eta)$, is given in Equation E18. The approximation given in Equation E31 evaluated for $A = 0.838$ and $\tilde{r} < 2.2$ yields $\Omega_{GW} < 9.6 \times 10^{-12}$ (95% CL) and for $r < 0.55$, $\Omega_{GW} < 2.0 \times 10^{-12}$ (95% CL).

7. DISCUSSION AND CONCLUSIONS

WMAP detects significant levels of polarized foreground emission over much of the sky. The minimum in contamination is near 60 GHz outside the P06 mask. To detect the polarization in the CMB at $\ell < 10$ a model of the foreground emission must be subtracted from the data. This situation differs from that of the analysis of the temperature anisotropy for which the foreground emission may be simply masked as

²³ Note that our convention yields $r = 16\epsilon$ for slow-roll inflationary models with a single scalar field. Here, ϵ is the slow roll parameter related to the square of the slope of the inflaton potential.

TABLE 9
OPTICAL DEPTH VS. DATA SELECTION

Combination	Exact EE Only	Exact EE & TE	Simple tau EE	Simple tau, no $\ell = 5, 7$
KaQV	0.111 ± 0.022	0.111 ± 0.022
Q	0.100 ± 0.044	0.082 ± 0.043	0.08 ± 0.03	0.085 ± 0.03
QV	0.100 ± 0.029	0.092 ± 0.029	0.110 ± 0.027	$0.085^{+0.045}_{-0.015}$
QV+VV	0.145 ± 0.03	$0.14^{+0.02}_{-0.06}$
V	0.089 ± 0.048	0.094 ± 0.043	$0.09^{+0.03}_{-0.07}$	$0.10^{+0.03}_{-0.07}$
QVW	0.110 ± 0.021	0.101 ± 0.023	0.090 ± 0.012	0.090 ± 0.015
KaQVW	0.107 ± 0.018	0.106 ± 0.019	0.095 ± 0.015	0.095 ± 0.015

The values of simple tau are computed for $2 \leq \ell \leq 11$. The models are computed in steps of $\Delta\tau = 0.005$ and linearly interpolated. The last column is computed with the errors on $\ell = 5, 7$ multiplied by ten. The QV+VV is the QV combination without the QQ component. Since the exact likelihood is based on the Ka, Q, V, and W maps, there is no corresponding entry for QV+VV. Note that the maximum likelihood values are independent of frequency combination indicating that foreground emission is not biasing the determination of τ .

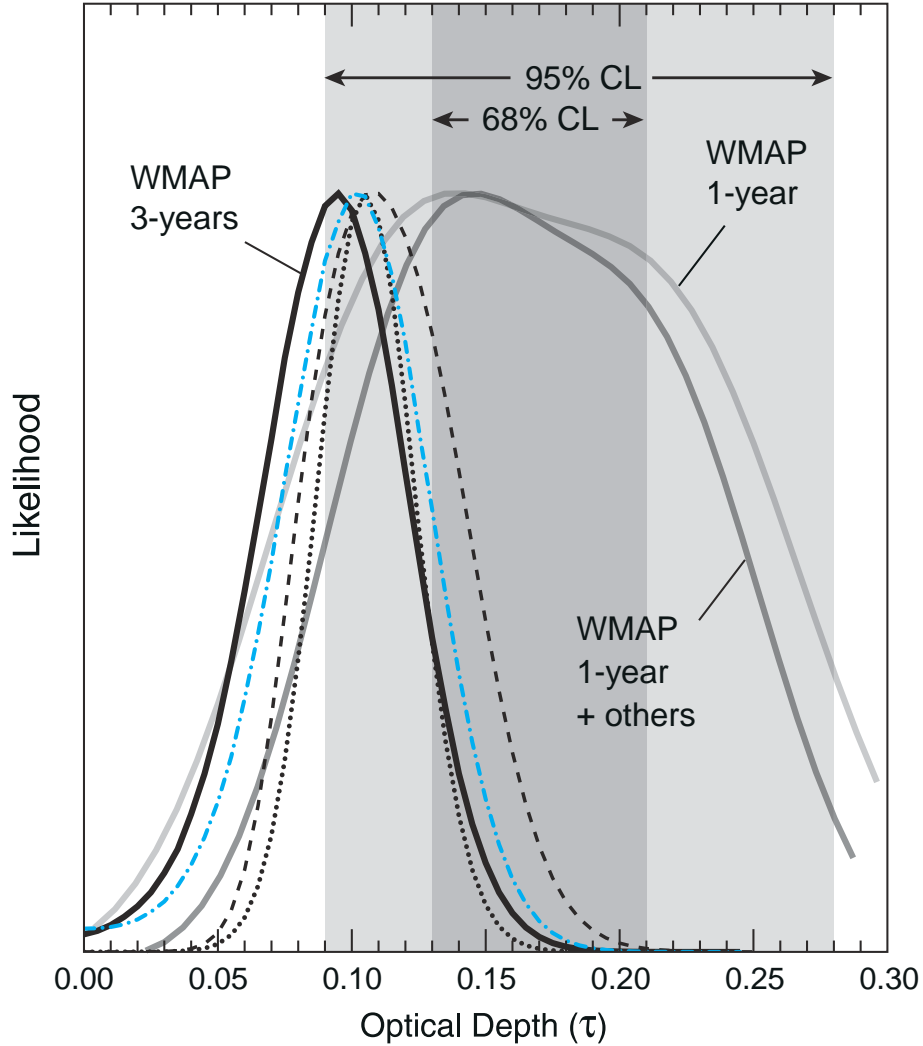


FIG. 26.— The relative likelihoods of τ , τ from the stand alone exact likelihood code, and the first-year results. For the three-year results, all parameters except τ and the scalar normalization, A , were held fixed as described in the text. The solid curve (labeled “WMAP 3-years”) shows the exact likelihood for the QV combination and the combined EE & TE data. The dot-dash line shows the exact likelihood for the QV combination but just for EE. Note that the three-year TE data has little influence on determination of τ . The dotted line shows the exact likelihood for the KaQVW combination indicating that any foreground contamination is small. The dashed line is simple tau for the QV combination. The two curves that peak at higher values of τ are from Spergel et al. (2003) and show the first-year likelihood for the WMAP data alone and for WMAP in combination with other data sets. The darker grey band labeled “68% CL” shows the result reported in Kogut et al. (2003) as a mean of $\tau = 0.17$ and width $\sigma = 0.04$.

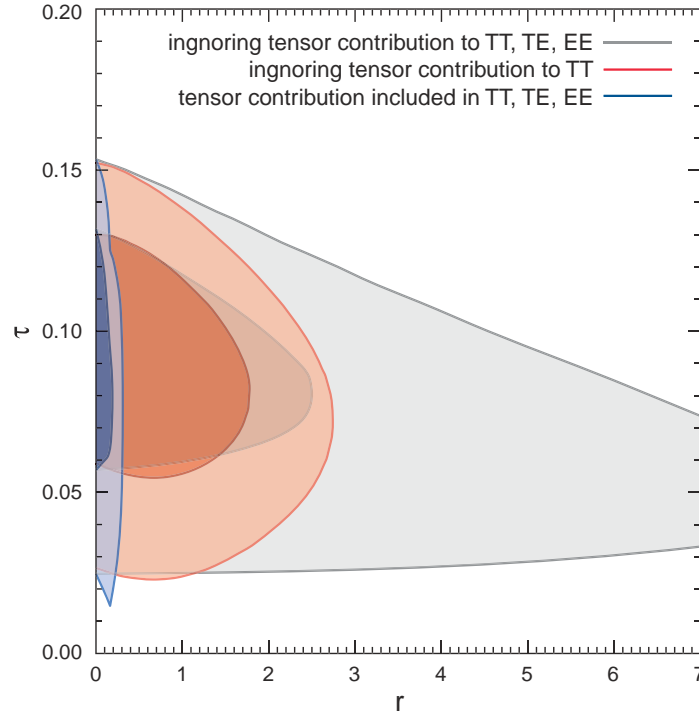


FIG. 27.— The two dimensional likelihood as a function of $\bar{\tau}$ and \bar{r} for the BB spectrum. The contours indicate 1σ and 2σ . The n_s parameter, which is degenerate with τ and r , has been set at $n_s = 0.96$. For the lightest contours, the tensor contribution to TT, TE, and EE is ignored. Because τ is fully degenerate with r when the data are restricted to just BB, the limit is poor. The orange contours show the result when the TE and EE contributions are included, breaking the r - τ degeneracy. The bluish contours show the result of including all data. The limit on r is more restrictive than in Spergel et al. (2006) because n_s is fixed. When we marginalize over $\bar{\tau}$, the 95% upper limits on \bar{r} are 4.5, 2.2, and 0.27 for the three cases respectively. The plot shows that WMAP's ability to constrain r does not yet come from the BB data. The plot also shows that WMAP's ability to limit r depends critically on τ .

a first approximation.²⁴

WMAP has detected the primary temperature anisotropy, the temperature polarization cross correlation, and the E-mode polarization of the CMB. We detect the optical depth with $\tau = 0.088^{+0.028}_{-0.034}$ in a full fit to all WMAP data. This result is supported by stand-alone analyses of the polarization data. Using primarily the TT spectrum, along with the optical depth established with the TE and EE spectra, the tensor to scalar ratio is limited to $r_{0.002} < 0.55$ (95% CL). When the large scale structure power spectrum is added to the mix (Spergel et al. 2006), the limit tightens to $r_{0.002} < 0.28$ (95% CL). These values are approaching the predictions of the simplest inflation models.

A clear detection of the B modes at $\ell < 100$ would give a direct handle on the physics of the early universe at energy scales of $10^{15} - 10^{16}$ GeV. This paper shows that care will be required to unambiguously separate the intrinsic signal from the foreground emission. However, the BB spectrum is particularly clean in WMAP and, at least for $\ell = 2, 3$, the foreground contamination is relatively low. In the noise dominated regime, the error bar on C_ℓ^{BB} decreases in proportion to time. Continued WMAP operations combined with other experimental efforts are nearing a range of great interest.

These new results involve a complete reevaluation of all the components of our previous analyses, from the beams and gain models through to the mapmaking and foreground modeling. The data and most of the derived data products are available through the LAMBDA website,

<http://lambda.gsfc.nasa.gov/>. WMAP continues to operate nominally. In the future we will address a number of the open issues raised above. In particular, we can anticipate a better understanding of systematic errors and foreground emission, and therefore improved constraints on τ and r . It is remarkable that our understanding of the cosmos has reached the point where we have begun to quantitatively distinguish between different models of the birth of the universe.

8. ACKNOWLEDGMENTS

We wish to thank Jo Dunkley, Uros Seljak, Suzanne Staggs, and Paul Steinhardt for enlightening conversations on polarization and inflation, and Jim Peebles for his explanation of reionization. We thank Bruce Draine for helpful discussions on dust polarization. EK acknowledges support from an Alfred P. Sloan Research Fellowship. HVP wishes to acknowledge useful discussions with R. Easther, S. Larson, D. Mortlock, and A. Lewis. The WMAP mission is made possible by the support of the Office of Space Sciences at NASA Headquarters and by the hard and capable work of scores of scientists, engineers, technicians, machinists, data analysts, budget analysts, managers, administrative staff, and reviewers. HVP is supported by NASA through Hubble Fellowship grant #HF-01177.01-A awarded by the Space Telescope Science Institute which is operated by the Association of Universities for Research in Astronomy, Inc., for NASA under contract NAS 5-26555. This research has made use of NASA's Astrophysics Data System Bibliographic Services, the HEALPix software, CAMB software, and the CMBFAST software. This research was additionally supported by NASA LTSA03-000-0090, NASA ATPNNG04GK55G, and NASA ADP03-0000-

²⁴ Of course our full analysis (Hinshaw et al. 2003b) involved extensive modeling of the foregrounds (Bennett et al. 2003b).

092 awards.

REFERENCES

- Abbott, L. F. & Harari, D. D. 1986, *Nucl. Phys.*, B264, 487
- Baccigalupi, C., Burigana, C., Perrotta, F., De Zotti, G., La Porta, L., Maino, D., Maris, M., & Paladini, R. 2001, *A&A*, 372, 8
- Banday, A. J. & Wolfendale, S. 1991, *MNRAS*, 248, 705
- Barkats, D. et al. 2005, *ApJ*, 619, L127
- Barnes, C., et al. 2002, *ApJS*, 143, 567
- . 2003, *ApJS*, 148, 51
- Basko, M. M. & Polnarev, A. G. 1980, *MNRAS*, 191, 207
- Bennett, C. L., et al. 2003a, *ApJS*, 148, 97
- . 2003b, *ApJ*, 583, 1
- Benoît, A., et al. 2004, *A&A*, 424, 571
- Berdyugin, A., Piirola, V., & Teerikorpi, P. 2004, *A&A*, 424, 873
- Berdyugin, A. & Teerikorpi, P. 2001, *A*, 368, 635
- . 2002, *A&A*, 384, 1050
- Berdyugin, A., Teerikorpi, P., Haikala, L., Hanski, M., Knude, J., & Markkanen, T. 2001, *A&A*, 372, 276
- Berkhuijsen, E. M., Haslam, C. G. T., & Salter, C. J. 1971, *A&A*, 14, 252
- Bernardi, G., Carretti, E., Fabbri, R., Sbarra, C., Poppi, S., & Cortiglioni, S. 2003, *MNRAS*, 344, 347
- Blum, E. J. 1959, *Annales D' Astrophysique*, 22, 140
- Bond, J. R. & Efstathiou, G. 1984, *ApJ*, 285, L45
- Bond, J. R. & Efstathiou, G. 1987, *MNRAS*, 226, 655
- Born, M. & Wolf, E. 1980, *Principles of Optics*, sixth edn. (Pergamon Press)
- Boyle, L., Steinhardt, P., & Turok, N. 2005, *Phys. Rev. Lett.*, *Phys. Rev. Lett.*, submitted, (astro-ph/0507455)
- Brouw, W. N. & Spoelstra, T. A. T. 1976, *Astron. Astrophys. Suppl. Ser.*, 26, 129
- Bunn, E. F., Zaldarriaga, M., Tegmark, M., & de Oliveira-Costa, A. 2003, *Phys. Rev. D*, 67, 23501
- Burn, B. J. 1966, *MNRAS*, 133, 67
- Caderni, N., Fabbri, R., Melchiorri, B., Melchiorri, F., & Natale, V. 1978, *Phys. Rev. D*, 17, 1908
- Cioffi, D. F. & Jones, T. W. 1980, *AJ*, 85, 368
- Cortiglioni, S. & Spoelstra, T. A. T. 1995, *A&A*, 302, 1
- Coulson, D., Crittenden, R. G., & Turok, N. G. 1994, *Phys. Rev. Lett.*, 73, 2390
- Crittenden, R., Davis, R. L., & Steinhardt, P. J. 1993, *ApJ*, 417, L13
- Crittenden, R. G., Coulson, D., & Turok, N. G. 1995, *Phys. Rev. D*, 52, 5402
- Davis, L. J. & Greenstein, J. L. 1951, *ApJ*, 114, 206
- de Oliveira-Costa, A., Kogut, A., Devlin, M. J., Netterfield, C. B., Page, L. A., & Wollack, E. J. 1997, *ApJ*, 482, L17+
- de Oliveira-Costa, A., Tegmark, M., Page, L., & Boughn, S. 1998, *ApJ*, 509, L9
- de Oliveira-Costa, A. et al. 1999, *ApJ*, 527, L9
- . 2003, *Phys. Rev. D*, 68
- . 2004, *Astrophys. J.*, 606, L89
- Dodelson, S. 2003, *Modern Cosmology* (Academic Press)
- Draine, B. T. & Lazarian, A. 1998, *ApJ*, 494, L19
- Drimmel, R. & Spergel, D. N. 2001, *ApJ*, 556, 181
- Duncan, A., Reich, P., Reich, W., & Furst, E. 1999, *A&A*, 350, 447
- Duncan, A. R., Haynes, R. F., Jones, K. L., & Stewart, R. T. 1995, *MNRAS*, 277, 36
- Efstathiou, G. 2004, *MNRAS*, 348, 885
- Eisenhauer, F., Schoedel, R., Genzel, R., Ott, T., Tecza, M., Abuter, R., Eckart, A., & Alexander, T. 2003, *ApJ*, 597, 121
- Enomoto, R., et al. 2002, *Nature*, 416, 823
- Erickson, W. C. 1957, *ApJ*, 126, 480
- Faris, J. 1967, *J. Res. Nat. Bur. Stand., Engr. & Instr.*, 71C, 153
- Fernandez-Cerezo, S., et al. 2006, *ArXiv Astrophysics e-prints*
- Finkbeiner, D. P. 2004, *ApJ*, 614, 186
- Finkbeiner, D. P., Davis, M., & Schlegel, D. J. 1999, *ApJ*, 524, 867
- Finkbeiner, D. P., Langston, G. I., & Minter, A. H. 2004, *ApJ*, 617, 350
- Finkbeiner, D. P., Schlegel, D. J., Frank, C., & Heiles, C. 2002, *ApJ*, 566, 898
- Flett, A. M. & Henderson, C. 1979, *MNRAS*, 189, 867
- Flett, A. M. & Murray, A. G. 1991, *MNRAS*, 249, 4P
- Fosalba, P., Lazarian, A., Prunet, S., & Tauber, J. A. 2002, *ApJ*, 564, 762
- Frewin, R. A., Polnarev, A. G., & Coles, P. 1994, *MNRAS*, 266, L21+
- Giardino, G., Banday, A. J., Górski, K. M., Bennett, K., Jonas, J. L., & Tauber, J. 2002, *A&A*, 387, 82
- Górski, K. M., Hivon, E., & Wandelt, B. D. 1998, in *Evolution of Large-Scale Structure: From Recombination to Garching*
- Greaves, J. S., et al. 2003, *MNRAS*, 340, 353
- Grishchuk, L. P. 2001, *Lect. Notes Phys.*, 562, 167
- Han, J.-L. & Wiełebinski, R. 2002, *Chinese Journal of Astronomy and Astrophysics*, 2, 293
- Harari, D. D. & Zaldarriaga, M. 1993, *Physics Letters B*, 319, 96
- Haslam, C. G. T., Stoffel, H., Salter, C. J., & Wilson, W. E. 1982, *A&AS*, 47, 1
- Hedman, M. M., Barkats, D., Gundersen, J. O., McMahon, J. J., Staggs, S. T., & Winstein, B. 2002, *ApJ*, 573, L73
- Heiles, C. 2000, *AJ*, 119, 923
- Hinshaw, G., et al. 2003a, *ApJS*, 148, 63
- . 2003b, *ApJS*, 148, 135
- Hinshaw, G. et al. 2006, *ApJ*, submitted
- Hivon, E., Górski, K. M., Netterfield, C. B., Crill, B. P., Prunet, S., & Hansen, F. 2002, *ApJ*, 567, 2
- Hobbs, R. W., Maran, S. P., & Brown, L. W. 1978, *ApJ*, 223, 373
- Holder, G. P., Haiman, Z., Kaplinghat, M., & Knox, L. 2003, *ApJ*, 595, 13
- Hu, W., Hedman, M. M., & Zaldarriaga, M. 2003, *Phys. Rev. D*, 67, 43004
- Hu, W. & White, M. 1997, *Phys. Rev. D*, 56, 596
- Hummel, E., Dahlem, M., van der Hulst, J. M., & Sukumar, S. 1991, *A&A*, 246, 10
- Jarosik, N., et al. 2003a, *ApJS*, 145, 413
- . 2003b, *ApJS*, 148, 29
- Jarosik, N. et al. 2006, *ApJ*, submitted
- Johnston, K. J. & Hobbs, R. W. 1969, *ApJ*, 158, 145
- Jones, R. C. 1941, *J. Opt. Soc. Am.*, 31, 488
- Jones, T. J., Klebe, D., & Dickey, J. M. 1992, *ApJ*, 389, 602
- Junkes, N., Haynes, R. F., Harnett, J. I., & Jauncey, D. L. 1993, *A&A*, 269, 29
- Kaiser, N. 1983, *MNRAS*, 202, 1169
- Kamionkowski, M., Kosowsky, A., & Stebbins, A. 1997, *Phys. Rev. D*, 55, 7368
- Keating, B. G., O'Dell, C. W., de Oliveira-Costa, A., Klawikowski, S., Stebor, N., Piccirillo, L., Tegmark, M., & Timbie, P. T. 2001, *ApJ*, 560, L1
- Keating, B. G., Timbie, P. T., Polnarev, A., & Steinberger, J. 1998, *ApJ*, 495, 580
- Khouri, J., Ovrat, B. A., Seiberg, N., Steinhardt, P. J., & Turok, N. 2002, *Phys. Rev. D*, 65, 086007
- Kogut, A., Banday, A. J., Bennett, C. L., Górski, K. M., Hinshaw, G., & Reach, W. T. 1996, *ApJ*, 460, 1
- Kogut, A., et al. 2003, *ApJS*, 148, 161
- Kosowsky, A. 1996, *Ann. Phys.*, 246, 49
- Kovac, J. M., Leitch, E. M., Pryke, C., Carlstrom, J. E., Halverson, N. W., & Holzappel, W. L. 2002, *Nature*, 420, 772
- Krauss, L. M. & White, M. 1992, *Physical Review Letters*, 69, 869
- Lagache, G. 2003, *A&A*, 405, 813
- Lawson, K. D., Mayer, C. J., Osborne, J. L., & Parkinson, M. L. 1987, *MNRAS*, 225, 307
- Lazarian, A. & Draine, B. T. 2000, *ApJ*, 536, L15
- Leitch, E. M., Kovac, J. M., Halverson, N. W., Carlstrom, J. E., Pryke, C., & Smith, M. W. E. 2005, *ApJ*, 624, 10
- Leitch, E. M., Readhead, A. C. S., Pearson, T. J., & Myers, S. T. 1997, *ApJ*, 486, L23
- Leitch, E. M., et al. 2002, *Nature*, 420, 763
- Lewis, A., Challinor, A., & Lasenby, A. 2000, *ApJ*, 538, 473
- Lewis, A., Challinor, A., & Turok, N. 2002, *Phys. Rev. D*, 65, 023505
- Liddle, A. R. & Lyth, D. H. 2000, *Cosmological inflation and large-scale structure* (Cambridge University Press)
- Limon, M., et al. 2003, *Wilkinson Microwave Anisotropy Probe (WMAP): Explanatory Supplement*, http://lambda.gsfc.nasa.gov/data/map/doc/MAP_supplement.pdf
- Linde, A. D. 1983, *Phys. Lett.*, B129, 177
- Lubin, P., Melese, P., & Smoot, G. 1983, *ApJ*, 273, L51
- Lubin, P. M. & Smoot, G. F. 1979, *Physical Review Letters*, 42, 129
- . 1981, *ApJ*, 245, 1
- Matveenko, L. I. & Conklin, E. K. 1973, *Soviet Astronomy*, 16, 726
- Mayer, C. H. & Hollinger, J. P. 1968, *ApJ*, 151, 53
- Montgomery, C. G., Dicke, R. H., & Purcell, E. M. 1948, *MIT Radiation Laboratory Series*, Vol. 8, *Principles of Microwave Circuits* (New York: McGraw-Hill)
- Montgomery, J. W., Epstein, E. E., Oliver, J. P., Dworetzky, M. M., & Fogarty, W. G. 1971, *ApJ*, 167, 77
- Montroy, T. E., et al. 2005, *ApJ*
- Mukhanov, V. 2005, *Physical Foundations of Cosmology* (Cambridge University Press)
- Mukhanov, V. & Vikman, A. 2005, *LMU-ASC 78/05*
- Mukherjee, P., Coble, K., Dragovan, M., Ganga, K., Kovac, J., Ratra, B., & Souradeep, T. 2003, *ApJ*, 592, 692
- Nanos, G. P. 1979, *ApJ*, 232, 341
- Netterfield, C. B., Devlin, M. J., Jarosik, N., Page, L., & Wollack, E. J. 1997, *ApJ*, 474, 47
- Ng, K.-w. & Spiliotopoulos, A. D. 1995, *Phys. Rev.*, D52, 2112
- Page, L., et al. 2003a, *ApJS*, 148, 39
- . 2003b, *ApJ*, 585, 566
- Peebles, P. J. E. 1968, *ApJ*, 153, 1
- . 1993, *Principles of Physical Cosmology* (Princeton, NJ: Princeton University Press)
- Peiris, H. 2003, *Ph.D. thesis*, Princeton University
- Peiris, H. V., et al. 2003, *ApJS*, 148, 213
- Penzias, A. A. & Wilson, R. W. 1965, *ApJ*, 142, 419
- Piacentini, F., et al. 2005, *ArXiv Astrophysics e-prints*
- Polnarev, A. G. 1985, *AZh*, 62, 1041
- Ponthieu, N. et al. 2005, *Astron. & Astro.*, 607, 655
- Pritchard, J. R. & Kamionkowski, M. 2005, *Annals Phys.*, 318, 2

- Prunet, S. & Lazarian, A. 1999, in *Microwave Foregrounds*. Sloan Summit, Institute for Advanced Study, Princeton, New Jersey 14-15 November 1998. Eds: A. Rde Oliveira-Costa and M. Tegmark., Vol. 181 (Astronomical Society of the Pacific), 113
- Readhead, A. C. S., et al. 2004, *ApJ*, 609, 498
- Readhead, A. C. S., et al. 2004, *Science*, 306, 761
- Rees, M. J. 1968, *ApJ*, 153, L1
- Reich, P. & Reich, W. 1988, *A&AS*, 74, 7
- Reid, M. & Brunthaler, A. 2005, in *Future Directions in High Resolution Astronomy: The 10th Anniversary of the VLBA*, ASP Conference Proceedings, Eds: J. Romney and M. Reid., Vol. 340 (Astronomical Society of the Pacific), 253
- Rybicki, G. B. & Lightman, A. 1979, *Radiative Processes in Astrophysics* (Wiley & Sons: New York)
- Sault, R. J., Hamaker, J. P., & Bregman, J. D. 1996, *A&AS*, 117, 149
- Seljak, U. 1997, *ApJ*, 482, 6
- Seljak, U. & Zaldarriaga, M. 1996, *ApJ*, 469, 437
- Sievers, J. L., et al. 2005, *ArXiv Astrophysics e-prints*
- Sironi, G., Boella, G., Bonelli, G., Brunetti, L., Cavaliere, F., Gervasi, M., Giardino, G., & Passerini, A. 1997, *New Astronomy*, 3, 1
- Slosar, A., Seljak, U., & Makarov, A. 2004, *Phys. Rev.*, D69, 123003
- Sofue, Y., Fujimoto, M., & Wielebinski, R. 1986, *ARA&A*, 24, 459
- Spergel, D. N. & Zaldarriaga, M. 1997, *Phys. Rev. Lett.*, 79, 2180
- Spergel, D. N., et al. 2003, *ApJS*, 148, 175
- Spergel, D. N. et al. 2006, *ApJ*, submitted
- Starobinsky, A. A. 1979, *ZhETF Pis ma Redaktsiiu*, 30, 719
- Steinhardt, P. J. & Turok, N. 2002, *Science*, 296, 1436
- Sukumar, S. & Allen, R. 1991, *ApJ*, 382, 100
- Tegmark, M., Eisenstein, D. J., Hu, W., & de Oliveira-Costa, A. 2000, *ApJ*, 530, 133, astro-ph/9905257
- Tinbergen, J. 1996, *Astronomical polarimetry* (Cambridge University Press)
- Torbet, E. et al. 1999, *ApJ*, 521, L79
- Tucci, M., Carretti, E., Cecchini, S., Nicastro, L., Fabbri, R., Gaensler, B. M., Dickey, J. M., & McClure-Griffiths, N. M. 2002, *ApJ*, 579, 607
- Turner, M. S. 1997, *Phys. Rev. D*, 55, 435
- Turner, M. S., White, M. J., & Lidsey, J. E. 1993, *Phys. Rev.*, D48, 4613
- Turok, N. 1996, *ApJ*, 473, L5
- Uyaniker, B., Fuerst, E., Reich, W., Reich, P., & Wielebinski, R. 1999, *Astron. Astrophys. Suppl. Ser.*, 138, 31
- Verde, L., Peiris, H., & Jimenez, R. 2006, *JCAP*, 019
- Verde, L., et al. 2003, *ApJS*, 148, 195
- Wang, Y. 1996, *Phys. Rev.*, D53, 639
- Watson, R. A., Rebolo, R., Rubiño-Martín, J. A., Hildebrandt, S., Gutiérrez, C. M., Fernández-Cerezo, S., Hoyland, R. J., & Battistelli, E. S. 2005, *ApJ*, 624, L89
- Weiss, R. 1984, *ARA&A*, 12, 90
- Wollack, E. B., Jarosik, N., Netterfield, C. B., Page, L., & Wilkinson, D. 1993, *ApJ*, 419, L49
- Wolleben, M., Landecker, T. L., Reich, W., & Wielebinski, R. 2005, *ArXiv Astrophysics e-prints*
- Wright, E. L., Hinshaw, G., & Bennett, C. L. 1996, *ApJ*, 458, L53
- Wright, M. C. H. & Forster, J. R. 1980, *ApJ*, 239, 873
- Zaldarriaga, M. & Harari, D. D. 1995, *Phys. Rev.*, D52, 3276
- Zaldarriaga, M. & Seljak, U. 1997, *Phys. Rev. D*, 55, 1830
- Zeldovich, Y. B., Kurt, V. G., & Syunyaev, R. A. 1969, *Journal of Experimental and Theoretical Physics*, 28, 146
- Zhang, Y., Yuan, Y., Zhao, W., & Chen, Y.-T. 2005, *Class. Quant. Grav.*, 22, 1383

APPENDIX

A. RADIOMETER MODEL

In this section we develop a simple model for the *WMAP* instrument using Jones matrices (Jones 1941; Montgomery et al. 1948; Blum 1959; Faris 1967; Sault et al. 1996; Tinbergen 1996; Hu et al. 2003). In the following we assume that all circuit elements are matched and ignore additive noise terms.

The Jones matrix \mathbf{J} models the instrumental response to polarization,

$$E_{\text{out}} = \mathbf{J} E_{\text{in}} \quad (\text{A1})$$

linearly relating the output electric field to the input. *WMAP* is a differential instrument, so the input radiation vector E_{in} has four elements, $(E_x^A, E_y^A, E_x^B, E_y^B)$, corresponding to the electric field seen by the A- and B-side feed pair. The outputs E_{out} are the inputs to the detectors.

The first link in the chain is to model the optics, feeds, and orthomode transducers (OMTs). We consider them as a single unit, because ascribing effects to the individual components is difficult and not well defined in terms of observations. We include two effects, loss imbalance and polarization leakage:

$$\mathbf{J}_{\text{OFO}}^{A,B} = \mathbf{J}_{\text{loss}}^{A,B} \mathbf{J}_{\text{crosspol}}^{A,B} \quad (\text{A2})$$

$$\mathbf{J}_{\text{loss}}^{A,B} = \begin{pmatrix} L_x^{A,B} & 0 \\ 0 & L_y^{A,B} \end{pmatrix} \quad (\text{A3})$$

$$\mathbf{J}_{\text{crosspol}}^{A,B} = \begin{pmatrix} 1 & X_1^{A,B} e^{iY_1^{A,B}} \\ -X_2^{A,B} e^{-iY_2^{A,B}} & 1 \end{pmatrix} \quad (\text{A4})$$

Here $L_{x,y}^{A,B}$ is the loss for the particular polarization and $X_{1,2}^{A,B}$ quantifies the level of cross-polarization (or polarization isolation) leakage, which we model as a small rotation error. The matrix $\mathbf{J}_{\text{crosspol}}^{A,B}$ is the first term in the expansion of a general unitary matrix but is not unitary itself. The subscripts “1” and “2” refer to the two orthogonally polarized radiometers which are differenced to form Δ_P . The matrix $\mathbf{J}_{\text{crosspol}}^{A,B}$ is the first term in the expansion of a general unitary matrix, though it is not unitary itself. The cross-polarization terms are allowed to have arbitrary phases $Y_{1,2}^{A,B}$. It is possible for cross polarization to produce circular polarization but *WMAP* cannot detect it in Δ_I or Δ_P . While in general there are four loss terms, two of them are calibrated out. The two that remain are the radiometer loss imbalances, $x_{\text{im},1}$ and $x_{\text{im},2}$. Jarosik et al. (2003b, Table 3) measured the loss imbalances by fitting the response to the common mode CMB dipole signal, and found them to be $\lesssim 1\%$. The mean imbalance, $\bar{x}_{\text{im}} = (x_{\text{im},1} + x_{\text{im},2})/2$, is corrected for by the map-making algorithm, while the “imbalance in the imbalance”, $\delta x_{\text{im}} = (x_{\text{im},1} - x_{\text{im},2})/2$, is not (Hinshaw et al. 2003a, §C.3). To connect the different notations, $L_x^A = L_1(1 + x_{\text{im},1})$, $L_y^A = L_2(1 + x_{\text{im},2})$, $L_x^B = L_2(1 - x_{\text{im},2})$, and $L_y^B = L_1(1 - x_{\text{im},1})$. The L_1 and L_2 are calibrated out.

The next step is to model the radiometers. They are described in detail in Jarosik et al. (2003a), so we simply present the Jones representation of the radiometer and refer the reader to the paper for more details.

$$\mathbf{J}_{\text{radiometer}} = \mathbf{J}_{\text{warmT}} \mathbf{J}_{\text{switch}} \mathbf{J}_{\text{amp}} \mathbf{J}_{\text{coldT}} \quad (\text{A5})$$

$$\mathbf{J}_{\text{coldT}} = \frac{1}{\sqrt{2}} \begin{pmatrix} 1 & 1 \\ 1 & -1 \end{pmatrix} \quad (\text{A6})$$

$$\mathbf{J}_{\text{amp}} = \begin{pmatrix} g_s & 0 \\ 0 & g_d \end{pmatrix} \quad (\text{A7})$$

$$\mathbf{J}_{\text{switch}} = \begin{pmatrix} 1 & 0 \\ 0 & e^{i\phi} \end{pmatrix} \quad (\text{A8})$$

$$\mathbf{J}_{\text{warmT}} = \frac{1}{\sqrt{2}} \begin{pmatrix} 1 & 1 \\ 1 & -1 \end{pmatrix} \quad (\text{A9})$$

Here, g_s, g_d are the amplifier gains in the two legs of the radiometer, and ϕ is the instantaneous phase of the (unjammed) phase switch. We have lumped the warm and cold amplifiers together.

$$\mathbf{J}_{\text{DA}} = \mathbf{J}_{\text{bandpass}} \mathbf{J}_{\text{radiometer}} \mathbf{M}_{\text{connect}} \mathbf{J}_{\text{OFO}} \quad (\text{A10})$$

$$\mathbf{M}_{\text{connect}} = \begin{pmatrix} 1 & 0 & 0 & 0 \\ 0 & 0 & 0 & 1 \\ 0 & 1 & 0 & 0 \\ 0 & 0 & 1 & 0 \end{pmatrix} \quad (\text{A11})$$

$$\mathbf{J}_{\text{radiometer}} = \begin{pmatrix} \mathbf{J}_{\text{radiometer}}^{(1)} & \mathbf{0} \\ \mathbf{0} & \mathbf{J}_{\text{radiometer}}^{(2)} \end{pmatrix} \quad (\text{A12})$$

$$\mathbf{J}_{\text{bandpass}} = \begin{pmatrix} f_{13}(\omega) & 0 & 0 & 0 \\ 0 & f_{14}(\omega) & 0 & 0 \\ 0 & 0 & f_{23}(\omega) & 0 \\ 0 & 0 & 0 & f_{24}(\omega) \end{pmatrix} \quad (\text{A13})$$

The detector outputs in counts ($c_{13}, c_{14}, c_{23}, c_{24}$) are the diagonal elements of $\mathbf{P}_{\text{out}} = \langle E_{\text{out}} E_{\text{out}}^\dagger \rangle$, multiplied by the responsivities ($s_{13}, s_{14}, s_{23}, s_{24}$). \mathbf{J}_{OFO} is a 4x4 matrix with $\mathbf{J}_{\text{OFO}}^A$ (Equation A2) filling the upper left 2x2 entries and $\mathbf{J}_{\text{OFO}}^B$ filling the lower right 2x2 entries.

$$\mathbf{P}_{\text{out}} = \mathbf{J}_{\text{DA}} \mathbf{P}_{\text{in}} \mathbf{J}_{\text{DA}}^\dagger \quad (\text{A14})$$

$$\mathbf{P}_{\text{in}} = \begin{pmatrix} \mathbf{P}_{\text{in}}^A & 0 \\ 0 & \mathbf{P}_{\text{in}}^B \end{pmatrix} \quad (\text{A15})$$

$$\mathbf{P}_{\text{in}}^X = \begin{pmatrix} T^X + Q^X & U^X - iV^X \\ U^X + iV^X & T^X - Q^X \end{pmatrix}. \quad (\text{A16})$$

In this expression, Stokes Q , U , and V refer to the quantities measured in the radiometer reference frame; we drop the ‘‘Rad’’ notation used in §3 for notational convenience. Before the outputs are recorded they are demodulated in phase with the phase switch. We model this process as

$$c_{ij} \rightarrow \frac{1}{2} [c_{ij}(\phi_i) - c_{ij}(\phi_i + \pi - \delta_i)] \quad (\text{A17})$$

where ϕ_i is the phase difference between the two radiometer legs, and δ_i is the error between the two switch states.

Since the input radiation is incoherent,

$$\mathbf{P}_{\text{out}} = \int d\omega \frac{\partial \mathbf{P}_{\text{out}}}{\partial \omega}. \quad (\text{A18})$$

Since $\mathbf{J}_{\text{bandpass}}$ is the only frequency dependent component in the model, we make the substitution $f_{ij}^2(\omega) \rightarrow \tilde{f}_{ij}^2$, where

$$\tilde{f}_{ij}^2 = \int d\omega f_{ij}^2(\omega). \quad (\text{A19})$$

The calibrated detector outputs are $d_{ij} = c_{ij}/G_{ij}$, where G_{ij} is a gain for the temperature difference,

$$G_{ij} = \frac{1}{2} L_i g_{is} g_{id} \tilde{f}_{ij}^2 s_{ij} \cos(\delta_i/2) \cos(\phi_i - \delta_i/2) (1 - \epsilon_{ij}). \quad (\text{A20})$$

Here ϵ_{ij} is the calibration uncertainty.

The radiometer signal channels are $\Delta T_i = (d_{i3} - d_{i4})/2$, from which are formed the temperature and polarization signal channels $\Delta T_i, \Delta T_P$. Then to first order in the systematic uncertainties,

$$\Delta T_i = 2 \delta x_{\text{im}} Q^- + \epsilon^- Q^+ + (1 + \epsilon^+) T^- + 2 \bar{x}_{\text{im}} T^+ + Z_-^A U^A - Z_-^B U^B \quad (\text{A21})$$

$$\Delta T_P = 2 \bar{x}_{\text{im}} Q^- + (1 + \epsilon^+) Q^+ + \epsilon^- T^- + 2 \delta x_{\text{im}} T^+ + Z_+^A U^A + Z_+^B U^B \quad (\text{A22})$$

Here $T^\pm \equiv T^A \pm T^B$, $\{Q^\pm, U^\pm, L^\pm\}$ are similarly defined, $Z_\pm^{A,B} = X_1^{A,B} \cos(Y_1^{A,B}) \pm X_2^{A,B} \cos(Y_2^{A,B})$ encodes the influence of the crosspol effects, and $\epsilon^\pm \equiv ((\epsilon_{13} + \epsilon_{14}) \pm (\epsilon_{23} + \epsilon_{24}))/4$. The dominant ΔT_P component is Q^+ , not Q^- , because $Q^A \rightarrow -Q^B, Q^B \rightarrow -Q^A$ when the spacecraft rotates 180°. In the limit of no loss imbalance or calibration error, and similar cross polarization for all components, $\Delta T_P = Q^+ + 2X \cos(Y) U^+$.

B. ESTIMATION OF THE POLARIZATION POWER SPECTRA

The WMAP polarization power spectra at $l < 32$ incorporate an extension of the MASTER quadratic estimator (Hivon et al. 2002), which is used to account for mode coupling. The original method assumes that observations of every point on the sky give statistically independent noise. However, WMAP has a significant component of the noise that is correlated between pointings due to its scan pattern and the $1/f$ noise, and thus the method needs to be modified as described here to accommodate a full covariance matrix. The most conspicuous mathematical feature of the original method is Wigner 3- j symbols, whereas in the extended method, these objects are not used. For more details of the original method, as well as the application to polarization, see Appendix A of Kogut et al. (2003), together with the references therein.

B.1. Extended MASTER Algorithm for Temperature Power Spectrum

The original method is derived by modeling the sky brightness as a continuous function of pointing. For example, the observed cut-sky spherical harmonic coefficients for Stokes I , denoted as \tilde{T}_{lm} , are defined as follows:

$$\tilde{T}_{lm} = \int d\hat{n} w(\hat{n}) T(\hat{n}) Y_{lm}^*(\hat{n}). \quad (B1)$$

Here, \hat{n} is the unit vector of the pointing, $w(\hat{n})$ is the weighting function, $T(\hat{n})$ is the sky brightness, and $Y_{lm}(\hat{n})$ is a spherical harmonic basis function. Expanding $T(\hat{n})$ and $w(\hat{n})$ in spherical harmonics gives a series. Each term of the series includes an integral of a product of three spherical harmonic basis functions:

$$\tilde{T}_{lm} = \sum_{l'm'} \sum_{l''m''} w_{l''m''} T_{l'm'} \int d\hat{n} Y_{l'm'}(\hat{n}) Y_{l''m''}(\hat{n}) Y_{lm}^*(\hat{n}).$$

These distinctive integrals are what give rise to the 3- j symbols. The orthogonality relations of 3- j symbols eliminate many terms in the expression for the observed power spectrum.

When there is noise covariance, the weight is a function of two pointings rather than just one, and the 3- j symbols are not used. This case is most easily treated by modeling the sky as a set of discrete pixels. The goal of the derivation is to form a mode-coupling matrix $M_{ll'}^{XY, X'Y'}$, where XY and $X'Y'$ are each chosen from the nine correlations TT , TE , TB , ET , EE , EB , BT , BE , and BB . In order to introduce the formalism, we first discuss the TT correlation, which is the simplest. Because there is no coupling between TT and the other eight correlations, only $M_{ll'}^{TT, TT}$ needs to be considered. We note here that we do not actually use this formalism for TT but only for the others, as the temperature power spectrum at low- l is dominated by the signal and the noise correlation is not important. We use TT here to illustrate the main point of the method. The extension to the polarization power spectra that follows TT (§ B.2) is what we use for the actual analysis.

The weighting is computed initially as the inverse of the covariance matrix of the pixels. The sky cut is expressed by setting the appropriate rows and columns to a very large number in the noise covariance matrix before inverting it [Eq. (D7)]. We call the resulting weight matrix W . Further, let $Y_{lm,p}$ be a matrix containing (appropriately normalized) values of a spherical harmonic basis function evaluated at each pixel, p , index lm . The number of rows of $Y_{lm,p}$ is n_p , which is the number of pixels in each sky map. The observed Stokes I sky map is T_p .

In this notation, the observed spherical harmonic coefficients are expressed as

$$\tilde{T}_{lm} = \sum_{pp'} Y_{lm,p}^* W_{pp'} T_{p'}.$$

If the matrix W is diagonal, this expression is simply the discrete version of Eq. B1 above. Expanding $T_{p'}$ in spherical harmonics gives

$$\tilde{T}_{lm} = \sum_{l'm'} \left[\sum_{pp'} Y_{lm,p}^* W_{pp'} Y_{l'm',p'} \right] T_{l'm'}.$$

This expression suggests the utility of defining

$$Z_{lm,l'm'} \equiv \sum_{pp'} Y_{lm,p}^* W_{pp'} Y_{l'm',p'} \quad (B2)$$

so that

$$\tilde{T}_{lm} = \sum_{l'm'} Z_{lm,l'm'} T_{l'm'}.$$

The value of the observed power spectrum at l is expressed as follows:

$$\begin{aligned} (2l+1)\tilde{C}_l &= \sum_m \tilde{T}_{lm}^* \tilde{T}_{lm} \\ &= \sum_m \sum_{l''m''} \sum_{l'm'} (Z_{lm,l''m''} T_{l''m''})^* Z_{lm,l'm'} T_{l'm'}. \end{aligned} \quad (B3)$$

In order to get the true, underlying CMB power spectrum into the equation, the next step is to take the expectation of Eq. B3:

$$\begin{aligned}
 (2l+1)\langle\tilde{C}_l\rangle &= \sum_{l''m''} \sum_{l'm'} \sum_m Z_{lm,l''m''}^* Z_{lm,l'm'} \langle T_{l''m''}^* T_{l'm'} \rangle \\
 &= \sum_{l''m''} \sum_{l'm'} \sum_m Z_{lm,l''m''}^* Z_{lm,l'm'} \langle C_{l'} \rangle \delta_{l'l''} \delta_{m'm''} \\
 &= \sum_{l'} \left(\sum_{mm'} Z_{lm,l'm'}^* Z_{lm,l'm'} \right) \langle C_{l'} \rangle.
 \end{aligned} \tag{B4}$$

Therefore, we obtain the unbiased estimator of the underlying power spectrum as

$$C_l = \sum_{l'} (M^{-1})_{ll'} \tilde{C}_{l'}, \tag{B5}$$

where

$$M_{ll'} \equiv \frac{1}{2l+1} \sum_{mm'} |Z_{lm,l'm'}|^2. \tag{B6}$$

In order to apply this method to cross-correlations between DAs, one of the Z matrices in Eq. B6 is computed from the noise matrix of the first DA, and the other from that of the second DA.

B.2. Extended MASTER Algorithm for Polarization Power Spectra

The same formalism accommodates polarization. In what follows, uppercase X or Y indicates one of the three harmonic transforms T , E , or B , and lowercase a or b denotes the Stokes parameter label I , Q , or U . The following substitutions are made in the above derivation:

$$W_{pp'} \rightarrow W_{(ap)(a'p')} \tag{B7}$$

$$Y_{lm,p} \rightarrow \Upsilon_{(Xlm)(ap)} \tag{B8}$$

where the non-zero elements of Υ are

$$\Upsilon_{(Tlm)(Ip)} = Y_{lm,p} \tag{B9}$$

$$\Upsilon_{(Elm)(Qp)} = -\frac{1}{2} (+2Y_{lm,p} - 2Y_{lm,p}) \tag{B10}$$

$$\Upsilon_{(Blm)(Qp)} = -\frac{i}{2} (+2Y_{lm,p} - 2Y_{lm,p}) \tag{B11}$$

$$\Upsilon_{(Elm)(Up)} = -\Upsilon_{(Blm)(Qp)} \tag{B12}$$

$$\Upsilon_{(Blm)(Up)} = \Upsilon_{(Elm)(Qp)} \tag{B13}$$

$\pm 2Y_{lm,p}$ are spin-2 spherical harmonics in the same matrix form as $Y_{lm,p}$.

For each pair of DAs, a Z matrix is computed by analogy with Eq. B2. The derivation follows the general steps above. The analog of Eq. B5 is

$$C_l^{XY} = \sum_{X'Y'l'} (M^{-1})_{ll'}^{XY,X'Y'} \tilde{C}_{l'}^{X'Y'}, \tag{B14}$$

where

$$M_{ll'}^{XY,X'Y'} = \frac{1}{2l+1} \sum_{mm'} Z_{lm,l'm'}^{XX'*} Z_{lm,l'm'}^{YY'},$$

where

$$Z_{lm,l'm'}^{XX'} \equiv \sum_{ap,a'p'} \Upsilon_{(Xlm)(ap)}^* W_{(ap)(a'p')} \Upsilon_{(X'l'm')(a'p')} \tag{B15}$$

For each DA pair, the 81 coupling submatrices $M_{ll'}^{XY,X'Y'}$ are combined in a grand coupling matrix that takes into account all the coupling among the nine correlation types.

B.3. Analytical Approximation

The expressions for the coupling matrices greatly simplify when $W_{pp'}$ is diagonal in pixel space, $W_{pp'} = \delta_{pp'} N_{obs,p}$. This limit is a good approximation to the WMAP data at high l , where noise is approximately uncorrelated (diagonal in pixel space). In this limit, one can evaluate the coupling matrices analytically.

It is convenient to write the N_{obs} matrix as

$$\begin{pmatrix} N_{obs,p}^{QQ} & N_{obs,p}^{QU} \\ N_{obs,p}^{UQ} & N_{obs,p}^{UU} \end{pmatrix} = \begin{pmatrix} N_{obs,p}^+ + N_{obs,p}^- & N_{obs,p}^{QU} \\ N_{obs,p}^{UQ} & N_{obs,p}^+ - N_{obs,p}^- \end{pmatrix}, \tag{B16}$$

where

$$N_{obs,p}^+ \equiv \frac{N_{obs,p}^{QQ} + N_{obs,p}^{UU}}{2}, \quad (B17)$$

$$N_{obs,p}^- \equiv \frac{N_{obs,p}^{QQ} - N_{obs,p}^{UU}}{2}. \quad (B18)$$

One can show that under a rotation of basis by an angle θ , these quantities transform as

$$N_{obs,p}^+ \rightarrow N_{obs,p}^+, \quad (B19)$$

$$N_{obs,p}^- \pm iN_{obs,p}^{QU} \rightarrow e^{\mp 4i\theta} (N_{obs,p}^- \pm iN_{obs,p}^{QU}). \quad (B20)$$

Therefore, we expand them into spin harmonics as follows:

$$N_{obs,p}^+ = \sum_{lm} n_{lm}^+ Y_{lm,p}, \quad (B21)$$

$$N_{obs,p}^- \pm iN_{obs,p}^{QU} = \sum_{lm} \mp 4n_{lm} \mp 4Y_{lm,p}. \quad (B22)$$

We obtain

$$\begin{aligned} Z_{lm,l'm'}^{EE} = & \frac{1}{2} \sum_{LM} I_{lm,l'm'}^{LM} \left\{ n_{LM}^+ \left[1 + (-)^{L+l+l'} \right] \begin{pmatrix} L & l & l' \\ 0 & 2 & -2 \end{pmatrix} \right. \\ & \left. + \left[{}_4n_{LM} + (-)^{L+l+l'} {}_{-4}n_{LM} \right] \begin{pmatrix} L & l & l' \\ -4 & 2 & 2 \end{pmatrix} \right\}, \end{aligned} \quad (B23)$$

$$\begin{aligned} Z_{lm,l'm'}^{BB} = & \frac{1}{2} \sum_{LM} I_{lm,l'm'}^{LM} \left\{ n_{LM}^+ \left[1 + (-)^{L+l+l'} \right] \begin{pmatrix} L & l & l' \\ 0 & 2 & -2 \end{pmatrix} \right. \\ & \left. - \left[{}_4n_{LM} + (-)^{L+l+l'} {}_{-4}n_{LM} \right] \begin{pmatrix} L & l & l' \\ -4 & 2 & 2 \end{pmatrix} \right\}, \end{aligned} \quad (B24)$$

$$\begin{aligned} Z_{lm,l'm'}^{EB} = & \frac{i}{2} \sum_{LM} I_{lm,l'm'}^{LM} \left\{ n_{LM}^+ \left[1 - (-)^{L+l+l'} \right] \begin{pmatrix} L & l & l' \\ 0 & 2 & -2 \end{pmatrix} \right. \\ & \left. - \left[{}_4n_{LM} - (-)^{L+l+l'} {}_{-4}n_{LM} \right] \begin{pmatrix} L & l & l' \\ -4 & 2 & 2 \end{pmatrix} \right\}, \end{aligned} \quad (B25)$$

where

$$I_{lm,l'm'}^{LM} \equiv (-)^m \sqrt{\frac{(2L+1)(2l+1)(2l'+1)}{4\pi}} \begin{pmatrix} L & l & l' \\ M & -m & m' \end{pmatrix}. \quad (B26)$$

Using the identity

$$\sum_{mm'} I_{lm,l'm'}^{LM} I_{lm,l'm'}^{L'M'} = \frac{(2l+1)(2l'+1)}{4\pi} \delta_{LL'} \delta_{MM'}, \quad (B27)$$

it is straightforward to evaluate all the relevant coupling matrices analytically:

$$\begin{aligned} M_{ll'}^{EE,EE} = & \frac{1}{2l+1} \sum_{mm'} |Z_{lm,l'm'}^{EE}|^2 \\ = & \frac{2l'+1}{16\pi} \sum_{LM} \left| n_{LM}^+ \left[1 + (-)^{L+l+l'} \right] \begin{pmatrix} L & l & l' \\ 0 & 2 & -2 \end{pmatrix} \right. \\ & \left. + \left[{}_4n_{LM} + (-)^{L+l+l'} {}_{-4}n_{LM} \right] \begin{pmatrix} L & l & l' \\ -4 & 2 & 2 \end{pmatrix} \right|^2, \end{aligned} \quad (B28)$$

$$\begin{aligned} M_{ll'}^{BB,BB} = & \frac{1}{2l+1} \sum_{mm'} |Z_{lm,l'm'}^{BB}|^2 \\ = & \frac{2l'+1}{16\pi} \sum_{LM} \left| n_{LM}^+ \left[1 + (-)^{L+l+l'} \right] \begin{pmatrix} L & l & l' \\ 0 & 2 & -2 \end{pmatrix} \right. \\ & \left. - \left[{}_4n_{LM} + (-)^{L+l+l'} {}_{-4}n_{LM} \right] \begin{pmatrix} L & l & l' \\ -4 & 2 & 2 \end{pmatrix} \right|^2, \end{aligned} \quad (B29)$$

$$\begin{aligned}
M_{ll'}^{EE,BB} &= \frac{1}{2l+1} \sum_{mm'} |Z_{lm,l'm'}^{EB}|^2 \\
&= \frac{2l'+1}{16\pi} \sum_{LM} \left| n_{LM}^+ \left[1 - (-)^{L+l+l'} \right] \begin{pmatrix} L & l & l' \\ 0 & 2 & -2 \end{pmatrix} \right. \\
&\quad \left. - \left[4n_{LM} - (-)^{L+l+l'} - 4n_{LM} \right] \begin{pmatrix} L & l & l' \\ -4 & 2 & 2 \end{pmatrix} \right|^2,
\end{aligned} \tag{B30}$$

$$\begin{aligned}
M_{ll'}^{EB,EB} &= \frac{1}{2l+1} \sum_{mm'} Z_{lm,l'm'}^{EE*} Z_{lm,l'm'}^{BB} \\
&= \frac{2l'+1}{16\pi} \sum_{LM} \left\{ \left| n_{LM}^+ \left[1 + (-)^{L+l+l'} \right] \begin{pmatrix} L & l & l' \\ 0 & 2 & -2 \end{pmatrix} \right|^2 \right. \\
&\quad \left. - \left| \left[4n_{LM} + (-)^{L+l+l'} - 4n_{LM} \right] \begin{pmatrix} L & l & l' \\ -4 & 2 & 2 \end{pmatrix} \right|^2 \right\}.
\end{aligned} \tag{B31}$$

C. POLARIZATION FISHER AND COVARIANCE MATRIX

In this Appendix, we derive expressions for the Fisher and covariance matrices of the temperature and polarization power spectra. Our derivation extends the derivation of the TT matrices given in Hinshaw et al. (2003b) to all combinations of polarization power spectra.

Note that we do *not* use these results for evaluating the likelihood that is used in the cosmological analysis. At low multipoles, $l \leq 23$, we evaluate the likelihood of polarization data directly from the maps using the exact method described in Appendix D. Why do we not use the Fisher or covariance matrix for the cosmological analysis, except for TT and TE spectra at $\ell > 23$? The reason is because the form of the likelihood function for the power spectra is not a Gaussian at low multipoles, and therefore the Fisher or covariance matrix, which only characterize the second-order moment of the power spectrum, is not sufficient to fully specify the likelihood function. This was pointed out after the first year release by Efstathiou (2004) and Slosar et al. (2004) and is discussed in Hinshaw et al. (2006). As we do not know the precise form of the likelihood for the power spectra, we evaluate the likelihood of the temperature and polarization maps directly, which is a Gaussian, at low multipoles, $l \leq 23$. For high multipoles, $l > 23$, the likelihood function may be approximated as a Gaussian and therefore we use a Gaussian likelihood with the Fisher or covariance matrices. While we do not use the EE or BB power spectra at $l > 23$, as they contain very little signal compared to noise, we do use the covariance matrix of the TE power spectrum at $l > 23$ in the likelihood code, for which we adopt the analytical *ansatz* given in Equation C12, which was also used in the first-year analysis of the TE power spectrum (Kogut et al. 2003). For the evaluation of the TT likelihood, see Hinshaw et al. (2006).

C.1. Fisher Matrix: Exact formula

The Fisher matrix, $F_{ll'}$, is given by

$$F_{ll'}^{XY,X'Y'} = \frac{1}{2} \sum_q \left[\sum_{q_1} (C^{-1})_{qq_1} \frac{\partial C_{q_1 q_2}}{\partial S_l^{XY}} (C^{-1})_{q_2 q_3} \frac{\partial C_{q_3 q}}{\partial S_{l'}^{X'Y'}} \right], \tag{C1}$$

where the covariance matrix $C_{qq'}$ consists of the covariance matrices of all the bilinear combinations of T , Q , and U :

$$C_{qq'} = \begin{pmatrix} C_{pp'}^{TT} & C_{pp'}^{TQ} & C_{pp'}^{TU} \\ C_{pp'}^{QT} & C_{pp'}^{QQ} & C_{pp'}^{QU} \\ C_{pp'}^{UT} & C_{pp'}^{UQ} & C_{pp'}^{UU} \end{pmatrix}, \tag{C2}$$

and the covariance includes the signal and noise, $C_{qq'} = S_{qq'} + N_{qq'}$. Here S_l^{XY} is the angular (cross) power spectrum of the signal where X and Y denote T , E , or B . The inverse covariance matrix in harmonic space is then given by the harmonic transform of $(C^{-1})_{qq'}$:

$$(C^{-1})_{lm,l'm'}^{XY} = \sum_{ap,a'p'} \Upsilon_{(Xlm)(ap)} (C^{-1})_{ap,a'p'} \Upsilon_{(Y^*l'm')(a'p')}, \tag{C3}$$

where Υ is given by the equations following (B8).

Using these quantities, each term of the Fisher matrix (Eq. [C1]) evaluates to

$$F_{ll'}^{XX,XX} = \frac{1}{2} \sum_{mm'} [(C^{-1})_{lm,l'm'}^{XX}]^2, \tag{C4}$$

$$F_{ll'}^{XX,XY} = \sum_{mm'} [(C^{-1})_{lm,l'm'}^{XX} (C^{-1})_{lm,l'm'}^{XY}], \tag{C5}$$

$$F_{ll'}^{XX,YY} = \frac{1}{2} \sum_{mm'} [(C^{-1})_{lm,l'm'}^{XY}]^2, \tag{C6}$$

$$F_{ll'}^{XY,XY} = \sum_{mm'} [(C^{-1})_{lm,l'm'}^{XY}]^2 + \sum_{mm'} [(C^{-1})_{lm,l'm'}^{XX} (C^{-1})_{lm,l'm'}^{YY}] , \quad (C7)$$

where $X \neq Y$. In general cases where $S_{qq'}$ or $N_{qq'}$ (or both) are non-diagonal, one must calculate $(C^{-1})_{qq'}$ by directly inverting the covariance matrix given by equation (C2). In reality, however, the matrix inversion requires n_p^3 operations and thus it become computationally too expensive to evaluate for the full WMAP resolution. On the other hand, if one considers only large scale anisotropies at low l , then the matrix inversion can be done in a reasonable computational time. We use Eq. (C4)–(C7) for computing the Fisher matrices for C_l^{TT} , C_l^{TE} , C_l^{TB} , C_l^{EE} , C_l^{EB} , and C_l^{BB} , at low multipoles, $l \leq 32$.

C.2. Fisher Matrix: Analytical Approximation

The expressions for the Fisher matrices can be evaluated analytically when $C_{qq'}$ is diagonal in pixel space. This limit is a good approximation to the WMAP data at high l , where $C_{qq'}$ is dominated by noise and noise is approximately uncorrelated (diagonal in pixel space). In this limit, one obtains the following analytical formulae:

$$\begin{aligned} F_{ll'}^{EE,EE} &= \frac{1}{2} \sum_{mm'} |(N^{-1})_{lm,l'm'}^{EE}|^2 \\ &= \frac{(2l+1)(2l'+1)}{32\pi} \sum_{LM} \left| n_{LM}^+ \left[1 + (-)^{L+l+l'} \right] \begin{pmatrix} L & l & l' \\ 0 & 2 & -2 \end{pmatrix} \right. \\ &\quad \left. + \left[4n_{LM} + (-)^{L+l+l'} - 4n_{LM} \right] \begin{pmatrix} L & l & l' \\ -4 & 2 & 2 \end{pmatrix} \right|^2 , \end{aligned} \quad (C8)$$

$$\begin{aligned} F_{ll'}^{BB,BB} &= \frac{1}{2} \sum_{mm'} |(N^{-1})_{lm,l'm'}^{BB}|^2 \\ &= \frac{(2l+1)(2l'+1)}{32\pi} \sum_{LM} \left| n_{LM}^+ \left[1 + (-)^{L+l+l'} \right] \begin{pmatrix} L & l & l' \\ 0 & 2 & -2 \end{pmatrix} \right. \\ &\quad \left. - \left[4n_{LM} + (-)^{L+l+l'} - 4n_{LM} \right] \begin{pmatrix} L & l & l' \\ -4 & 2 & 2 \end{pmatrix} \right|^2 , \end{aligned} \quad (C9)$$

$$\begin{aligned} F_{ll'}^{EE,BB} &= \frac{1}{2} \sum_{mm'} |(N^{-1})_{lm,l'm'}^{EB}|^2 \\ &= \frac{(2l+1)(2l'+1)}{32\pi} \sum_{LM} \left| n_{LM}^+ \left[1 - (-)^{L+l+l'} \right] \begin{pmatrix} L & l & l' \\ 0 & 2 & -2 \end{pmatrix} \right. \\ &\quad \left. - \left[4n_{LM} - (-)^{L+l+l'} - 4n_{LM} \right] \begin{pmatrix} L & l & l' \\ -4 & 2 & 2 \end{pmatrix} \right|^2 , \end{aligned} \quad (C10)$$

$$\begin{aligned} M_{ll'}^{EB,EB} &= \sum_{mm'} |(N^{-1})_{lm,l'm'}^{EB}|^2 + \sum_{mm'} (N^{-1})_{lm,l'm'}^{EE*} (N^{-1})_{lm,l'm'}^{BB} \\ &= \frac{(2l+1)(2l'+1)}{32\pi} \sum_{LM} \left\{ \left| n_{LM}^+ \left[1 - (-)^{L+l+l'} \right] \begin{pmatrix} L & l & l' \\ 0 & 2 & -2 \end{pmatrix} \right. \right. \\ &\quad \left. \left. - \left[4n_{LM} - (-)^{L+l+l'} - 4n_{LM} \right] \begin{pmatrix} L & l & l' \\ -4 & 2 & 2 \end{pmatrix} \right|^2 \right. \\ &\quad \left. + \left| n_{LM}^+ \left[1 + (-)^{L+l+l'} \right] \begin{pmatrix} L & l & l' \\ 0 & 2 & -2 \end{pmatrix} \right|^2 \right. \\ &\quad \left. - \left| \left[4n_{LM} + (-)^{L+l+l'} - 4n_{LM} \right] \begin{pmatrix} L & l & l' \\ -4 & 2 & 2 \end{pmatrix} \right|^2 \right\} . \end{aligned} \quad (C11)$$

C.3. Covariance Matrix: Ansatz

The inverse of the Fisher matrix gives the covariance matrix, Σ . While we use the map-based exact likelihood described in Appendix D for the cosmological analysis, it is still useful to have an approximate method to evaluate the likelihood of the data given theory and noise model from the power spectra. For this purpose, we use the following *ansatz*:

$$\Sigma_\ell^{TE TE} = \frac{\left(S_\ell^{TT} + n_{eff\ell}^{TT} \right) \left(S_\ell^{EE} + n_{eff\ell}^{EE} \right) + \left(S_\ell^{TE} \right)^2}{(2\ell+1) \left[f_{sky\ell}^{TE} \right]^2} \quad (C12)$$

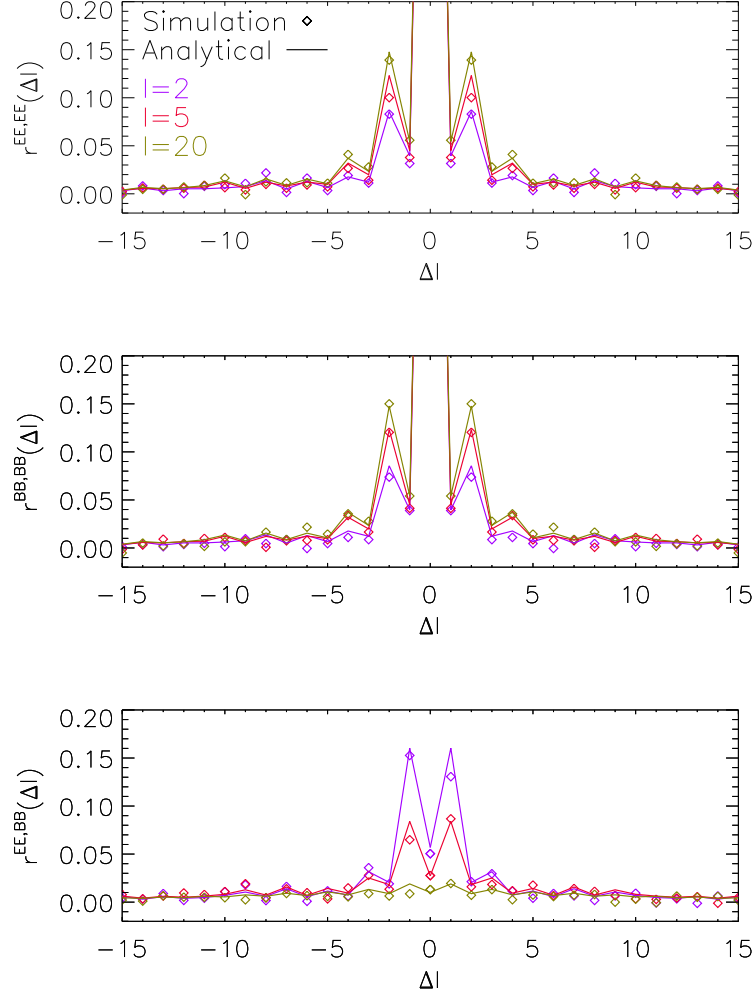


FIG. C28.— The correlation coefficients of the Fisher matrices. The diamonds are derived from 100,000 Monte Carlo simulations, while the solid lines are the analytical formulae in the noise-dominated regime. In the simulations, the B -mode is noise only while the E -mode has some signals at low l from reionization.

$$\Sigma_{\ell}^{TBTB} = \frac{\left(S_{\ell}^{TT} + n_{eff\ell}^{TT}\right) \left(S_{\ell}^{BB} + n_{eff\ell}^{BB}\right)}{(2\ell+1) \left[f_{sky\,eff}^{TB}(\ell)\right]^2} \quad (C13)$$

$$\Sigma_{\ell}^{EEEE} = \frac{2 \left(S_{\ell}^{EE} + n_{eff\ell}^{EE}\right)^2}{(2\ell+1) \left[f_{sky\,eff}^{EE}(\ell)\right]^2} \quad (C14)$$

$$\Sigma_{\ell}^{BBBB} = \frac{2 \left(S_{\ell}^{BB} + n_{eff\ell}^{BB}\right)^2}{(2\ell+1) \left[f_{sky\,eff}^{BB}(\ell)\right]^2} \quad (C15)$$

$$\Sigma_{\ell}^{EBEB} = \frac{\left(S_{\ell}^{EE} + n_{eff\ell}^{EE}\right) \left(S_{\ell}^{BB} + n_{eff\ell}^{BB}\right)}{(2\ell+1) \left[f_{sky\,eff}^{EB}(\ell)\right]^2} \quad (C16)$$

In these expressions $n_{eff\ell}$ denotes the effective noise as a function of ℓ and $f_{sky\,eff}$ denotes the effective fraction of the sky observed. These are obtained from comparing the *ansatz* to the inverse of the Fisher matrices derived in the previous sections.

We have found that $f_{\text{sky}}^{XY} \simeq \sqrt{f_{\text{sky}}^{XX} f_{\text{sky}}^{YY}}$ to a very good approximation. See also Kogut et al. (2003) for the evaluation of $\Sigma_\ell^{TE TE}$ and Hinshaw et al. (2006) for the evaluation of $\Sigma_\ell^{TT TT}$.

D. EXACT LIKELIHOOD EVALUATION AT LOW MULTIPOLES

At low multipoles, $l \leq 23$, we evaluate the likelihood of the data for a given theoretical model exactly from the temperature and polarization maps. The standard likelihood is given by

$$L(\vec{m}|S)d\vec{m} = \frac{\exp\left[-\frac{1}{2}\vec{m}'(S+N)^{-1}\vec{m}\right]}{|S+N|^{1/2}} \frac{d\vec{m}}{(2\pi)^{3n_p/2}}, \quad (\text{D1})$$

where \vec{m} is the data vector containing the temperature map, \vec{T} , as well as the polarization maps, \vec{Q} , and \vec{U} , n_p is the number of pixels of each map, and S and N are the signal and noise covariance matrix ($3n_p \times 3n_p$), respectively. As the temperature data are completely dominated by the signal at such low multipoles, noise in temperature may be ignored. This simplifies the form of likelihood as

$$L(\vec{m}|S)d\vec{m} = \frac{\exp\left[-\frac{1}{2}\vec{m}'(\tilde{S}_P+N_P)^{-1}\vec{m}\right]}{|\tilde{S}_P+N_P|^{1/2}} \frac{d\vec{m}}{(2\pi)^{n_p}} \frac{\exp\left(-\frac{1}{2}\vec{T}'S_T^{-1}\vec{T}\right)}{|S_T|^{1/2}} \frac{d\vec{T}}{(2\pi)^{n_p/2}}, \quad (\text{D2})$$

where S_T is the temperature signal matrix ($n_p \times n_p$), the new polarization data vector, $\vec{m} = (\tilde{Q}_p, \tilde{U}_p)$, is given by

$$\tilde{Q}_p \equiv Q_p - \frac{1}{2} \sum_{l=2}^{23} \frac{S_l^{TE}}{S_l^{TT}} \sum_{m=-l}^l T_{lm} (+2Y_{lm,p} + {}_{-2}Y_{lm,p}^*), \quad (\text{D3})$$

$$\tilde{U}_p \equiv U_p - \frac{i}{2} \sum_{l=2}^{23} \frac{S_l^{TE}}{S_l^{TT}} \sum_{m=-l}^l T_{lm} (+2Y_{lm,p} - {}_{-2}Y_{lm,p}^*), \quad (\text{D4})$$

and \tilde{S}_P is the signal matrix for the new polarization vector with the size of $2n_p \times 2n_p$. As T_{lm} is totally signal dominated, the noise matrix for (\tilde{Q}, \tilde{U}) equals that for (Q, U) , n_p . To estimate T_{lm} , we used the full-sky internal linear combination (ILC) temperature map (Hinshaw et al. 2006).

One can show that equation (D1) and (D2) are mathematically equivalent when the temperature noise is ignored. The new form, equation (D2), allows us to factorize the likelihood of temperature and polarization, with the information in their cross-correlation, S_l^{TE} , fully retained. We further rewrite the polarization part of the likelihood as

$$L(\vec{m}|\tilde{S}) = \frac{\exp\left[-\frac{1}{2}(N_P^{-1}\vec{m})'(\tilde{S}_P N_P^{-1} + N_P^{-1})^{-1}(N_P^{-1}\vec{m})\right]}{|N_P^{-1}\tilde{S}_P N_P^{-1} + N_P^{-1}|^{1/2}} \frac{|N_P^{-1}|d\vec{m}}{(2\pi)^{n_p}}. \quad (\text{D5})$$

This form is operationally more useful, as it contains only N_P^{-1} . Hinshaw et al. (2006) describes the method to evaluate the temperature part of the likelihood.

The effect of *P06* mask is included in N_P^{-1} . Suppose that the structure of N_P^{-1} is given by

$$N_P^{-1} = \begin{pmatrix} A & B \\ B & D \end{pmatrix}, \quad (\text{D6})$$

where A is the noise matrix for unmasked pixels, D is for masked pixels, and B is for their correlations. We assign infinite noise to the masked pixels such that $N_P \rightarrow N_P + \lambda(I - M)$, where M is the diagonal matrix whose elements are zero for masked pixels and unity otherwise. In the limit of $\lambda \rightarrow \infty$, the inverse of N_P is given by

$$N_P^{-1} \rightarrow \begin{pmatrix} A - B'DB & 0 \\ 0 & 0 \end{pmatrix}. \quad (\text{D7})$$

We have checked that this form of N_P^{-1} yields the unbiased estimates of the signal matrix from simulated realizations of the WMAP data. When the masked pixels were simply ignored (i.e., $B'DB = 0$), on the other hand, the estimated signal matrix was found to be biased high. As the likelihood form is sensitive to the precise form of N_P^{-1} , it is important to treat the mask in this way so that the estimated signal matrix from the data is unbiased.

We mask the polarization maps as follows. We first mask the maps at the full resolution, $n_{\text{side}} = 512$, and then degrade the masked maps using the weight that is diagonal in pixel space, $N_{P,pp}^{-1}$, to a lower resolution, $n_{\text{side}} = 16$. (Note that while the weight is diagonal in pixel space, it contains noise covariance between \tilde{Q}_p and \tilde{U}_p . The spurious polarization term, S , is ignored in this process.) The degraded mask is redefined such that it takes on 1 when the lower resolution pixel contains more than half of the original full resolution pixels, and 0 otherwise. We degrade these maps further to the resolution of $n_{\text{side}} = 8$ using the full noise matrix, and also degrade the mask and the noise matrix. (The noise matrix has been masked using Eq [D7].) We use the resulting maps and noise matrix in the likelihood function given in equation (D5).

E. AN ESTIMATE OF Ω_{GW}

Tensor perturbations generated by inflation are stochastic in nature, so the gravity wave perturbation can be expanded in plane waves

$$h_{ij}(\eta, \mathbf{x}) = \int \frac{d^3k}{(2\pi)^3} \left[h_+(\eta, \mathbf{k}) \epsilon_{ij}^+ e^{-i\mathbf{k}\cdot\mathbf{x}} + h_\times(\eta, \mathbf{k}) \epsilon_{ij}^\times e^{-i\mathbf{k}\cdot\mathbf{x}} \right], \quad (\text{E1})$$

where ϵ_{ij}^a is the polarization tensor, and $a = +, \times$ are the two polarizations in the transverse traceless (tt) gauge (in which $h_{ij,j} = h_i^i = 0$; we also set $h_{00} = h_{0j} = 0$). The stress-energy tensor for gravity waves is defined as

$$T_{\mu\nu} = \frac{1}{32\pi G} \langle h_{\alpha\beta,\mu} h^{\alpha\beta}_{,\nu} \rangle, \quad (\text{E2})$$

and in the tt gauge, we have

$$T_{00} = \frac{1}{32\pi G} \langle \dot{h}_{ij} \dot{h}^{ij} \rangle. \quad (\text{E3})$$

Thus,

$$\begin{aligned} \langle \dot{h}_{ij} \dot{h}^{ij} \rangle &= \int \frac{d^3k}{(2\pi)^3} \int \frac{d^3k'}{(2\pi)^3} e^{i(\mathbf{k}-\mathbf{k}')\cdot\mathbf{x}} \\ &\quad \left[\langle \dot{h}_+(\eta, \mathbf{k}) \dot{h}_+(\eta, \mathbf{k}') \rangle \epsilon_{ij}^+ \epsilon^{+ij} + \langle \dot{h}_\times(\eta, \mathbf{k}) \dot{h}_\times(\eta, \mathbf{k}') \rangle \epsilon_{ij}^\times \epsilon^{\times ij} \right] \end{aligned} \quad (\text{E4})$$

The variance of the perturbations in the h fields can be written as

$$\langle \dot{h}_a(\eta, \mathbf{k}) \dot{h}_a(\eta, \mathbf{k}') \rangle = \langle |\dot{h}_a(\eta, \mathbf{k})|^2 \rangle (2\pi)^3 \delta^3(\mathbf{k} - \mathbf{k}'), \quad (\text{E5})$$

and since $\epsilon_{ij}^a \epsilon^{aij} = 2$, we obtain

$$\langle \dot{h}_{ij} \dot{h}^{ij} \rangle = \int \frac{d^3k}{(2\pi)^3} 2 \left[\langle |\dot{h}_+(\eta, \mathbf{k})|^2 \rangle + \langle |\dot{h}_\times(\eta, \mathbf{k})|^2 \rangle \right]. \quad (\text{E6})$$

Writing

$$h_a(\eta, \mathbf{k}) = h_a(0, \mathbf{k}) T(\eta, k), \quad (\text{E7})$$

where T is the transfer function, we have

$$\begin{aligned} \langle \dot{h}_{ij} \dot{h}^{ij} \rangle &= \int \frac{4\pi k^2 dk}{(2\pi)^3} 2 \left[\langle |h_+(0, \mathbf{k})|^2 \rangle + \langle |h_\times(0, \mathbf{k})|^2 \rangle \right] \dot{T}^2(\eta, k) \\ &= \int \frac{dk}{k} \frac{2k^3}{2\pi^2} \left[\langle |h_+(0, \mathbf{k})|^2 \rangle + \langle |h_\times(0, \mathbf{k})|^2 \rangle \right] \dot{T}^2(\eta, k). \end{aligned} \quad (\text{E8})$$

From the definition of the primordial tensor power spectrum,

$$\Delta_h^2(k) = \frac{2k^3}{2\pi^2} \left[\langle |h_+(0, \mathbf{k})|^2 \rangle + \langle |h_\times(0, \mathbf{k})|^2 \rangle \right], \quad (\text{E9})$$

we obtain

$$\langle \dot{h}_{ij} \dot{h}^{ij} \rangle = \int d \ln k \Delta_h^2(k) \dot{T}^2(\eta, k). \quad (\text{E10})$$

Now

$$T_{00} = \rho_{GW} \equiv \int d \ln k \frac{d\rho_{GW}}{d \ln k}, \quad (\text{E11})$$

thus we have

$$\frac{d\rho_{GW}}{d \ln k} = \frac{\Delta_h^2(k) \dot{T}^2(\eta, k)}{32\pi G}. \quad (\text{E12})$$

Remembering that $\Omega = \rho \times (8\pi G/3H_0^2)$, we obtain

$$\frac{d\Omega_{GW}}{d \ln k} = \frac{\Delta_h^2(k) \dot{T}^2(\eta, k)}{12H_0^2}. \quad (\text{E13})$$

Therefore,

$$\Omega_{GW} = \int d \ln k \frac{\Delta_h^2(k) \dot{T}^2(\eta, k)}{12H_0^2}. \quad (\text{E14})$$

The transfer function T and its time derivative \dot{T} can be calculated easily by numerically integrating the evolution equation for the polarization states, which, neglecting the neutrino anisotropic stress, is given by

$$h_a'' + 2 \left(\frac{a'}{a} \right) h_a' + k^2 h_a = 0, \quad (\text{E15})$$

where prime denotes derivatives with respect to conformal time η , related to the time derivative by $d\eta = dt/a(\eta)$. This expression may be numerically integrated. In the following, however, we derive an analytic estimate relating a given limit on the tensor-to-scalar ratio, r , and the measured amplitude of the primordial scalar power spectrum, A , to a limit on the current energy density in primordial gravitational radiation.

There are several approaches taken in the literature to derive analytic expressions for the tensor transfer function, though these results are obtained in almost all cases for a universe containing only matter and radiation. These include using (1) an instantaneous transition from radiation to matter domination (Abbott & Harari 1986; Ng & Speliotopoulos 1995; Grishchuk 2001; Pritchard & Kamionkowski 2005, e.g.), (2) a “transfer function” to account for the smooth transition from radiation domination to matter domination (Turner et al. 1993; Wang 1996; Turner 1997, e.g.,), and (3) WKB methods (Ng & Speliotopoulos 1995; Pritchard & Kamionkowski 2005, e.g.,). In the following derivation, we will apply the sudden transition approximation to a Λ CDM universe (Zhang et al. 2005, see also), which is a good approximation for gravitational waves with wavelengths much longer than the time taken for the transition to happen.

In a universe which undergoes a set of piecewise instantaneous transitions in the scale-factor, given by $a(\eta) \propto \eta^{-\nu}$, the solution to eq. E15 is given by

$$h(\eta, k) = (k\eta)^{\nu+1} [C j_\nu(k\eta) + D y_\nu(k\eta)], \quad (\text{E16})$$

where j_ν and y_ν are spherical Bessel functions of order ν of the first and second kinds, respectively. Here, $\nu = -1$ for radiation-domination (RD, $\eta < \eta_{eq1}$), $\nu = -2$ for matter-domination (MD, $\eta_{eq1} < \eta < \eta_{eq2}$), and $\nu = +1$ for Λ -domination (LD, $\eta > \eta_{eq2}$). η_{eq1} is the conformal time at radiation-matter equality, with a scale-factor corresponding to $a_{eq1} = (\Omega_r/\Omega_m)$, and η_{eq2} is the conformal time at matter- Λ equality, with a scale-factor corresponding to $a_{eq2} = (\Omega_m/\Omega_\Lambda)^{1/3}$. For a concordance cosmology with $\{\Omega_r, \Omega_m, \Omega_\Lambda, h\} = \{4.18 \times 10^{-5}/h^2, 0.3, 0.7, 0.72\}$, $\eta_{eq1} = 103 \text{ Mpc}^{-1}$ and $\eta_{eq2} = 12270 \text{ Mpc}^{-1}$ (115 and 12030 Mpc^{-1} respectively in the instantaneous approximation).

To obtain the coefficients C and D , we require h and h' to be continuous at each of the transitions, η_{eq1} and η_{eq2} . Thus, denoting $x \equiv k\eta_0$ and making use of special properties of spherical Bessel functions, we obtain the transfer function and its derivative at present:

$$T(x) = x^2 [C j_1(x) + D y_1(x)], \quad (\text{E17})$$

$$\dot{T}(k, x) = kx^2 [C j_0(x) + D y_0(x)]. \quad (\text{E18})$$

The coefficients are given by

$$C = \frac{1}{2x_2^6} [2Ax_2^3 + 3B(1+x_2^2) + 3\cos(2x_2)(B+2Ax_2-Bx_2^2) + 3\sin(2x_2)(2Bx_2+A(x_2^2-1))] \quad (\text{E19})$$

$$D = \frac{1}{2x_2^6} [2Bx_2^3 - 3A(1+x_2^2) + 3\cos(2x_2)(A-2Bx_2-Ax_2^2) + 3\sin(2x_2)(B+2Ax_2-Bx_2^2)] \quad (\text{E20})$$

$$A = \frac{3x_1 - x_1 \cos(2x_1) + 2\sin(2x_1)}{2x_1} \quad (\text{E21})$$

$$B = \frac{2 - 2x_1^2 - 2\cos(2x_1) - x_1 \sin(2x_1)}{2x_1}, \quad (\text{E22})$$

where $x_1 \equiv k\eta_{eq1}$ and $x_2 \equiv k\eta_{eq2}$.

Further, we have the following definitions:

$$\Delta_h^2(k) = \Delta_h^2(k_0) \left(\frac{k}{k_0} \right)^{n_t(k_0)} \quad (\text{E23})$$

$$r \equiv \frac{\Delta_h^2(k_0)}{\Delta_{\mathcal{R}}^2(k_0)}, \quad (\text{E24})$$

where

$$\Delta_{\mathcal{R}}^2(k_0) \simeq 2.95 \times 10^{-9} A(k_0). \quad (\text{E25})$$

To eliminate n_t , we use the inflationary single-field consistency relation, $n_t = -r/8$.

Combining these equations, and evaluating them at the present conformal time η_0 (with $a = 1$) for modes within our current horizon, we are left with

$$\Omega_{GW} = \frac{1}{12H_0^2} \int_{2\pi/\eta_0}^{\infty} \frac{dk}{k} r \Delta_{\mathcal{R}}^2(k_0) \left(\frac{k}{k_0} \right)^{-r/8} k^2 (k\eta_0)^4 [C(k, \eta_{eq1}, \eta_{eq2}) j_0(k\eta_0) + D(k, \eta_{eq1}, \eta_{eq2}) y_0(k\eta_0)]^2, \quad (\text{E26})$$

where k and η_0 are to be evaluated in units of $1/\text{Mpc}$ and $k_0 = 0.002 \text{ Mpc}^{-1}$. We can now change to the dimensionless variable $x \equiv k\eta_0$ and obtain

$$\Omega_{GW} \simeq \frac{2.95 \times 10^{-9} r A(k_0) x_0^{r/8}}{12H_0^2 \eta_0^2} \int_{2\pi}^{\infty} dx x^{5-r/8} [C j_0(x) + D y_0(x)]^2, \quad (\text{E27})$$

where $x_0 = k_0 \eta_0$. We also have the result

$$\frac{d\Omega_{GW}}{d \ln k}(k, \eta_0) = 2.21 \times 10^{-3} (rA) \left(\frac{k}{k_0} \right)^{-r/8} [\dot{T}(k, \eta_0)]^2 \quad (\text{E28})$$

$$\simeq 2.21 \times 10^{-3} (rA) \left(\frac{k}{k_0} \right)^{-r/8} \{k\chi^2 [C j_0(x) + D y_0(x)]\}^2. \quad (\text{E29})$$

Now

$$H_0 \eta_0 = \int_0^1 \frac{1}{\sqrt{\Omega_r + \Omega_m a + \Omega_\Lambda a^4}}, \quad (\text{E30})$$

and $H_0 \eta_0 = 3.25$ for the concordance Λ CDM model. Taking the concordance model and $k_0 = 0.002 \text{ Mpc}^{-1}$, for given upper limits on r and A , the upper limit on Ω_{GW} is given by (Peiris 2003),

$$\Omega_{GW} \leq 2.33 \times 10^{-11} (rA) (27.05)^{r/8} [0.1278 - 0.0835 (\log r) - 0.0671 (\log r)^2 - 0.0248 (\log r)^3], \quad (\text{E31})$$

where the logarithm is taken in base ten.